University of Strathclyde

Department of Naval Architecture, Ocean and Marine Engineering

Peridynamic Modelling of Fatigue Damage in Polycrystalline Materials

By

Ning Zhu

A thesis submitted in fulfilment of the requirements for the degree of Doctor of Philosophy

Glasgow, U.K.

September, 2021

AUTHOR STATEMENT

This thesis is the result of the author's original research. It has been composed by the author and has not been previously submitted for examination which has led to the award of a degree.

Signed: Date:

ACKNOWLEDGEMENTS

I would like to thank:

Dr. Erkan Oterkus who guided me how to carry out research, supported me throughout my PhD with kindness, passion and dedication, encouraged me with my communication skills through the writing of journal papers and presentation skills through the delivery of several presentations in the research group (PMMA).

Dr. Emrah Celik who offered me the opportunity to become a visiting scholar to the University of Miami, gave me the great interest in 3D Printing, and experienced the research life in America.

The financial support of the Department of Naval Architecture, Ocean and Marine Engineering for the study and research visit to America.

All my friends and the staffs in the NAOME department who gave me the unforgettable memories through my study.

Finally, I would like to thank my family for all the support and encouragement. And my wife Xiaorui Ju, I felt so lucky meeting her, and her love and support helped me to overcome the challenges.

ABSTRACT

Fracture of structures and materials can bring great threat to human life, environment and finance. Among all types of fracture mechanisms, one of the most important ones to be considered is fatigue fracture. Although many studies have carried out on macroscopic point of view, only few studies are focus on crystal level. The main objective of this study is to find an alternative way to simulate microscopic fatigue cracks.

Engineers have developed various of techniques (continuum mechanics) and numerical methods (Finite Element Method) to study fracture of structures. However, majority of these numerical techniques are based on partial differential equations and will become invalid when there are discontinuities (cracks and sharp concentration gradients) occurring inside the body. To overcome this limitation, a continuum mechanics theory based on integro-differential equations, Peridynamics (PD), was developed and used for both fracture and fatigue analysis.

Since the study is focus on crystal level, an ordinary state-based polycrystal PD formulation is developed to analyse cubic polycrystalline materials to overcome the constraint condition on material constants brought by Bond-based (BB) PD theory. The formulation is validated by first considering static analyses and comparing the displacement fields obtained from the finite element method and Ordinary State-based (OSB) PD. As a result, the OSB PD polycrystal model can provide accurate displacement fields by comparing it with finite element method. Then, dynamic analysis is performed to investigate the effect of grain boundary strength, crystal size, and discretization size on fracture behaviour and fracture morphology.

In the past decades, several different methods (Stress – Life, Strain – Life and Paris Law etc.) have been developed to assist researchers on studying fatigue crack propagations, which also have been combined with PD theory by researchers. For instance, studies on stress energy release rate of a crack tip (for instance J-integral) have been carried out, but few methods are available to calculate the Stress Intensity Factor (SIF) which is directly related to a widely used formula to evaluate crack propagation rate in fatigue analysis – Paris' Law. However, using J-integral can sometime be quite tricky, due to which path has been chosen for analyse. In this study, Displacement Extrapolation Method (DEM) is used to calculate SIF in PD framework more conveniently. In DEM, only crack surface needs to be checked each time when crack propagates, so the detection of the position of crack tip becomes rather important. Although several methods combined with Cohesive Zone Model (CZM) have been used to find crack tip in fracture analysis, few studies on crack tip tracking technique have been done in PD framework. In this thesis, a new automatic crack tip tracking method is discovered and accurately validated by comparing the crack growth speed with the existing study.

In the end, all the above methods, including the implemented polycrystal OSB PD formulation, new approach of calculating SIF using DEM under PD framework and the all-new crack tip tracking method, are combined with the PD fatigue model to provide an alternative way to simulate fatigue crack propagation of polycrystalline material.

TABLE OF CONTENTS

LIST OF FIGURES

LIST OF TABLES

ABBREVIATIONS

ADR	Adaptive Dynamic Relaxation
ATSB	Australian Transport Safety Bureau
BB	Bond-based
BCM	Boundary Collocation Method
BEM	Boundary Element Method
CCM	Classical Continuum Mechanics
CEM	Cohesive Element Method
COD	Crack Opening Displacements
CZE	Cohesive Zone Element
CZM	Cohesive Zone Model/Method
DEM	Displacement Extrapolation Method
FDM	Finite Difference Method
FEM	Finite Element Method
GB	Grain Boundary
GI	Grain Interior
MD	Molecular Dynamic
NOSB	Non-Ordinary State-based
NTSB	American National Transportation Safety Board
OSB	Ordinary State-based

PD	Peridynamic
SIF	Stress Intensity Factor
WW2	World War II
XFEM	Extendend Finite Element Method

NOMENCLATURE

$\mathbf{x}$	Vector defining the position of a material point in the undeformed configuration
$\mathbf{x}'$	Vector defining the position of a neighbour of material point $\mathbf{x}$ in the undeformed configuration
$\ddot{\mathbf{u}}(\mathbf{x},t)$	Acceleration associated with material point $\mathbf{x}$
$\rho(\mathbf{x})$	Density associated with material point $\mathbf{x}$
∇	Divergence operator
$\mathbf{b}(\mathbf{x},t)$	Body force applying on material point $\mathbf{x}$
$\mathbf{u}(\mathbf{x},t)$	Displacement of material point $\mathbf{x}$
$\mathbf{x}'-\mathbf{x}$	Vector defining the relative position of material points $\mathbf{x}$ and $\mathbf{x}'$ in the undeformed configuration
σ	Stress tensor
t	Time
$\mathbf{f}$	PD force function
$dV_{\mathbf{x}'}$	Infinitesimal volume associated with material point $\mathbf{x}'$
$H_{\mathbf{x}}$	Horizon
δ	Radius of the horizon

$\mathbf{y}$	Vector defining the position of a material point in the deformed configuration
$\mathbf{y}'$	Vector defining the position of a neighbour of material point $\mathbf{y}$ in the deformed configuration
$\mathbf{y}'-\mathbf{y}$	Vector defining the relative position of material points $\mathbf{y}$ and $\mathbf{y}'$ in the deformed configuration
c	Bond constant (BB PD)
s	Bond stretch
s_0	Critical bond stretch
$\mathbf{t}$	Force density vectors of the material point $\mathbf{x}$ (OSB PD)
$\mathbf{u}'-\mathbf{u}$	Difference of displacements vectors of the material points $\mathbf{x}$ and $\mathbf{x}'$
A and B	Material constants (OSB PD)
Δ	Grid size
$\mathbf{x}_i$	Vector defining the position of the particle i
V_j	Volume of the particle j
υ_j	Volume correction factor of the particle j
w	Micro potential of a bond
ξ	Length of a bond

W_i	Strain energy density of the particle i
S_i	Surface correction factor
n_t	Current time step
$n_t + 1$	Next time step
$\mathbf{D}$	Fictitious diagonal density matrix
c_d	Damping coefficient
K_{ij}	Stiffness matrix of the whole system
Δt	Time step size
$\mathbf{e}$	Unit vector
φ	Crystal orientation
ϕ	Angle between type 1 bond and the crystal orientation
θ	PD dilatation
a	OSB PD material constant
b_{T1}	OSB PD material constant for Type 1 bonds
b_{T2}	OSB PD material constant for Type 2 bonds
d	OSB PD material constant
Q_{ij}	Reduced material constants of a cubic crystal
μ	Shear modulus
κ	Bulk modulus

G_c	Critical energy release rate
K_{Ic}	Fracture toughness
E	Young's modulus
β	Interface strength coefficient
h	Thickness of the body
υ	Poisson's ratio
K_I	Stress intensity factor under Mode I loading condition
K_{II}	Stress intensity factor under Mode II loading condition
K_{III}	Stress intensity factor under Mode III loading condition
λ	Bond remaining life
A and m	Material constants in PD fatigue analysis
R	Load ratio
$D_{\min}$ and $D_{\max}$	Critical damage factors

1. INTRODUCTION

There are four sections in this chapter. In the first section, general information of incidents happened in past years which caused due to fatigue was introduced, to show the importance of fatigue analysis in human life, and the impact to human safety if fatigue fracture was not treat properly. In the second section, the aims of this research will be highlighted. The objectives of this research will be introduced in the third section, and at last the reviews of past papers on how researchers solved the same objectives will be discussed.

1.1. Background

The high-speed development of modern technology not only brings convenience to human life, but also brings threat if certain procedures could not be followed strictly. Although large amount of energy and money have been spent on research of both fracture mechanics and fatigue to prevent the incidents, it can still bring significant loss to human life when it happens, not only in marine industries, but also other fields, such as civil engineering and aerospace industries. One of the most famous accidents which took away 101 lives and injured 88 people was the Eschede Derailment, Germany on 3rd June 1998. According to (Oestern *et al.*, 2000), one of the most important reasons was the fatigue fracture damage occurred at the thin steel tyre of one of the dual block wheels at the first coach of the train, and the steel tyre was peeled away from the wheel and pricked through the floor and then remain embedded. The train was originally equipped with single-cast wheelsets, however, the design resulted in great vibration and noise especially at restaurant car. To reduce the vibration, the company, ICE, changed the wheels to “wheel-tyre” type wheels, which added a thick rubber damper between the wheel body and the thin steel tyre

(see Figure 1). Although this type of wheels only used on low-speed trams at that moment and never tested on high-speed trains, the change not only solved the vibration problem, but also brought great threat on wheels, as the tyres were flattened into an ellipse shape when the wheel turned through each cycle, which brought fatigue damage to the steel tyre after certain cycles. The failure of steel tyre triggered the followed several events resulting in one of the most serious train incidents in recent years.

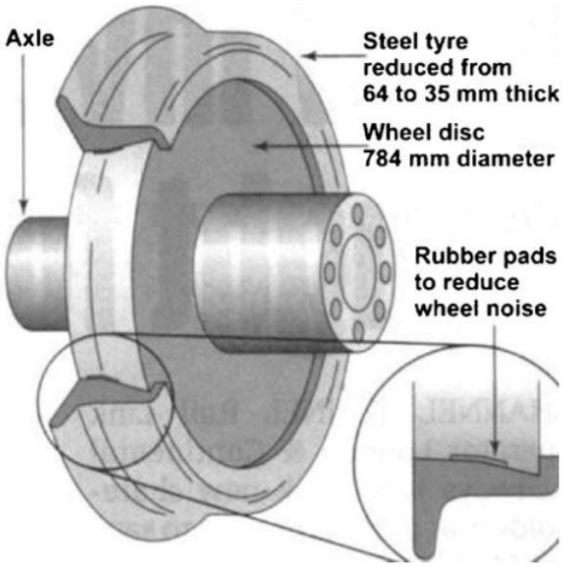

Figure 1. Configuration of the wheel-tyre type wheel which failed at Eschede 23 June 1998 (Smith, 2013)

The incidents can not only happen on land transports, but on aerospace field as well. In modern human life, airplane has become the most common transportation type for a long-distance travel. As the airplane itself has become larger and more advanced, safety has become more important as well, otherwise the accident can likely bring more serious loss than the trains. On 4th November 2010, the engine of a high-tech Airbus A380 aircraft, the largest passenger aircraft ever in human history, from Qantas Airline failed after departing from Changi Airport, Singapore (ATSB, 2013). The engine failure brought huge impact to the structure and system of the plane, and

luckily the plane safely returned to and landed at Changi Airport after management by the flight crew. After investigation of the damaged engine, Australian Transport Safety Bureau (ATSB) found out that several oil feed stub pipes did not fulfil the design specifications, resulting in significantly thin wall of the pipes (Figure 2), which reduced the fatigue life of the pipe and fatigue crack occurred. The oil leak from the crack finally caused fire inside the engine and blew up the engine structure. Although the incident itself was mainly caused by the manufacture failure, otherwise the fatigue damage would not happen on the pipe, it still can be seen how important the role that fatigue plays in human life.

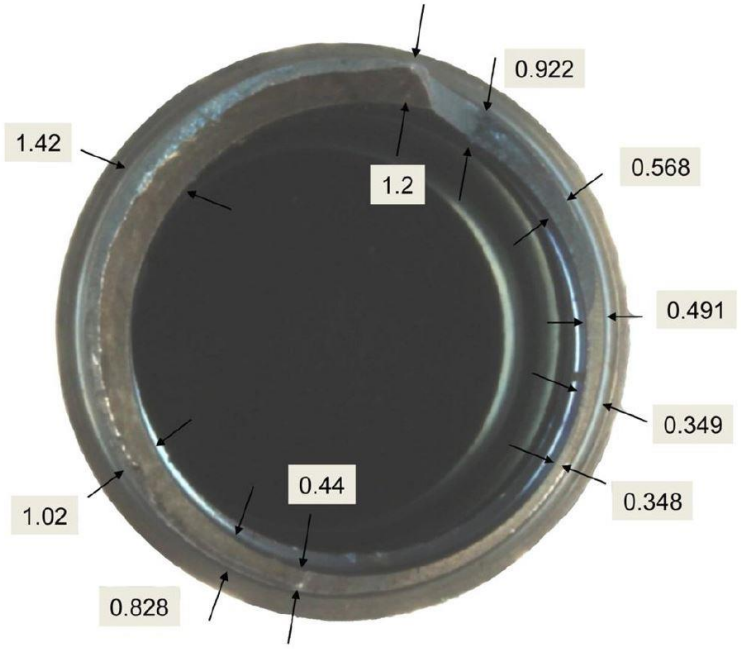

Figure 2. Wall measurements (units: mm) of the fractured oil feed pipe (ATSB, 2013)

Not only the oil pipes, but also the engine blades could also result in fatigue damage and bring huge threat to passengers. On 27th August 2016, a fan blade of the engine of a Boeing 737 which operated by Southwest Airlines was separated from the fan disk and caused serious uncontained engine failure. After the investigation operated by American National Transportation Safety Board (NTSB), it was clearly found that

the separation of the blade was caused due to metal fatigue damage (NTSB, 2016). Similarly, about one and a half years later, the incident happened again on 17th April 2018. Although the incident is still under investigation, NTSB announced that fatigue crack was the reason caused by the break of the blade (NTSB, 2018). Unlike the previous incident that all passengers and crew members were survived, this time one woman was dead, and eight people were injured.

Fatigue damage could also bring harm in civil engineering, for example the Mianus River Bridge at Greenwich, Connecticut, USA collapsed due to both metal corrosion and fatigue damage on the pin which connected to the bridge structure (NTSB, 1984), and the Sgt. Aubrey Cosens VC Memorial Bridge collapsed due to fatigue fracture of steel hanger rods, according to Canadian Ministry of Transportation (Ben-Daya, Kumar and Murthy, 2016).

Similar to the incidents happened in civil engineering, trains, and planes, fatigue also plays relatively important role in marine industries. Researchers did not spend much attention on fracture mechanics before World War II (WW2), as cracks thought to be too small to threaten large structures such as ships. However, during the war, many ships failed and broke into half all in a sudden and in inexplicable ways. One of the most popular incidents was the liberty ships. Many liberty ships were built during WW2 by US ship industries to transport supplies to Europe. Although most of the sinking ships were because of the attack from the German torpedoes, still 1200 Liberty-class ships (about 30% of all Liberty-class ships) were suffered with cracks and 3 of which were broken into half (Wei Zhang, 2016). The cause of the fracture was not fully understood at first of the ship Schenectady, one of the three broken ships, but later research discovered the fracture was due to the cold weather which

change the material of the ship to become highly brittle and fatigue crack initiated easily, and then finally caused the failure (Thompson, 2001). The other very famous incident was the capsize of the Norwegian semi-submersible drilling platform called Alexander L. Kielland in March 1980. A year later, an investigation report concluded that the platform collapsed because of a fatigue crack in one of the six bracings, which connected the leg to the platform. The fatigue crack propagated and broke the bracing, and then triggered the broken of the rest five bracings and disconnected the leg to the platform (Norway, 1981). The incident took 123 lives and only 89 people survived, making this the worst disaster in Norwegian offshore history after WW2.

Not only the ships, but offshore platforms are also suffering from fatigue damage. On 4 December 2015, a 31-year-old platform called Gunashli Platform No. 10, which located in the west of oil field Gunashli in the Caspian Sea near Azerbaijan, caught fire which caused by the breakage of a high-pressure subsea pipeline (Bagirova, 2015). The pipeline was damaged in a severe storm, and the wave impact force was so strong that an explosion of the gas escaped and finally a fire broke out. Moreover, another offshore platform in the same area was collapsed due to the same storm on the same day (Azvision, 2015). Both events caused fatalities (one for each case) and numbers of lives (30 and 3 respectively) were still missing. Although these platforms were damaged due to the heavy storm, the harsh environmental condition can cause significant loss of fatigue life of the platform so that the aging condition of the platforms in Gunashli field posed a serious risk to safety (Executive, 2016).

1.2. Aim of Research

As the incidents have brought great threat to human life, researchers have developed different methods, from S-N curve to Finite Element Method (FEM), to prevent these

incidents from happening. The aim of this research study is to use PD theory to enhance the safety of ship and offshore structures.

1.3. Objectives of Research

In order to achieve the aim, the following objectives need to be fulfilled:

- Creation of a Peridynamic model using Ordinary State-based (OSB) PD theory to investigate the microstructural fracture behaviour of cubic crystals.
- Calculation of the Stress Intensity Factor (SIF) using Displacement Extrapolation Method (DEM) under PD framework.
- Creation of a suitable technique to find the estimate location of the crack tip, i.e. Crack tip Tracking Technique.
- Creation of a new PD fatigue polycrystal model to simulate simple crystal structure under cyclic loading condition.

To verify the method, for example the OSB PD cubic crystal model, introduced in this thesis, a more common and widely used FEM has been used as a benchmark study. The displacement field (Chapter 3.4.2) and SIF (Chapter 4.4) can be calculated using the FEM software ANSYS. The Crack tip Tracking Technique was verified by simulating the same problem listed in (Madenci and Oterkus, 2014) and comparing the crack growth distance – time curves of the two studies.

As (De Meo, Zhu and Oterkus, 2016) has already used Bond-based (BB) Peridynamic theory to model the fracture behaviour of cubic crystals. According to author's knowledge, there were no research studies available in the literature about fracture and crack growth in polycrystalline materials before (De Meo, Zhu and Oterkus, 2016). The cubic crystals were chosen for the start of the study due to its

relatively simple 6×6 material matrix (only 3 material constants) compare with the normal crystal who has 36 different material constants in theory. The studies on more complex polycrystalline material can be considered in the future. To overcome the PD constant constraint brought by the limitation of BB PD theory, the OSB PD was chosen in the study.

Since SIF plays a very important role in fatigue simulations, i.e. Paris' Law, it is important to find a proper method to evaluate either Critical Strain Energy Release Rate or the SIF to calculate crack propagation rate. J-integral has been used by (Guanfeng Zhang *et al.*, 2016) to strain energy release rate at crack tip region, and (Y. L. Hu and Madenci, 2017) explored a method to calculate strain energy release rate for each material points. However, few have used DEM to calculate SIF which has been widely used in FEM.

In order to calculate the suitable number of cycles to jump during fatigue analysis using Paris' Law equation, location of crack tip need to be monitored. Unlike the use of FEM and CZM in fatigue analysis, crack tip tracking technique has been well developed. However, few research studies have been made in this area, the thesis will provide an idea on how to automatically update crack tip location in PD theory.

Several different PD fatigue models have been developed recently. For example, (Guanfeng Zhang *et al.*, 2016) used a method introduced earlier by (Stewart A. Silling and Askari, 2014), and (Y. L. Hu and Madenci, 2017) developed a new method by calculating strain energy release rate for each material points. This thesis extended the PD fatigue formulation given by (Stewart A. Silling and Askari, 2014) and coupled a crack tip tracking algorithm to study the fracture behaviour of 2D polycrystalline materials.

1.4. Literature Review

1.4.1. Review of Numerical Methods to Predict Structural Damage

To fulfil the aim of this research, the first objective is to find a proper numerical method (tool) to carry out the simulation of structural damage. Nowadays in engineering industries, there are several popular numerical approaches under the framework of Classical Continuum Mechanics (CCM) used to predict structural damage, such as the Boundary Element Method (BEM), the FEM, the CZM implemented in FEM by using finite cohesive elements and the eXtended Finite Element Method (XFEM).

The early study of BEM in the field was reported by (Rizzo, 1967) and (Cruse, 1969) to solve electrostatic problems. As discussed in (Sadd, 2009), the BEM has two major advantages over the FEM. The first advantage is that the equation system of boundary elements is much smaller than that of finite elements, resulting in lower computational cost. The second advantage is that several studies showed that the BEM is more accurate in determination of stress concentration effects. In FEM, when dealing with problems of infinite extent, there are difficulties in developing appropriate meshes which would significantly affect the accuracy of the results, however, BEM only requires boundary meshing which means it could handle infinite extent problems automatically, and additional computation is required for the solution at internal points. Later after the discovery of BEM, several modifications had been developed to overcome the problem when using BEM formulation to model discontinuities such as fractures and crack growth. (Aliabadi and Rooke, 1991) briefly described and discussed the advantages and limitations of these modifications. Among which the main limitation of BEM is that the matrices are

unsymmetric and fully populated (common on crystal level analysis) that means it will be relatively computational expensive to solve the matrix.

FEM was also one of the most widely used numerical tools in solving engineering problems including solution of discontinuous fields. The discovery of FEM could be tracked back to early 1940s by the work of (Hrennikoff, 1941) and (Courant, 1994). But the real impetus of the FEM was in the 1960s by the developments of several researchers such as (Hinton and Irons, 1968). However, with the development of FEM, similar problems as BEM was discovered that FEM was not able to produce reasonable accurate results around the crack tip area (Aliabadi and Rooke, 1991). In order to overcome this problem, (Tracey, 1971) introduced the determination of crack tip element. Moreover, additional difficulties and limitations were found when solving the crack propagation problems. For the modelling of propagating cracks, remeshing of the model is necessary and easy after the incremental crack growth for elastic materials (Madenci and Oterkus, 2014), however, according to (Anderson, 2005), due to the plastic strain field need to be passed to the remeshed model for elastic-plastic materials, the remeshing will bring problems.

In the 1960s, to overcome the limitations when using FEM to solve dynamic crack propagation problems without requirements of remeshing, CZM was introduced by (Barenblatt, 1962) and (Dugdale, 1960) to indicate the nonlinear processes at the front of a crack. But the actual breakthrough of the method was the developing of Cohesive Zone Elements (CZE) by (Hillerborg, Modéer and Petersson, 1976) for Mode-I cracks and (Xu and Needleman, 1994) for mixed mode cracks. The implementation not only overcame the limitations, but also brought new problems, like softening of material properties when decreasing mesh size (Madenci and

Oterkus, 2014). Due to the concept of CZM, the propagation of cracks is limited to fixed boundaries of elements, which can restrict the crack path (for example crack branching) being represented even the mesh is fine (Papoulia, Vavasis and Ganguly, 2006).

Since the introduction of XFEM by (Belytschko and Black, 1999) and (Moës, Dolbow and Belytschko, 1999) in 1999 to resolve the difficulties of modelling crack growth without remeshing, the method was widely used by researchers to solve crack propagation problems including mixed-mode cracks (Cox, 2009, Mariani and Perego, 2003), however, there are still limitations when solving multiple crack growth and complex problems (Zi, Rabczuk and Wall, 2007) and predictions of SIF (Rabczuk, Bordas and Zi, 2010).

In summary, as described above, researchers were trying to overcome the limitations on modelling discontinuities using various numerical method. However, there are still other problems need to be solved. For example, limitations on solving fully populated matrix in BEM, remeshing problem on simulating cracks using FEM, restrictions of crack path in CEM, and multi-crack growth problem when using XFEM. Since these are quite common problems that need to face when studying fractures on crystal level, none of them was suitable for the research study in this thesis.

The numerical methods described in this section are all based on CCM, which are formulated using derivatives of the displacement components, therefore the mathematical formulation becomes invalid when discontinuities occur inside the body (Madenci and Oterkus, 2014). To overcome the problem of discontinuities, (Stewart A Silling, 2000) introduced a nonlocal theory called PD theory by changing

the partial derivatives in the governing equations to spatial integrals. Unlike CCM, material failure is part of the PD constitutive laws and there are no additional criteria needed to predict direction, speed and branching etc of cracks. With these advantages, PD can overcome the limitations mentioned in previous paragraphs, which is a suitable method to simulate cracks. More detailed information of PD theory will be introduced in the Chapter 2.

1.4.2. Literature Studies on Polycrystalline Materials

Polycrystalline materials are widely used in many different industrial applications. Amongst the various existing polycrystalline materials, metals and ceramics are common examples. Polycrystalline materials are composed of individual crystals that have a particular crystal orientation and are separated from neighbouring crystals via grain boundaries. Microscopic features of polycrystalline materials such as crystal orientation, grain boundary strength, etc. may have a significant effect on the overall macroscopic behaviour of the material, especially on the fracturing behaviour of these materials. Therefore, it is essential to analyse this type of material at the microscopic scale, which is the reason why the main objective of this research study is to simulate fatigue crack growth of polycrystal material.

At first, experimental methods were used to study polycrystalline materials. X-ray was used by (Gay, Hirsch and Kelly, 1954) to study the deformation of polycrystalline metals by rolling, whereas the combination of X-ray diffraction and X-ray imaging were used to study 3D characterization of polycrystalline materials at the microscale (Ludwig *et al.*, 2009). (Herbig *et al.*, 2011) also used X-ray diffraction and tomography to analyse and visualise the growth rate and grain orientation of the fracture surface of the metastable beta titanium alloy Ti 21S.

Unlike the above researchers who used X-ray as the main experimental procedure, (Groeber *et al.*, 2006) applied a dual-beam focused ion beam-scanning electron microscope (FIB-SEM) system to study the 3D reconstruction and characterisation of Ni-based superalloy.

Although experimental approaches can be useful to analyse polycrystalline materials, it is not always possible to perform such experiments and they can also be very expensive. For example, the fatigue analyses of marine structures are normally considered as high-cycle fatigue, so it would be un-necessary to study fatigue fracture behaviour of crystals using experimental approaches. Hence, numerical approaches can be very good alternative. There are various numerical studies available as described in previous session, which can also be used for polycrystalline material problems. For example, CZM was used by (Barut, Guven and Madenci, 2006) for micromechanical analysis of crystal plasticity, (Zhou *et al.*, 2012) for crack propagation analysis of ceramic tool materials and (Lin, Wang and Zeng, 2017) for intergranular and trans-granular fracture of polycrystalline solids. Moreover, BEM (Benedetti and Aliabadi, 2013, Sfantos and Aliabadi, 2007a), XFEM (N Sukumar *et al.*, 2003, N Sukumar and Srolovitz, 2004) and FEM (CR Chen and Li, 1998, Crocker, Flewitt and Smith, 2005, Warner and Molinari, 2006) were also used for polycrystalline materials analysis. In addition, for some complex problems, such as multi-scale modelling (Sfantos and Aliabadi, 2007b), a combination of different methods were usually used for the analysis, for example, CZM and BEM (Benedetti and Aliabadi, 2013), BEM and FEM (Sfantos and Aliabadi, 2007b) and CZM and FEM (Kraft *et al.*, 2008). In addition, numerical results were usually compared with experimental results to examine for the accuracy (Bronkhorst, Kalidindi and Anand, 1992).

As discussed above, although some researchers have used numerical tools (CZM) to solve failure in polycrystalline materials (Benedetti and Aliabadi, 2013, Zhou *et al.*, 2012), the same limitations have been brought to the analysis of fracture of polycrystalline materials, i.e. the crack path has been restricted to specific CZEs. This is the reason why the fracture behaviours been studied in these papers were focused on trans-granular fractures. However, the inter-granular fractures also need to be considered, these numerical and experimental approaches are not suitable to achieve the main objective of this thesis.

1.4.3. Literature Studies on Stress Intensity Factors

As described in the previous two sections, PD theory has the advantage on simulating discontinuities problems of polycrystalline materials compare with other numerical methods, and SIF is widely used on fatigue analysis, therefore it is necessary to find a method to calculate SIF under PD framework.

SIF was first introduced by (Irwin, 1957) to describe the stress distribution around the crack tip region, and widely used to predict fatigue crack growth (Schijve, 2009). With the development of the calculation of SIF in the following years, several theoretical formulations had been developed to help researchers to determine the stress field around crack tips including central crack in an infinite plate under uniform uniaxial stress (Rooke and Cartwright, 1976), edge crack in a plate under uniaxial stress (Mingchao Liu *et al.*, 2015) and slanted crack in a biaxial stress field (George C. Sih, Paris and Erdogan, 1962) etc. On one hand, theoretical formulations provide researchers different ways to calculate SIF for non-complex problems; on the other hand, they are not quite suitable for complex problems, like inter-granular fracture in polycrystals.

The numerical methods, such as FEM and BEM, provided researchers more choice to calculate the SIF. Analytical solutions were used in some studies for validation of numerical results. For example, both (Kishimoto, Aoki and Sakata, 1980) and (Xiao and Chen, 2001) used FEM to simulate stress intensity factor and compare the results with simple analytical solutions. Moreover, BEM was used by (Blandford, Ingraffea and Liggett, 1981) to compute two-dimensional SIF and compared with the results calculated from displacement correlation method given by (Shih, de Lorenzi and German, 1976), (Barsoum, 1976) and (Ingraffea, 1978). The analytical solutions of SIF can be calculated based on various of formulations, such as formulations based on stress applied on the crack surface which can be calculated from the force applied on the model (Petroski and Achenbach, 1978), and crack opening displacements (COD) were computed by (Guinea *et al.*, 1998) using the expression given by (P. C. Paris, 1957). (Lim, Johnston and Choi, 1992) summarised and compared different displacement-based stress intensity factor formulations. However, many researchers usually use numerical methods to simulate either displacement field or stress field around the crack tip area, and then use corresponding displacement-based or stress-based formulation to compute the stress intensity factor. For instance, (Lazzarin and Tovo, 1998) used FEM to solve the stress field and then applied it to the formulation given by (Gross and Mendelson, 1972). FEM had also been used by (Rybicki and Kanninen, 1977) to calculate the displacement field in order to compute the SIF. Similarly, BEM was used by (Dominguez and Gallego, 1992) and (Martínez and Domínguez, 1984) to simulate the stress and displacement field respectively, and then apply the results to the corresponding formulation to compute SIF. Unlike the most widely used FEM and BEM, both Boundary Collocation Method (BCM) (Zheming Zhu *et al.*, 2006), Finite Difference Method (FDM) (Y. M. Chen, 1975)

and XFEM (Nagashima, Omoto and Tani, 2003) can also be used to calculate the SIF. Due to the relationship between the strain energy release rate and stress intensity factor, both (Parks, 1974) and (Miyazaki *et al.*, 1993) used J-integral to compute the strain energy release rate around crack tip and then converted it to SIF. As an alternative approach, a new continuum mechanics formulation, peridynamics, can be used to determine SIF. (Imachi, Tanaka and Bui, 2018) determined mixed-mode dynamic SIFs by using OSB PD based on the J-Integral value of the crack tip. (Wenke Hu *et al.*, 2012) and (Panchadhara and Gordon, 2016) presented a procedure to calculate J-Integral in bond-based peridynamic framework. (Stenström and Eriksson, 2019) proposed a new procedure on J-Integral calculation in PD framework by writing J-Integral as a function of displacement derivatives.

In this thesis, a new approach is presented to determine SIF by using DEM in PD framework. PD theory is first used to obtain the displacement field around the crack surface. Then, by using the evaluated displacement field, DEM is utilized to compute the SIF. Unlike the commonly used J-Integral to calculate SIF in PD framework, DEM can directly link the displacement field solved by PD theory with SIF using a much simpler formulation, which means the simulation time can be saved significantly when carrying out fatigue analysis. As discussed in previous sections, it is essential for this study to choose PD theory to simulate fatigue crack growth in polycrystalline materials due to the advantages that PD can carry out complex crack propagation problem easier than other numerical methods. Moreover, unlike FEM who need to couple with CZE to simulate cracks, there's no alternative approach needed for PD. Therefore, the use of DEM under PD framework is necessary.

DEM was introduced by (Paul C. Paris and Sih, 1965) and also used by (Nagashima, Omoto and Tani, 2003) to calculate SIF. Details of PD theory can be found in various studies available in the literature (De Meo, Zhu and Oterkus, 2016, Madenci and Oterkus, 2014, Oterkus, Madenci and Oterkus, 2017, Oterkus, Guven and Madenci, 2012). The information about PD theory will be given in the following chapter. To demonstrate the capability of the coupled DEM and PD approach to calculate SIFs, three benchmark cases are considered and PD results are compared with analytical and FEM results.

1.4.4. Literature Studies on Fatigue Analysis Techniques

Fatigue is one of the main reasons which cause failures in engineering structures, and predictions of these failures due to cyclic loadings are usually challenging. Engineers and researchers have developed several different methods to overcome the challenges. During the late 20th century, experimental methods were mainly used by researchers to analyse the fatigue crack propagation. (Reece, Guiu and Sammur, 1989) studied and compared crack propagations of two alumina under two different loading conditions (static and cyclic), and electron micrograph was used to scan the fracture surface of static and cyclic cracks and compared differences between them. Moreover, optical micrographs were used by (Dauskarat, Marshall and Ritchie, 1990), (Von Euw, Hertzberg and Roberts, 1972) and (Dauskardt, Yu and Ritchie, 1987) to monitor the cyclic fatigue crack paths in experiments. However, researchers usually used several different methods to analyse the experimental results. Paris' law, which was first introduced by (Paul C. Paris, 1961) to establish the fatigue crack propagation rate based on the stress intensity factor introduced in Irwin's theory (Irwin, 1957), was applied by many researchers (Dauskarat, Marshall and Ritchie, 1990, Von Euw, Hertzberg and Roberts, 1972, Dauskardt, Yu and Ritchie, 1987,

Hopper and Miller, 1977, Zheng and Hirt, 1983, Pearson, 1975) to modify the results generated from the experiments. Another method which is also widely used in both industries and research is the stress-life (S-N) method. For example, the S-N curve obtained from the bending fatigue test of a high carbon-chromium specimen was used to understand the fracture modes (Shiozawa, Lu and Ishihara, 2001), and (Marines *et al.*, 2003) also used the S-N curve to modify the ultrasonic fatigue test results of the bearing steel AISI-SAE 52100. Unlike (Donahue *et al.*, 1972) who used COD method to calculate SIF in order to estimate the fatigue crack growth rate, crack closure was used by (Wolf, 1970, Lindley and Richards, 1974, J. C. Newman, 1981) to analyse the fatigue crack growth and (Rice, 1967) summarised the mechanics of near crack deformation and fatigue crack propagation.

The development of technology and computational methods also provides researchers more options when dealing with fatigue analysis problems. One of the most common methods, FEM, has been used by (Dhondt, 1998) to solve the stress field around the crack tip region, and then use the S-N curve to predict the fatigue life of the structure. Also, (Dong, 2001) used both FEM and S-N curve to study the fatigue behaviour of weld joints. Similarly, Paris' Law has been used by (James C Newman, 1976) after solving the stress data around cracking area using FEM. However, not only the FEM, but also the BEM has been used by (Gerstle, Martha and Ingraffea, 1987) to compute the SIF, which then been used to calculate the fatigue crack growth rate using Paris' Law. Since there are limitations for the FEM when dealing with the crack growth problem, Cohesive Element Method (CEM)/ CZM has been developed by researchers to overcome this limitation. For example, after generating displacement field using CEM, both Paris' Law and COD method were considered by (Nguyen *et al.*, 2001) to compare the propagation rate of both

long and short cracks. Both (Roe and Siegmund, 2003) and (Yang, Mall and Ravi-Chandar, 2001) used CZM to predict fatigue crack growth, however, the former used strain energy release rate to compute the crack growth rate, and the latter used Paris' Law. X-FEM, which is also being widely used in fracture mechanics, has been used by (N. Sukumar, Chopp and Moran, 2003) to study the three-dimensional fatigue crack propagation. Not only the stress related methods can be used for fatigue analysis, strain energy related methods can also solve fatigue problems. (G. C. Sih and Barthelemy, 1980) provided expressions on calculation of crack growth rate based on strain energy density, and claimed that using strain energy density to predict mixed mode fatigue crack growth rate is more convenient than SIFs. Additionally, a strain energy density model was generated by (Huffman *et al.*, 2017) to predict fatigue crack propagation of a pressure vessel mild steel. Moreover, since J-integral method can be used to compute the strain energy release rate around crack tip region, (Dowling and Begley, 1976) used J-integral to study the elastic-plastic fatigue cracking behaviour. Although the methods described above are mainly focusing on macroscopic level, they could also be used for fatigue analysis at crystal level. For instance, microscopy and X-ray can be used to visualise and monitor the fatigue crack pattern at crystal level (Zhai, Wilkinson and Martin, 2000, Chevalier, Olagnon and Fantozzi, 1999, L. Liu *et al.*, 2011). Moreover, not only CZM (Bouvard *et al.*, 2009) and FEM (Kirane and Ghosh, 2008, L. Liu *et al.*, 2011, Proudhon *et al.*, 2016), but also the Molecular Dynamics (MD) (Potirniche *et al.*, 2005, Tang, Kim and Horstemeyer, 2010) can be used to study fatigue crack growth rate for crystals.

In this thesis, an alternative numerical approach called PD theory is used to study the fatigue crack propagation in polycrystalline structures. PD theory was first introduced in (Stewart A Silling, 2000, Stewart A Silling and Askari, 2005) and

being used by researchers to solve various types of problems. The PD fatigue model was first introduced by (Oterkus, Guven and Madenci, 2010), however, (Stewart A. Silling and Askari, 2014) provided another model which can reproduce the well-known Paris' Law, and been used by (Guanfeng Zhang *et al.*, 2016) to predict and compare the crack pattern with experimental results. A different PD fatigue model was introduced by (Y. L. Hu and Madenci, 2017), which is based on the calculation of critical strain energy release rate, to predict the fatigue life of composite lamina. This thesis will implement the PD fatigue model given in (Guanfeng Zhang *et al.*, 2016) with a crack tip detecting algorithm, and carried out the analysis in a finite element analysis software (for instance, ANSYS) by following expressions given by (Macek and Silling, 2007).

2. PERIDYNAMIC THEORY

2.1. Introduction

The main purpose of this chapter is to introduce PD theory in details and to give readers a more in-depth understanding of the advantages of this theory and the reason why it was selected to carry out fatigue analysis. There are three different types of PD theory which are used by the researchers around the globe. These are BB PD (Stewart A Silling, 2000), OSB PD (Stewart A Silling *et al.*, 2007) and Non-Ordinary State-based (NOSB) PD (Warren *et al.*, 2009). One of the main differences between BB PD and OSB PD is that the Poisson's ratio of the materials is limited to 1/4 for 3D analysis (1/3 for 2D) in BB PD theory, however, OSB PD theory overcomes this limitation by adding dilatation term in the formulation. In NOSB PD, since both the stress and strain tensors are used in the formulation, interaction forces can be in any directions. In this thesis, OSB PD is used in the simulations of polycrystalline materials to overcome the limitation brought by the BB theory (De Meo, Zhu and Oterkus, 2016). BB PD is then used to solve the displacement field, and then coupled with DEM to calculate the SIF of a crack. At last, the polycrystal fatigue analysis is carried out using BB PD theory.

2.2. Review of Peridynamic Theory

The new numerical method PD was first introduced by (Stewart A Silling, 2000) which reformulated the governing equation of CCM. CCM was first formulated by the French mathematician Augustin-Louis Cauchy in the 19th century (Reddy, 2013), and assumes that the solid body is continuum, which means that the body can be divided into smaller volumes (so called material points). The results (for example displacement, temperature and force etc.) can be obtained by solving differential

equations under different fundamental laws, such as conservation of mass, energy and momentum. FEM, one of the most widely used methods in engineering world, is a well-known example of CCM, and has been used in famous commercial software (ANSYS, ABAQUS) for structural analysis. Although numerical methods based on CCM are widely used, there are several limitations as well. Firstly, CCM is a local theory, which means each material point can only interact with its neighbouring points. However, when the analysis is at microscopic scale, the material points can not only interact with their neighbours, but also other material points within a specific region. The interactions between these non-neighbouring points are called long-range forces, and need to be considered in microscopic analysis. Therefore, CCM is not sufficient enough for analysing at such small scales. Secondly, the governing equation of CCM is based on partial differential equations, which means the equation cannot be used to analyse the body with discontinuities, i.e. cracks, due to the breakdown of mathematical formulation (Stewart Andrew Silling and Bobaru, 2005). Some external approaches based on fracture mechanics can be applied to overcome some part of this limitation, but these approaches may not be suitable for micro-scale analysis (Stewart Andrew Silling and Bobaru, 2005). Although MD can overcome this limitation for the analysis of micro structures, it also requires more computation power in order to achieve the acceptable accuracy. Thanks to the development of PD theory, the analysis of micro structures and material failures can be completed at the same time.

2.3. Bond-based Peridynamic Theory

The equation of motion of a material point $\mathbf{x}$ in CCM can be written as follows:

$$\rho(\mathbf{x})\ddot{\mathbf{u}}(\mathbf{x},t) = \nabla \cdot \sigma + \mathbf{b}(\mathbf{x},t) \tag{1}$$

where $\rho(\mathbf{x})$ denotes the density of material point $\mathbf{x}$ and $\ddot{\mathbf{u}}(\mathbf{x},t)$ denotes the acceleration of the material point $\mathbf{x}$ at time t. ∇ represents the gradient operator, σ is the stress tensor, and $\mathbf{b}(\mathbf{x},t)$ represents the body force applying on material point $\mathbf{x}$ at time t, respectively. As mentioned in the previous section, due to the term ∇ in the equation, it is not suitable to obtain solutions problems with discontinuities, i.e. cracks.

PD theory overcomes this limitation by replacing the derivative term with integral term, and the equation of motion of a material point $\mathbf{x}$ in PD can be written as follows (Stewart A Silling, 2000):

$$\rho(\mathbf{x})\ddot{\mathbf{u}}(\mathbf{x},t)=\int_{H_{\mathbf{x}}}\mathbf{f}\left(\mathbf{u}(\mathbf{x}',t)-\mathbf{u}(\mathbf{x},t),\mathbf{x}'-\mathbf{x}\right)dV_{\mathbf{x}'}+\mathbf{b}(\mathbf{x},t) \tag{2}$$

where $\mathbf{u}(\mathbf{x},t)$ denotes the displacement of material point $\mathbf{x}$ at time t, and $\mathbf{x}'-\mathbf{x}$ represents the relative distance between material points $\mathbf{x}$ and $\mathbf{x}'$. $\mathbf{f}\left(\mathbf{u}(\mathbf{x}',t)-\mathbf{u}(\mathbf{x},t),\mathbf{x}'-\mathbf{x}\right)$ is the PD bond force between material points $\mathbf{x}$ and $\mathbf{x}'$, $V_{\mathbf{x}'}$ represents the volume of material point $\mathbf{x}'$. As shown in Figure 3, in PD theory, the material point $\mathbf{x}$ not only can interact with neighbouring points but also can interact with other material points that are far apart.

In PD theory, it is assumed that the bond force between two material points decreases with increasing of the distance between these two points, and when the distance is larger than a specific value, there will be no interactions at all. This region is called horizon, which can be shown as $H_{\mathbf{x}}$ in Figure 4. The radius of horizon is often written as δ in PD formulations.

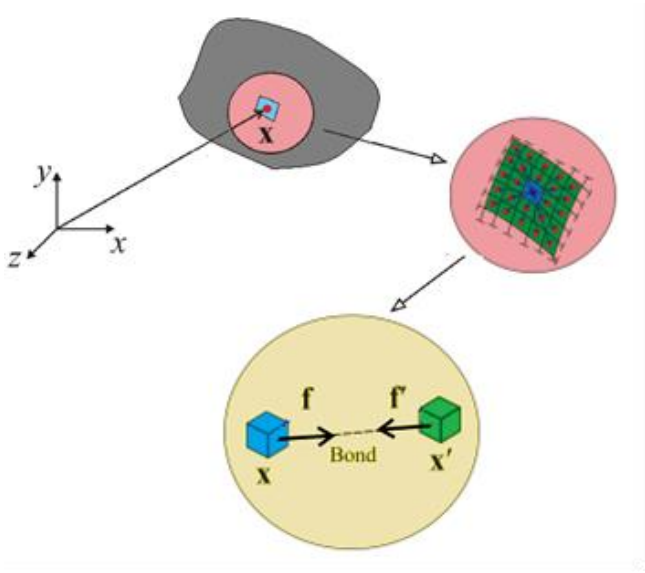

Figure 3. Peridynamic Interactions

The horizon size δ is defined manually. The larger the horizon size, the more accurate of the result, however, it requires more time for the analysis to complete. When δ decreases and tends to zero, interactions become more and more local. So CCM can be treated as a special case of PD theory.

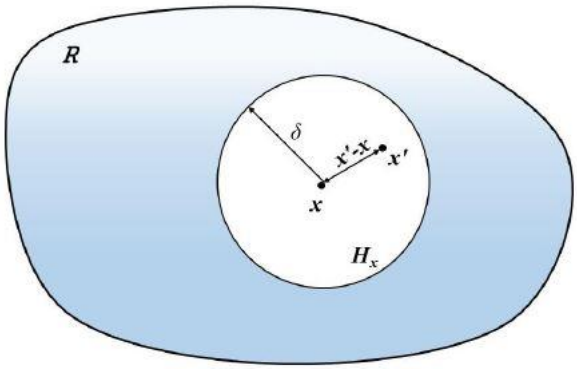

Figure 4. Peridynamic Horizon

The pairwise bond force function $\mathbf{f}$ in Equation (2) can be expressed in deformed configuration (Figure 5) whose expression can be given below:

$$\mathbf{f} = cs\frac{\mathbf{y}'-\mathbf{y}}{|\mathbf{y}'-\mathbf{y}|} \tag{3}$$

where c denotes the bond constant which can be expressed in terms of material properties in CCM, based on the description given by (Madenci and Oterkus, 2014). $\mathbf{y}$ represents the position of the material point $\mathbf{x}$ after deformation, in other words, $\mathbf{y}=\mathbf{x}+\mathbf{u}$. s is the PD bond stretch which can be defined as:

$$s=\frac{|\mathbf{y}'-\mathbf{y}|-|\mathbf{x}'-\mathbf{x}|}{|\mathbf{x}'-\mathbf{x}|} \tag{4}$$

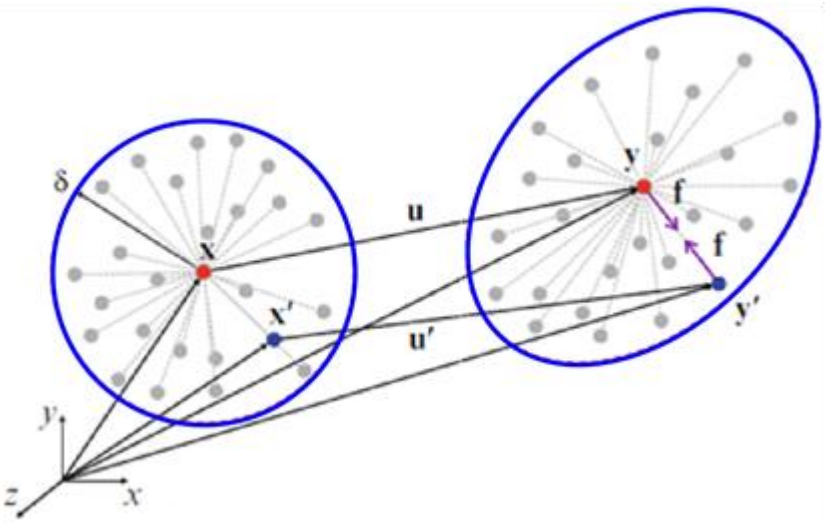

Figure 5. Peridynamic Deformed Configurations (Bond-based)

The relationship between PD bond constant c and PD bond stretch s for brittle materials can be shown in Figure 6. As shown in Figure 6, when bond stretch s exceeds a certain value s_0, PD bond breaks, which means there will be no longer interactions between material points associated with this bond (as shown in Equation (5)).

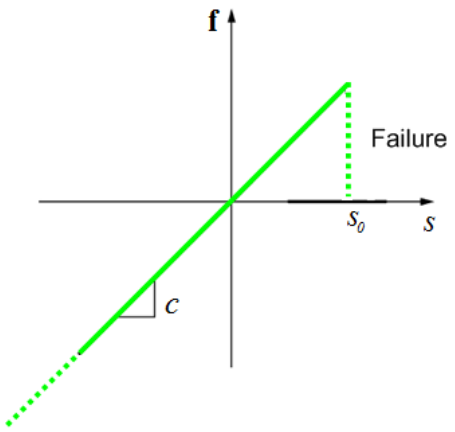

Figure 6. PD Bond Behaviour (Brittle Materials)

The s_0 in Equation (5) is called the critical stretch. In PD theory, the local damage of a material point is defined as the ratio between the number of broken bonds and the number of total bonds. Therefore, a material point with damage value of 0 means that there are no broken bonds connected to this material point. And damage value of 1 means that all bonds connected to this material point are broken. As shown in Figure 7, half of the bonds within the horizon of a material point are broken, so the damage of this material point is 0.5 (Madenci and Oterkus, 2014).

$$\mu\left(\mathbf{x}'-\mathbf{x},t\right)=\begin{cases}1 & \text{when } s<s_0\\ 0 & \text{when } s>s_0\end{cases} \tag{5}$$

2.4. Ordinary State-based Peridynamic Theory

Unlike the equation of motion of BB PD theory shown in Equation (2), the equation of motion of OSB PD can be written as:

$$\rho\left(\mathbf{x}\right)\ddot{\mathbf{u}}\left(\mathbf{x},t\right)=\int_{H_{\mathbf{x}}}\left(\mathbf{t}\left(\mathbf{u}'-\mathbf{u},\mathbf{x}'-\mathbf{x},t\right)-\mathbf{t}'\left(\mathbf{u}'-\mathbf{u},\mathbf{x}'-\mathbf{x},t\right)\right)dH_{\mathbf{x}}+\mathbf{b}\left(\mathbf{x},t\right) \tag{6}$$

where $\mathbf{t}\left(\mathbf{u}'-\mathbf{u},\mathbf{x}'-\mathbf{x},t\right)$ and $\mathbf{t}'\left(\mathbf{u}'-\mathbf{u},\mathbf{x}'-\mathbf{x},t\right)$ denote the force density vectors of the material points $\mathbf{x}$ and $\mathbf{x}'$, and $\mathbf{u}'-\mathbf{u}$ represents the difference of displacements of

the material points $\mathbf{x}$ and $\mathbf{x}'$ at time t. Similar to Equation (2), $H_{\mathbf{x}}$ represents the PD horizon that defines the range of interaction of a particular material point, and the size of the horizon is usually represented by the symbol δ.

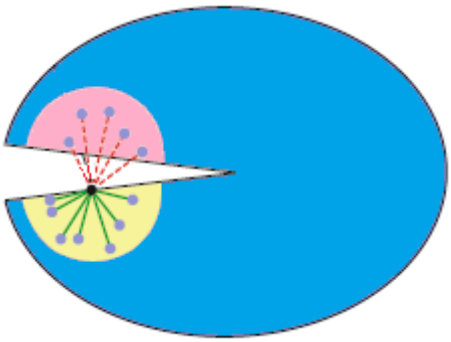

Figure 7. Damage in Peridynamic Theory

As shown in Figure 8, the magnitudes of the force density vector $\mathbf{t}$ and $\mathbf{t}'$ between material points $\mathbf{x}$ and $\mathbf{x}'$ are unequal, which can be obtained as:

$$\mathbf{t}\left(\mathbf{u}'-\mathbf{u},\mathbf{x}'-\mathbf{x},t\right)=\frac{1}{2}A\frac{\mathbf{y}'-\mathbf{y}}{|\mathbf{y}'-\mathbf{y}|} \tag{7}$$

And

$$\mathbf{t}'\left(\mathbf{u}-\mathbf{u}',\mathbf{x}-\mathbf{x}',t\right)=-\frac{1}{2}B\frac{\mathbf{y}'-\mathbf{y}}{|\mathbf{y}'-\mathbf{y}|} \tag{8}$$

where A and B are parameters which are dependent on material constants, horizon and displacement field.

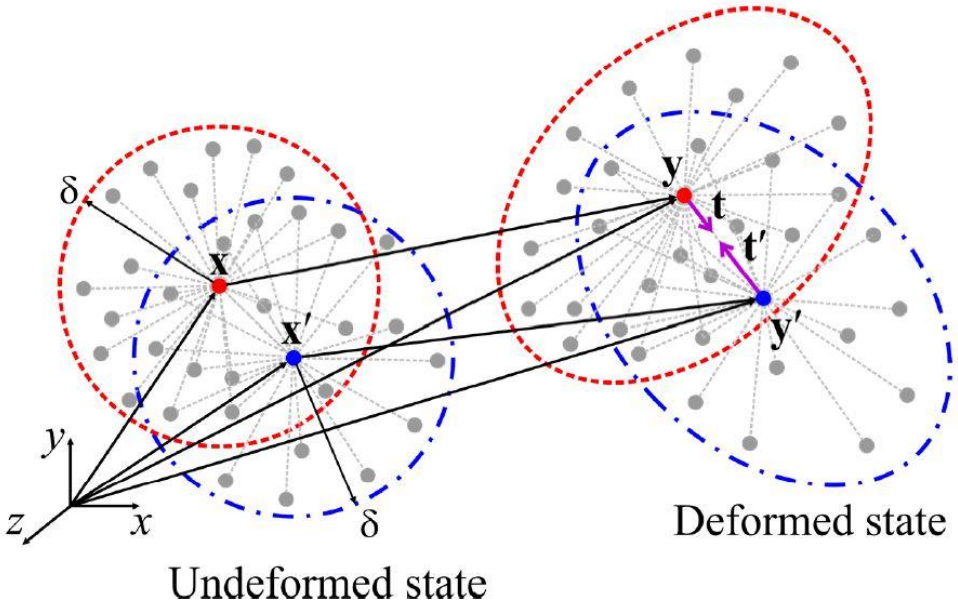

Figure 8. Peridynamic Forces between $\mathbf{x}$ *and* $\mathbf{x}'$ *in Ordinary State-based Peridynamic Theory*

2.5. Numerical Implementation of Peridynamics

In Peridynamic theory, the structure is discretized into finite number of volumes, and each volume represents a material point (as shown in Figure 9). When building up the PD model, only material points within the horizon can build up interactions with the reference material points, shown as yellow in Figure 9. The discretisation of the structure in PD theory are usually uniform, and the grid size is denoted as Δ. To simplify the analysis, the size of horizon is assumed to be symmetric and equals to $3^*\Delta$ until further notification. Therefore, the discretised form of equation of motion (EOM) for BB PD (Equation (2)) can be expressed as:

$$\rho(\mathbf{x}_i)\ddot{\mathbf{u}}(\mathbf{x}_i,t)=\sum_{j=1}^{n}\mathbf{f}\left(\mathbf{u}(\mathbf{x}_j,t)-\mathbf{u}(\mathbf{x}_i,t),\mathbf{x}_j-\mathbf{x}_i\right)V_j+\mathbf{b}(\mathbf{x}_i,t) \tag{9}$$

where n is the number of material points within the horizon of material point $\mathbf{x}_i$ (exclude the material point $\mathbf{x}_i$ itself).

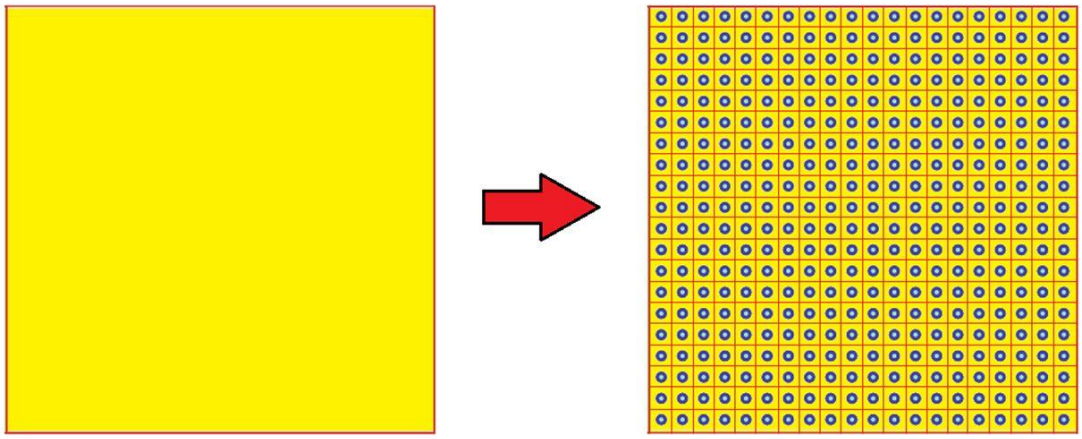

Figure 9. 2D Peridynamic Discretisation

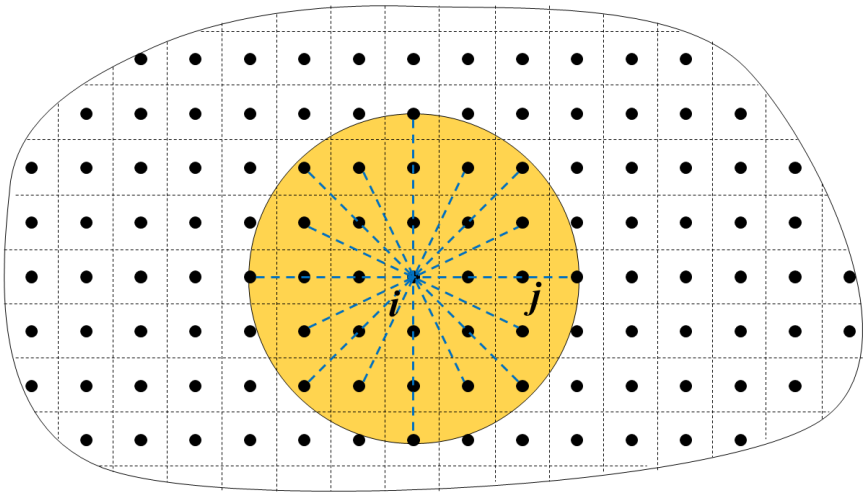

Figure 10. Peridynamic Domain

The discretised form of equation of motion for OSB PD (Equation (6)) can be expressed as:

$$\rho(\mathbf{x}_i)\ddot{\mathbf{u}}(\mathbf{x}_i,t)=\sum_{j=1}^{n}\begin{pmatrix}\mathbf{t}\left(\mathbf{u}(\mathbf{x}_j,t)-\mathbf{u}(\mathbf{x}_i,t),\mathbf{x}_j-\mathbf{x}_i\right)-\\ \mathbf{t}\left(\mathbf{u}(\mathbf{x}_i,t)-\mathbf{u}(\mathbf{x}_j,t),\mathbf{x}_i-\mathbf{x}_j\right)\end{pmatrix}V_j+\mathbf{b}(\mathbf{x}_i,t) \qquad (10)$$

2.5.1. Volume correction factor

As shown in Figure 11, since the structure is usually discretised uniformly in PD theory, the shape of each material point is square for 2D model. Due to the circular size of the horizon, for material points which are close to the edge of the horizon,

they are not fully embedded. Therefore, a correction factor needs to be applied to the volume term V_j in Equation (9) and (10). This correction factor is called Volume Correction Factor, and often written as υ_j in PD formulation. As explained in (Madenci and Oterkus, 2014) and shown in Figure 11, when the bond length $\xi_{ij} = \left|\mathbf{x}_j - \mathbf{x}_i\right| \le \delta - r$, where $r = \dfrac{\Delta}{2}$, the volume correction factor is $\upsilon_j = 1$. When the material points are located within the range $\delta - r < \xi_{ij} < \delta$, the volume correction factor is $\upsilon_j = \dfrac{\left(\delta + r - \xi_{ij}\right)}{2r}$.

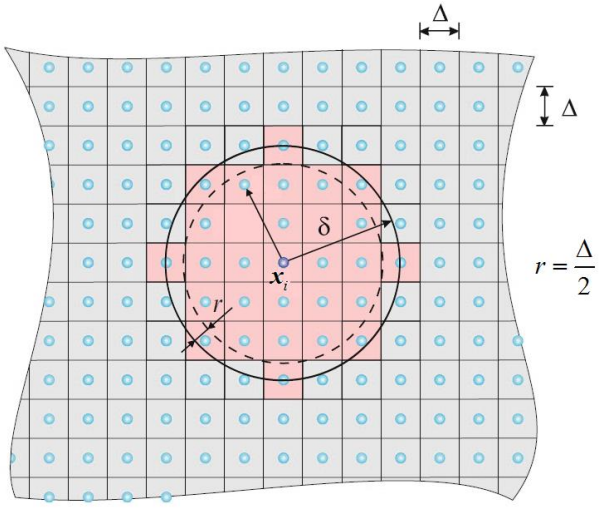

Figure 11. Volume Correction Factor

2.5.2. Surface correction factor

As shown in Figure 12, the circular sized horizon is not always fully embedded within the body. When a material point is located close to the free surface (Point 2 in Figure 12), the horizon of this material point is cut into a circular segment shape. To improve the accuracy, surface correction factor needs to be applied to the formulation. The surface correction factor of a material point can be calculated from the values of strain energy density by CCM and PD.

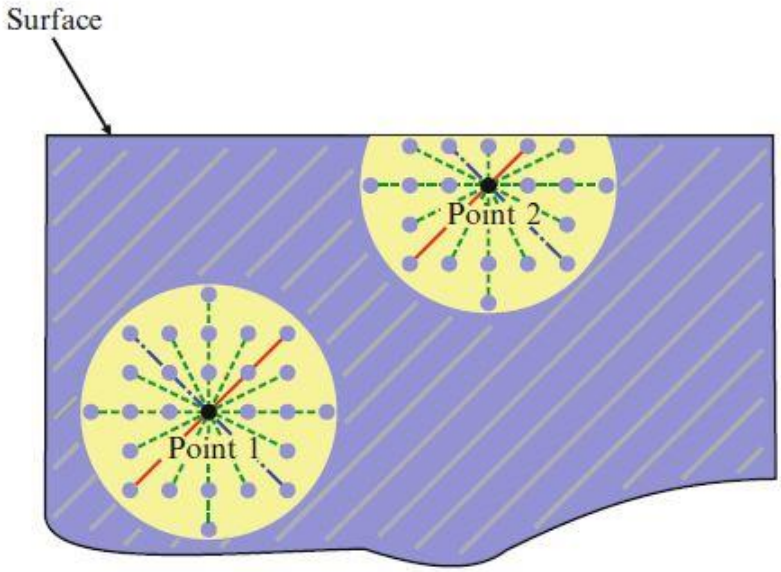

Figure 12. Surface Effect in Peridynamic Model

For example, in BB PD theory, the micro potential of a bond can be expressed as:

$$w = \frac{1}{2} c s^2 \xi \tag{11}$$

Since each material point of the bond shares the half of the micro potential w of this bond, the strain energy density of a material point can be calculated by integrating the micro potential within the entire horizon, hence:

$$W_i^{PD} = \frac{1}{2} \sum_{j=1}^{n} w_{ij} V_j \tag{12}$$

The strain energy density of CCM can be expressed based on the stress and strain state of a material point, so the expression can be written as:

$$W_i^{CCM} = \frac{1}{2} \sigma_i \varepsilon_i \tag{13}$$

Therefore, the surface correction factor of a material point can be defined as:

$$S_i = \frac{W_i^{CCM}}{W_i^{PD}} \tag{14}$$

Normally in PD theory, in order to approximate the surface correction in any direction, the correction factors of a material point in x-, y- and z-directions are calculated first, which can be written as:

$$\mathbf{g}_i = \left\{ S_i^x, S_i^y \right\}^T \tag{15}$$

Therefore, the surface correction factor for the bond between material point $\mathbf{x}_i$ and $\mathbf{x}_j$ can be obtained by the mean values as:

$$\bar{\mathbf{g}}_{ij} = \frac{\mathbf{g}_i + \mathbf{g}_j}{2} \tag{16}$$

As shown in Figure 13, an ellipsoid is then generated based on the correction factors calculated in Equation (15). Since the relative position vector of a bond can be expressed as: $\mathbf{n}_{ij} = \frac{\mathbf{x}_j - \mathbf{x}_i}{\left| \mathbf{x}_j - \mathbf{x}_i \right|}$, the surface correction of the bond ξ_{ij} can be determined as:

$$G_{ij} = \left(\left[\frac{n_{ij}^x}{\bar{g}_{ij}^x} \right]^2 + \left[\frac{n_{ij}^y}{\bar{g}_{ij}^y} \right]^2 \right)^{-\frac{1}{2}} \tag{17}$$

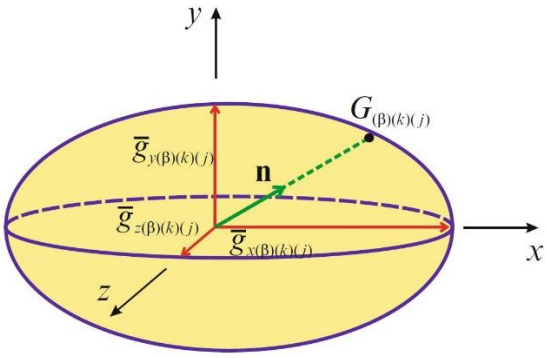

Figure 13. The Ellipsoid for the Surface Correction Factors

2.5.3. Time integration

Regarding the time integration in PD theory, the explicit forward and backward difference methods are applied. Initially, the displacement and velocity are defined by using explicit central difference scheme, which is described in (Stewart Andrew Silling and Bobaru, 2005), before the beginning of the integration. The acceleration of material point $\mathbf{x}_i$ of current time step n_t can be calculated from the equation of motion (both Equation (2) and Equation (6)). Therefore, the next time step's (n_t+1) velocity and displacement ($\dot{\mathbf{u}}_i^{n_t+1}$ and $\mathbf{u}_i^{n_t+1}$) can be calculated by using formulations given by (Madenci and Oterkus, 2014):

$$\dot{\mathbf{u}}_i^{n_t+1} = \dot{\mathbf{u}}_i^{n_t} + \ddot{\mathbf{u}}_i^{n_t} \cdot \Delta t \tag{18}$$

and

$$\mathbf{u}_i^{n_t+1} = \mathbf{u}_i^{n_t} + \dot{\mathbf{u}}_i^{n_t} \cdot \Delta t \tag{19}$$

In order to get proper stable numerical solution in explicit time integration, the time step size Δt needs to be relatively small. Hence, Δt can be determined based on a

von Neumann stability analysis as described in (Stewart Andrew Silling and Bobaru, 2005):

$$\Delta t < \sqrt{\frac{2\rho\Delta}{\pi\delta^2\Delta c}} \tag{20}$$

2.5.4. Adaptive dynamic relaxation

In PD, since the equation of motion is written in dynamic form, in order to solve the quasi-static problems, a dynamic relaxation technique can be applied. Based on the comments stated in (Kilic and Madenci, 2010), a static solution is actually a steady-state form of the fluctuating results, which can be obtained by introducing a damping factor to the dynamic system. Due to the fact that this damping factor is not always determined the most effectively, it needs to be determined every time step using Adaptive Dynamic Relaxation (ADR) scheme, which was firstly introduced in (Underwood, 1983).

Therefore, the EOM in PD can be rewritten in terms of ordinary differential equations after including the fictitious inertia and damping terms into the system:

$$\mathbf{D}\ddot{\mathbf{U}}\left(\mathbf{X},t\right)+c_d\mathbf{D}\dot{\mathbf{U}}\left(\mathbf{X},t\right)=\mathbf{F}\left(\mathbf{U},\mathbf{U}',\mathbf{X},\mathbf{X}'\right) \tag{21}$$

where $\mathbf{D}$ is the fictitious diagonal density matrix and c_d is the damping coefficient which can be determined by Greschgorin's theorem (Underwood, 1983) and Rayleigh's quotient, respectively. $\mathbf{U}$ and $\mathbf{X}$ are the displacement and position vectors that contain information for all material points in the system, which can be expressed as:

$$\mathbf{X}^T=\left\{\mathbf{x}_1,\mathbf{x}_2,\mathbf{x}_3,...,\mathbf{x}_m\right\} \tag{22}$$

and

$$\mathbf{U}^T = \left\{\mathbf{u}\left(\mathbf{x}_1, t\right), \mathbf{u}\left(\mathbf{x}_2, t\right), \mathbf{u}\left(\mathbf{x}_3, t\right), ..., \mathbf{u}\left(\mathbf{x}_m, t\right)\right\} \tag{23}$$

where m is the total number of material points in the system.

The force components of vector $\mathbf{F}$ in Equation (21) can be expressed as:

$$\mathbf{F}_i = \sum_{j=1}^{n}\left(\mathbf{t}_{ij} - \mathbf{t}_{ji}\right)\left(\upsilon_j V_j\right) + \mathbf{b}_i \tag{24}$$

To recall, υ_j represents the volume correction factor applied to the volume of material point j, and $\mathbf{t}_{ij}$ is the directional force density vector in OSB PD theory.

The components of the fictitious diagonal density matrix $\mathbf{D}$ in Equation (21) can be computed based on Greschgorin's theorem as:

$$\lambda_{ii} \geq \frac{1}{4}\Delta t^2 \sum_{j=1}^{n}\left|K_{ij}\right| \tag{25}$$

in which K_{ij} is the stiffness matrix of the system which can be determined by deriving from the PD interaction forces with respect to the relative displacement vector, and Δt is the time step size, which is usually assumed to be 1 in ADR. (Madenci and Oterkus, 2014) gives the expression of the elements of the stiffness matrix, K_{ij}, after using a small displacement assumption as:

$$\sum_{j}^{n}\left|K_{ij}\right| = \sum_{j=1}^{n}\frac{\partial\left(\mathbf{t}_{ij} - \mathbf{t}_{ji}\right)}{\partial\left(\left|\mathbf{u}_j - \mathbf{u}_i\right|\right)}\cdot\mathbf{e} = \sum_{j=1}^{n}\frac{\left|\xi_{ij}\cdot\mathbf{e}\right|}{\left|\xi_{ij}\right|}\frac{4\delta}{\left|\xi_{ij}\right|}\left(\frac{1}{2}\frac{ad^2\delta}{\left|\xi_{ij}\right|}\left(\upsilon_i V_i + \upsilon_j V_j\right) + b\right) \tag{26}$$

where $\mathbf{e}$ is the unit vector along x, y and z directions in Cartesian coordinate system, a, d and b are the PD constants in OSB PD theory, whose expressions will be explained in further sections in this thesis.

The damping factor c in Equation (21) can be expressed by introducing the lowest frequency of the system, while the lowest frequency can be determined from Rayleigh's quotient, as:

$$\omega = \sqrt{\frac{\mathbf{U}^T \mathbf{K} \mathbf{U}}{\mathbf{U}^T \mathbf{D} \mathbf{U}}} \tag{27}$$

Since the components in density matrix $\mathbf{D}$ may contain relatively large values, this can lead to significant difficulties to compute ω given in Equation (27). However, this problem can be solved by rewriting Equation (21) in the following form:

$$\ddot{\mathbf{U}}^n \left(\mathbf{X}, t^n \right) + c_d{}^n \dot{\mathbf{U}}^n \left(\mathbf{X}, t^n \right) = \mathbf{D}^{-1} \mathbf{F}^n \left(\mathbf{U}^n, \mathbf{U}'^u, \mathbf{X}, \mathbf{X}' \right) \tag{28}$$

The damping coefficient can therefore be expressed as:

$$c_d{}^n = 2 \sqrt{\frac{\left(\mathbf{U}^n \right)^T {}^1\mathbf{K}^n \mathbf{U}^n}{\left(\mathbf{U}^n \right)^T \mathbf{U}^n}} \tag{29}$$

where ${}^1\mathbf{K}^n$ is the diagonal "local" stiffness matrix that can be written as:

$${}^1K_{ii}^n = -\frac{F_i^n / \lambda_{ii} - F_i^{n-1} / \lambda_{ii}}{\Delta t \dot{u}_i^{n-1/2}} \tag{30}$$

Therefore, the velocities and displacements for the next time step can be calculated by applying central-difference explicit integration as:

$$\dot{\mathbf{U}}^{n+1/2} = \frac{\left(2 - c^n \Delta t\right)\dot{\mathbf{U}}^{n-1/2} + 2\Delta t \mathbf{D}^{-1}\mathbf{F}^n}{2 + c^n \Delta t} \tag{31}$$

and

$$\mathbf{U}^{n+1} = \mathbf{U}^n + \Delta t \dot{\mathbf{U}}^{n+1/2} \tag{32}$$

in which n is the n^{th} iteration. Since Equation (31) contains a special term which represents the velocity at $t^{n-1/2}$,for the initial condition when $n = 0$, $t^{-1/2}$ does not have any physical meaning. It is therefore assumed that the initial displacement and velocity field are $\mathbf{U}^0 \neq 0$ and $\dot{\mathbf{U}} = 0$, and the integration can then be started by:

$$\dot{\mathbf{U}}^{1/2} = \frac{\Delta t \mathbf{D}^{-1}\mathbf{F}^0}{2} \tag{33}$$

3. FRACTURE OF POLYCRYSTALLINE MATERIALS

3.1. Introduction

As opposed to partial differential equations that traditional approaches are based on, PD utilizes integro-differential equations without containing any spatial derivatives. Hence, these equations are always applicable regardless of discontinuities such as cracks. PD has been used for the fracture analysis of many different types of materials and material behaviours (Diyaroglu *et al.*, 2015, Madenci and Oterkus, 2016, Oterkus and Madenci, 2015, Panchadhara and Gordon, 2016). It has also been applied for the analysis of polycrystalline materials (Askari *et al.*, 2008, De Meo, Zhu and Oterkus, 2016). However, these studies used either original BB formulation (Stewart A Silling, 2000) or NOSB formulation (Stewart A Silling *et al.*, 2007). BB formulation has limitations on material constants whereas NOSB formulation may encounter the zero-energy mode problem. In order to overcome all these issues, an OSB PD formulation (Stewart A Silling *et al.*, 2007, Madenci and Oterkus, 2014) can be utilized. This is also the one of the reasons why OSB PD theory is used to simulate fracture of polycrystalline materials in this thesis.

The main purpose of this chapter is to introduce the implementation of OSB PD formulation to predict the fracture behaviour and mechanical response of cubic polycrystal material by introducing the interface strength coefficient. Firstly, the PD results of cubic polycrystalline material are obtained from ADR method for static analysis, and the results are compared with those obtained from FEM. Secondly, crack patterns are obtained from PD dynamic analysis, and the influence of grain boundary strength, crystal size and discretization size on fracture behaviour and fracture morphology is investigated. The study in this chapter can be found in (Ning

Zhu, De Meo and Oterkus, 2016), and the OSB PD formulation for polycrystalline material was utilized for the first time in the literature in order to overcome the limitations of BB formulation and zero-energy mode problem of NOSB theory.

3.2. Ordinary State-based Peridynamic Formulation for a Cubic Crystal

Similar to the BB PD model presented in (De Meo, Zhu and Oterkus, 2016), the OSB model for a cubic crystal can be represented using two types of interactions (bonds), as shown in Figure 14.

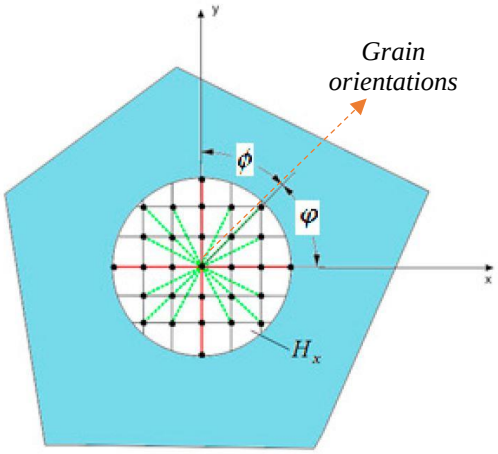

Figure 14. Type 1 bonds (green dashed lines) and Type 2 bonds (red solid lines) for the OSB PD cubic crystal model for a grain orientation (see arrow in the above figure) of $\varphi = \frac{\pi}{4}$.

These are:

1. Type 1 bonds (green dashed lines) – interactions along all directions $(\phi = 0 \sim 2\pi)$,
2. Type 2 bonds (red solid lines) – interactions along the directions of $\phi = \frac{1}{4}\pi, \frac{3}{4}\pi, \frac{5}{4}\pi, \frac{7}{4}\pi$,

where ϕ represents the angle between the orientation of the bond and the crystal (grain) orientation. As an example, bonds within the horizon of a particular material point for a grain orientation of $\varphi = \dfrac{\pi}{4}$ are shown in Figure 14.

According to OSB PD theory, the strain energy density of a material point can be written as (Madenci and Oterkus, 2014):

$$\begin{aligned} W_{(k)} &= a\theta_{(k)}^2 + b_{T1}\int_H \frac{\delta}{\left|\mathbf{x}'-\mathbf{x}\right|}\left(\left|\mathbf{y}'-\mathbf{y}\right|-\left|\mathbf{x}'-\mathbf{x}\right|\right)^2 dH \\ &+ b_{T2}\sum_{j=1}^{J}\frac{\delta}{\left|\mathbf{x}_{(j)}-\mathbf{x}_{(k)}\right|}\left(\left|\mathbf{y}_{(j)}-\mathbf{y}_{(k)}\right|-\left|\mathbf{x}_{(j)}-\mathbf{x}_{(k)}\right|\right)^2 V_{(j)} \end{aligned} \tag{34}$$

where J is the total number of Type-2 bonds within the family of material points $x_{(k)}$.

By using the strain energy density expression given in Equation (34), the peridynamic force densities $\mathbf{t}$ and $\mathbf{t}'$ can be obtained as:

$$\mathbf{t}\left(\mathbf{u}'-\mathbf{u},\mathbf{x}'-\mathbf{x},t\right) = \frac{1}{2}A\frac{\mathbf{y}'-\mathbf{y}}{\left|\mathbf{y}'-\mathbf{y}\right|} \tag{35}$$

where

$$A = 4ad\frac{\delta}{\left|\mathbf{x}'-\mathbf{x}\right|}\Lambda\theta + 4\delta\left(b_{T1}+\mu_{T2}b_{T2}\right)s \tag{36}$$

with

$$\mu_{T2} = \begin{cases} 1 & \text{Type-2 bonds} \\ 0 & \text{otherwise} \end{cases} \tag{37}$$

and

$$\mathbf{t}'\left(\mathbf{u}'-\mathbf{u},\mathbf{x}'-\mathbf{x},t\right)=-\frac{1}{2}B\frac{\mathbf{y}'-\mathbf{y}}{\left|\mathbf{y}'-\mathbf{y}\right|} \tag{38}$$

where

$$B=4ad\frac{\delta}{\left|\mathbf{x}'-\mathbf{x}\right|}\Lambda\theta'+4\delta\left(b_{T1}+\mu_{T2}b_{T2}\right)s \tag{39}$$

In Equations (35) and (38), $\mathbf{y}$ and $\mathbf{y}'$ represent the location of material points $\mathbf{x}$ and $\mathbf{x}'$ after deformation, i.e., $\mathbf{y}=\mathbf{x}+\mathbf{u}$ and $\mathbf{y}'=\mathbf{x}'+\mathbf{u}'$ (see Figure 8). The PD dilatation, θ, for a crystal can be expressed as:

$$\theta_{(k)}=d\int_{H}\frac{\delta}{\left|\mathbf{x}'-\mathbf{x}\right|}\left(\left|\mathbf{y}'-\mathbf{y}\right|-\left|\mathbf{x}'-\mathbf{x}\right|\right)\Lambda dH \tag{40}$$

and the parameter, Λ, can be defined as

$$\Lambda=\left(\frac{\mathbf{y}'-\mathbf{y}}{\left|\mathbf{y}'-\mathbf{y}\right|}\right)\cdot\left(\frac{\mathbf{x}'-\mathbf{x}}{\left|\mathbf{x}'-\mathbf{x}\right|}\right) \tag{41}$$

The stretch parameter s can be expressed as:

$$s=\frac{\left|\mathbf{y}'-\mathbf{y}\right|-\left|\mathbf{x}'-\mathbf{x}\right|}{\left|\mathbf{x}'-\mathbf{x}\right|} \tag{42}$$

The PD material parameter a is associated with the deformation involving dilatation, $\theta_{(k)}$. The remaining material parameters, b_{T1} and b_{T2}, are associated with deformation of the bonds along the Type 1 and Type 2 bond directions, respectively, as shown in Figure 14. All PD material constants can be expressed in terms of

material constants of a cubic crystal, Q_{ij}, from classical theory. the procedure for obtaining these relationships is presented in Section 3.3.

When the stretch, $s_{(k)(j)}$ between material points k and j exceeds a critical stretch value, s_c, the interaction breaks and damage occurs. Hence, there will no longer be any interaction between these two particles. The critical stretch parameter (2D) can be expressed as (Madenci and Oterkus, 2014):

$$s_c = \sqrt{\frac{G_c}{\left(\frac{6}{\pi}\mu + \frac{16}{9\pi^2}(\kappa - 2\mu)\right)\delta}} \tag{43}$$

where μ represents the shear modulus and κ is the bulk modulus of the material. According to (Anderson, 2005), the critical energy release rate G_c can be obtained from fracture toughness K_{Ic}, as:

$$G_c = \frac{K_{Ic}^2}{E} \quad \text{plane stress} \tag{44}$$

where E is the Young's modulus.

An "interface strength coefficient" is introduced by (Askari *et al.*, 2008) to investigate various fracture modes (intergranular/transgranular) of polycrystalline materials and is defined as:

$$\beta = \frac{s_c^{GB}}{s_c^{GI}} \tag{45}$$

where s_c^{GB} and s_c^{GI} denote the critical stretch of interactions that cross the grain boundary and the critical stretch of interactions that are located within the grain, respectively, i.e., GB represents the grain boundary and GI represents the grain interior.

3.3. Derivation of PD Parameters

The PD material parameters, a, d, b_{T1} and b_{T2}, that appear in the force density vector-stretch relations for in-plane deformation of a cubic crystal can be related to the engineering constants by considering three different simple loading conditions:

1. Simple shear: $\gamma_{12} = \zeta$;
2. Uniaxial stretch in crystal orientation direction: $\varepsilon_{11} = \zeta$, $\varepsilon_{22} = 0$;
3. Biaxial stretch: $\varepsilon_{11} = \zeta$, $\varepsilon_{22} = \zeta$.

3.3.1. First Loading Condition (Simple Shear $\gamma_{12} = \zeta$)

In the first loading condition, a constant simple shear strain is applied as shown in Figure 15 and the corresponding dilatation and strain energy density from CCM can be expressed as:

$$\theta_{(k)}^{CCM} = 0 \tag{46}$$

And

$$W_{(k)}^{CCM} = \frac{1}{2} Q_{44} \zeta^2 \tag{47}$$

For this loading condition, the length of the relative position of material points $\mathbf{y}_{(j)}$ and $\mathbf{y}_{(k)}$ in the deformed state becomes:

$$\left|\mathbf{y}_{(j)}-\mathbf{y}_{(k)}\right|=\left[1+\left(\sin\phi_{(j)(k)}\cos\phi_{(j)}\right)\zeta\right]\left|\mathbf{x}_{(j)}-\mathbf{x}_{(k)}\right| \tag{48}$$

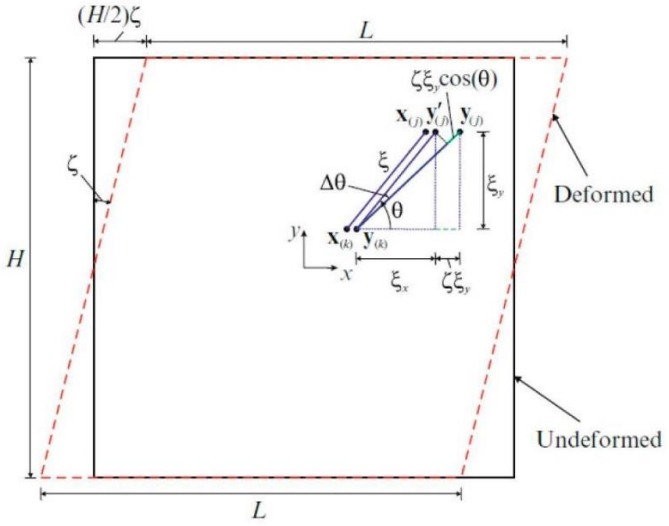

Figure 15. Simple shear loading condition (x: crystal orientation direction)

The PD dilatation term can be evaluated as:

$$\theta_{(k)}^{PD}=d\int_{H}\frac{\delta}{\xi}\left\{\left[1+\left(\sin\phi\cos\phi\right)\zeta\right]\xi-\xi\right\}dH=0 \tag{49}$$

in which $\xi=\left|\mathbf{x}_{(j)}-\mathbf{x}_{(k)}\right|$. As expected, there is no dilatation for this loading condition.

Therefore, the strain energy density can be calculated as:

$$\begin{aligned}W_{(k)}^{PD}&=a(0)+b_{T1}\int_{H}\frac{\delta}{\xi}\left\{\left[1+\left(\sin\phi\cos\phi\right)\zeta\right]\xi-\xi\right\}^{2}dH\\&+b_{T2}\sum_{j=1}^{J}\frac{\delta}{\left|\mathbf{x}_{(j)}-\mathbf{x}_{(k)}\right|}\left[\left(\sin\phi_{(j)(k)}\cos\phi_{(j)(k)}\right)\zeta\left|\mathbf{x}_{(j)}-\mathbf{x}_{(k)}\right|\right]^{2}V_{(j)}\end{aligned} \tag{50}$$

or

$$W_{(k)}^{PD} = \left(\frac{\pi h \delta^4 \zeta^2}{12} \right) b_{T1} + \left(\frac{\delta \zeta^2}{4} \sum_{j=1}^{J} \xi_{(j)(k)} V_{(j)} \right) b_{T2} \tag{51}$$

Equating expressions of strain energy density from CCM and OSB PD formulations, i.e., Equations (47) and (51), results in:

$$\left(\frac{\pi h \delta^4}{12} \right) b_{T1} + \left(\frac{\delta}{4} \sum_{j=1}^{J} \xi_{(j)(k)} V_{(j)} \right) b_{T2} = \frac{Q_{44}}{2} \tag{52}$$

3.3.2. Second Loading Condition (Uniaxial Stretch in Crystal Orientation Direction: $\varepsilon_{11} = \zeta$, $\varepsilon_{22} = 0$)

In the second loading condition, a constant strain is applied along the direction of crystal orientation (Figure 16), and the corresponding dilatation and strain energy density from CCM can be expressed as:

$$\theta_{(k)}^{CCM} = \zeta \tag{53}$$

and

$$W_{(k)}^{CCM} = \frac{1}{2} Q_{11} \zeta^2 \tag{54}$$

The length of the relative position of material points $\mathbf{y}_{(j)}$ and $\mathbf{y}_{(k)}$ in the deformed state becomes:

$$\left| \mathbf{y}_{(j)} - \mathbf{y}_{(k)} \right| = \left[1 + \left(\cos^2 \phi_{(j)(k)} \right) \zeta \right] \left| \mathbf{x}_{(j)} - \mathbf{x}_{(k)} \right| \tag{55}$$

Due to this deformation, the dilatation of PD can be evaluated as:

$$\theta_{(k)}^{PD} = d\int_{H}\frac{\delta}{\xi}\left\{\left[1+\left(\cos^2\phi\right)\zeta\right]\xi-\xi\right\}dH \tag{56}$$

or

$$\theta_{(k)}^{PD} = \frac{\pi dh\delta^3\zeta}{2} \tag{57}$$

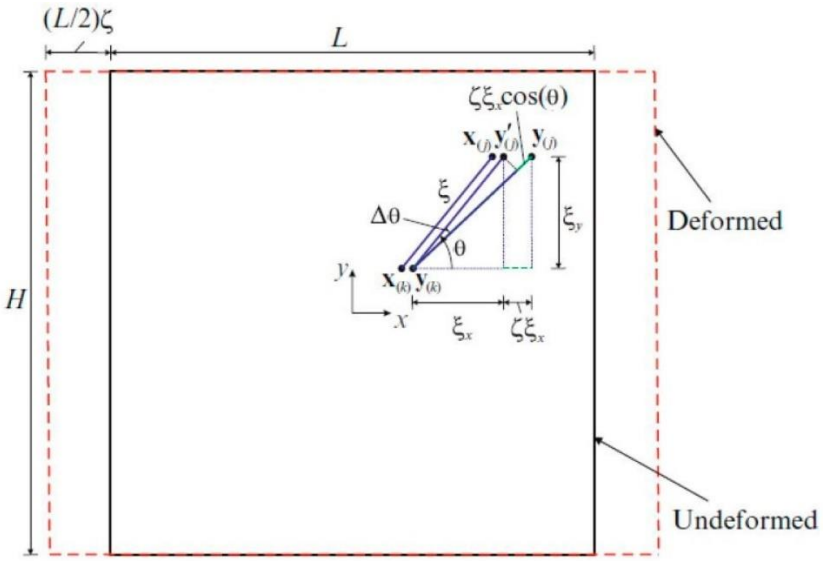

Figure 16. Uniaxial loading condition in crystal orientation direction, x.

By equating expressions of the dilatation term from CCM and PD formulations, i.e., Equations (53) and (57), results in:

$$d = \frac{2}{\pi h\delta^3} \tag{58}$$

The PD strain energy density for this loading condition can be calculated as:

$$\begin{aligned} W_{(k)}^{PD} &= a\zeta^2 + b_{T1}\int_{H}\frac{\delta}{\xi}\left\{\left[1+\left(\cos^2\phi\right)\zeta\right]\xi-\xi\right\}^2 dH \\ &+ b_{T2}\sum_{j=1}^{J}\frac{\delta}{\left|\mathbf{x}_{(j)}-\mathbf{x}_{(k)}\right|}\left[\left(\cos^2\phi_{(j)(k)}\right)\zeta\left|\mathbf{x}_{(j)}-\mathbf{x}_{(k)}\right|\right]^2 V_{(j)} \end{aligned} \tag{59}$$

or

$$W_{(k)}^{PD} = a\zeta^2 + \left(\frac{\pi h\delta^4\zeta^2}{4}\right)b_{T1} + \left(\frac{\delta\zeta^2}{4}\sum_{j=1}^{J}\xi_{(j)(k)}V_{(j)}\right)b_{T2} \tag{60}$$

Hence, by equating expressions of strain energy density from Equations (54) and (60), the following relationship can be obtained:

$$a + \left(\frac{\pi h\delta^4}{4}\right)b_{T1} + \left(\frac{\delta}{4}\sum_{j=1}^{J}\xi_{(j)(k)}V_{(j)}\right)b_{T2} = \frac{1}{2}Q_{11} \tag{61}$$

3.3.3. Third Loading Condition (Biaxial Stretch: $\varepsilon_{11} = \zeta$, $\varepsilon_{22} = \zeta$)

In the third loading condition, a constant strain is applied in all directions (Figure 17), and the corresponding dilatation and strain energy density from CCM can be expressed as:

$$\theta_{(k)}^{CCM} = 2\zeta \tag{62}$$

and

$$W_{(k)}^{CCM} = \left(Q_{11} + Q_{12}\right)\zeta^2 \tag{63}$$

The length of the relative position under this loading condition can be evaluated as:

$$\left|\mathbf{y}_{(j)} - \mathbf{y}_{(k)}\right| = \left[1 + \left(\cos^2\phi_{(j)(k)} + \sin^2\phi_{(j)(k)}\right)\zeta\right]\left|\mathbf{x}_{(j)} - \mathbf{x}_{(k)}\right| \tag{64}$$

Hence, the dilatation term in PD formulation can be expressed as:

$$\theta_{(k)}^{PD} = d\int_H \frac{\delta}{\xi}\left\{\left[1+\zeta\right]\xi - \xi\right\}dH \tag{65}$$

or

$$\theta_{(k)}^{PD} = \pi dh\delta^3\zeta \tag{66}$$

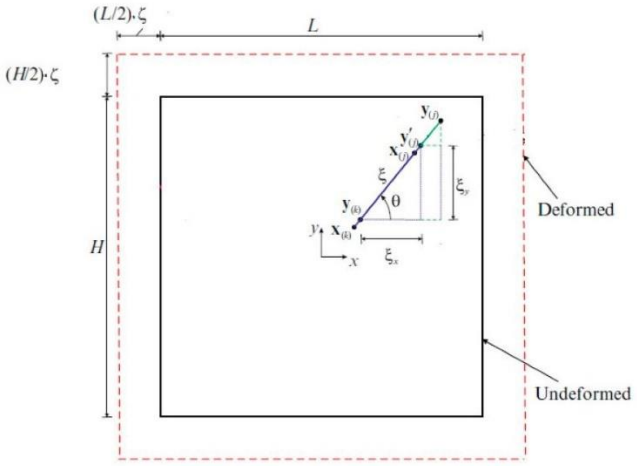

Figure 17. Biaxial Stretch Loading Condition

By equating the expressions of dilatation from both CCM and PD, i.e., Equations (62) and (66), the same expression given in Equation (58) can be obtained.

Moreover, the PD strain energy density under this loading condition can be evaluated as:

$$\begin{aligned} W_{(k)}^{PD} &= a\zeta^2 + b_{T1}\int_H \frac{\delta}{\xi}\left\{\left[1+\left(\sin^2\phi\right)\zeta\right]\xi-\xi\right\}^2 dH \\ &+b_{T2}\delta\zeta^2\left(\sum_{j=1}^{J}\left|\mathbf{x}_{(j)}-\mathbf{x}_{(k)}\right|V_{(j)}\right) \end{aligned} \tag{67}$$

By equating Equations (63) and (67), a new relationship can be obtained, as:

$$Q_{11}+Q_{12} = 4a+\left(\frac{2\pi h\delta^4}{3}\right)b_{T1}+\left(\delta\sum_{j=1}^{J}\xi_{(j)(k)}V_{(j)}\right)b_{T2} \tag{68}$$

Hence, the OSB PD material parameters can be expressed in terms of engineering constants of CCM by utilizing the three relationships given in Equations (52), (61) and (68) as:

$$\begin{cases} a = \dfrac{1}{2}\left(Q_{12} - Q_{44}\right) \\ b_{T1} = \dfrac{3\left(Q_{11} - Q_{12}\right)}{\pi h \delta^4} \\ b_{T2} = \dfrac{2Q_{44} - Q_{11} + Q_{12}}{\delta\left(\sum_{j=1}^{J}\left|\mathbf{x}_{(j)}^{n} - \mathbf{x}_{(k)}^{n}\right| V_{(j)}\right)} \\ d = \dfrac{2}{\pi h \delta^3} \end{cases} \tag{69}$$

For BB PD, the parameter a associated with dilatation should vanish, leading to the constraint equation $Q_{12} = Q_{44}$, which is a limitation of BB PD in cubic polycrystal analysis.

3.4. Numerical Results and Discussion

In this section, the results generated from static and dynamic PD analyses are presented, and comparisons with FEM results are also provided. For static analysis, a single cubic Niobium (Nb) crystal model is considered first and displacement fields of PD and FEM are compared. Then, a cubic Molybdenum (Mo) polycrystal model with 18 Voronoi grains is analysed, and the PD and FEM displacement fields are compared. For the dynamic analysis, the influence of the discretization size and the interface strength coefficient (β) on the results is considered first. Then the influence of crystal size on fracture behaviour is investigated.

3.4.1. Material data

Two different materials are considered in this study: niobium (Nb) for single crystal static analysis, and molybdenum (Mo) for polycrystal static and dynamic analysis. According to (Hosford, 1993), the local stiffness matrix of each individual crystal can be written as:

$$[C]=\begin{bmatrix} C_{11} & C_{12} & C_{12} & 0 & 0 & 0 \\ C_{12} & C_{11} & C_{12} & 0 & 0 & 0 \\ C_{12} & C_{12} & C_{11} & 0 & 0 & 0 \\ 0 & 0 & 0 & C_{44} & 0 & 0 \\ 0 & 0 & 0 & 0 & C_{44} & 0 \\ 0 & 0 & 0 & 0 & 0 & C_{44} \end{bmatrix} \tag{70}$$

However, for plane stress configuration, the material matrix given in Equation (70) can be written by using reduced stiffness matrix following the procedure given in (Kaw, 2005) as:

$$[Q]=\begin{bmatrix} Q_{11} & Q_{12} & 0 \\ Q_{12} & Q_{11} & 0 \\ 0 & 0 & Q_{44} \end{bmatrix} \tag{71}$$

where Q_{ij} are the reduced stiffness coefficients and can be expressed in terms of the elements of the stiffness matrix, C_{ij} as:

$$\begin{aligned} Q_{11} &= \frac{C_{11}{}^2 - C_{12}{}^2}{C_{11}} \\ Q_{12} &= \frac{C_{11}C_{12} - C_{12}{}^2}{C_{11}} \\ Q_{44} &= C_{44} \end{aligned} \tag{72}$$

Therefore, the material properties of Nb and Mo are given in Table 1 as shown below (Kaw, 2005):

Table 1. Material properties of Niobium and Molybdenum

Niobium				**Molybdenum**			
C_{11}	239.8 GPa	Q_{11}	174.4 GPa	C_{11}	441.6 GPa	Q_{11}	374.5 GPa
C_{12}	125.2 GPa	Q_{12}	59.82 GPa	C_{12}	172.7 GPa	Q_{12}	105.4 GPa
C_{44}	28.22 GPa	Q_{44}	28.22 GPa	C_{44}	121.9 GPa	Q_{44}	121.9 GPa

The fracture toughness of Mo is specified as $K_{Ic} = 24.2$ MPa$\sqrt{m}$ (Sturm *et al.*, 2007), which corresponds to a critical stretch value of 0.008127 for plane stress configuration.

3.4.2. Static analysis

A cubic crystal model with a length of $152.4\ \mu$m and a width of $76.2\ \mu$m is considered and the number of particles along the horizontal and vertical directions is 240 and 120, respectively. The values of grid spacing and horizon are $\Delta x = 0.635\ \mu$m and $\delta = 1.915\ \mu$m, respectively. A uniform discretization scheme is used throughout this study. However, non-uniform discretization can also be possible by using small grid sizes at critical regions such as interfaces and utilizing the "Dual-horizon peridynamics" concept, as introduced by (Ren *et al.*, 2016, Ren, Zhuang and Rabczuk, 2016). A horizontal tension loading of P is applied on the right edge of the model and the left edge is fully fixed as shown in Figure 18. The tension loading is specified as a body load and applied to a single layer of material points at the right edge of the model. The displacement constraint condition at the left edge is also imposed to a single layer of material points. To reach the steady-state condition and perform static analysis, an ADR technique was utilized as described in (Madenci and Oterkus, 2014).

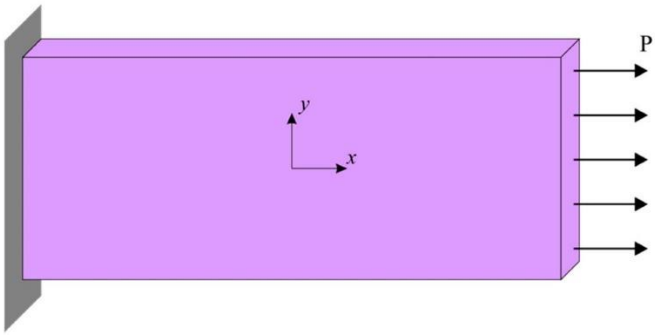

Figure 18. Crystal Model for Static Analysis

3.4.2.1. *Static analysis of Nb single crystal*

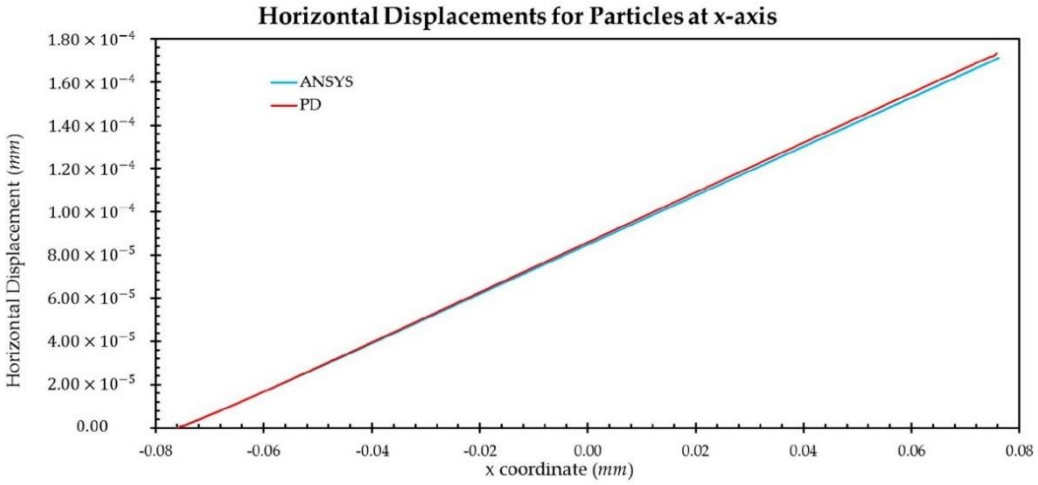

(a)

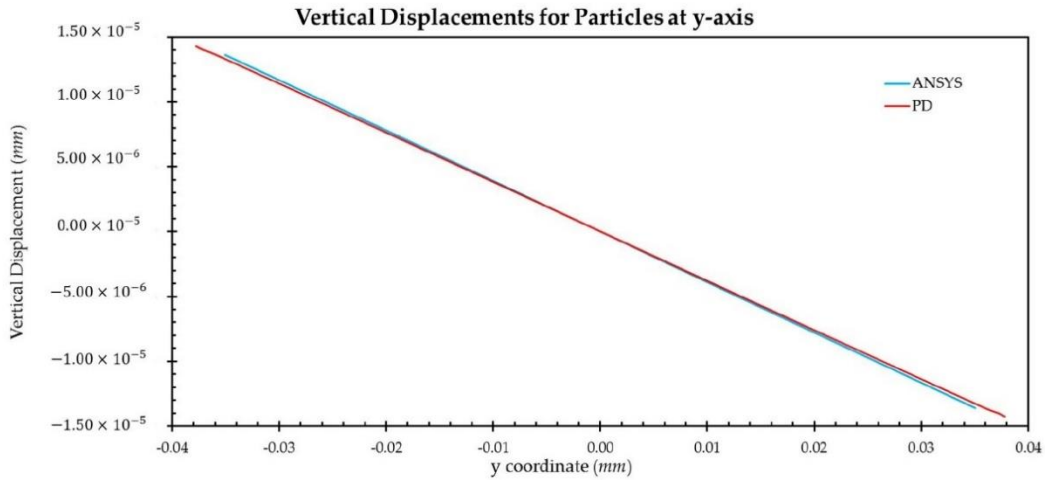

(b)

Figure 19. Comparison of displacements between FEM and PD analyses for Nb crystal for 0° orientation: (a) horizontal displacements for particles along the central x-axis; (b) vertical displacements for particles along the central y-axis

The tension loading applied on the right edge of the model is $P = 174.4$ MPa . In ANSYS, the plate was modelled using PLANE 182, with total of 5000 elements. Figure 19 and Figure 20 show a comparison of the results obtained from FEM and PD analysis under plane stress conditions for crystal orientations of 0° and 45°, respectively. Particles located along the central x-axis and y-axis are selected and horizontal and vertical displacements are compared, respectively.

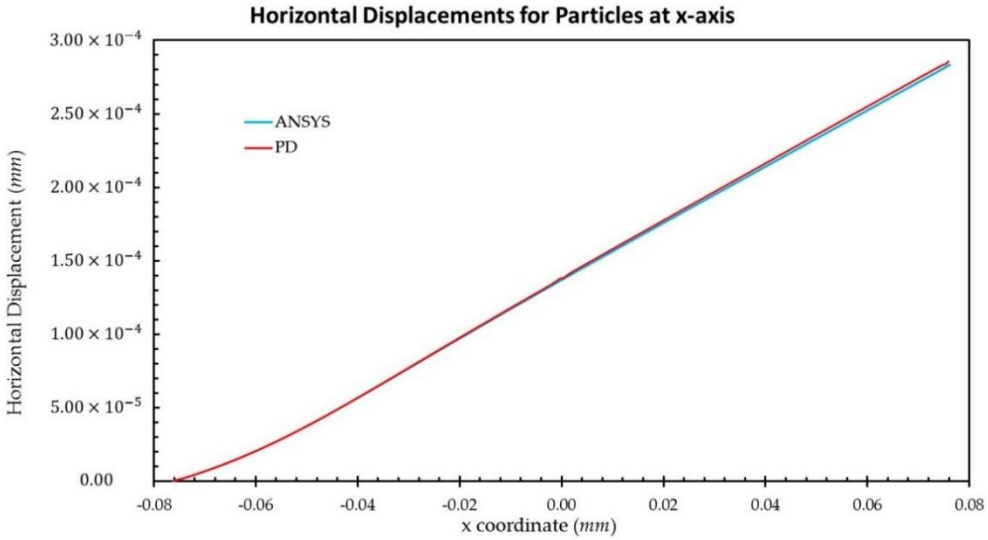

(a)

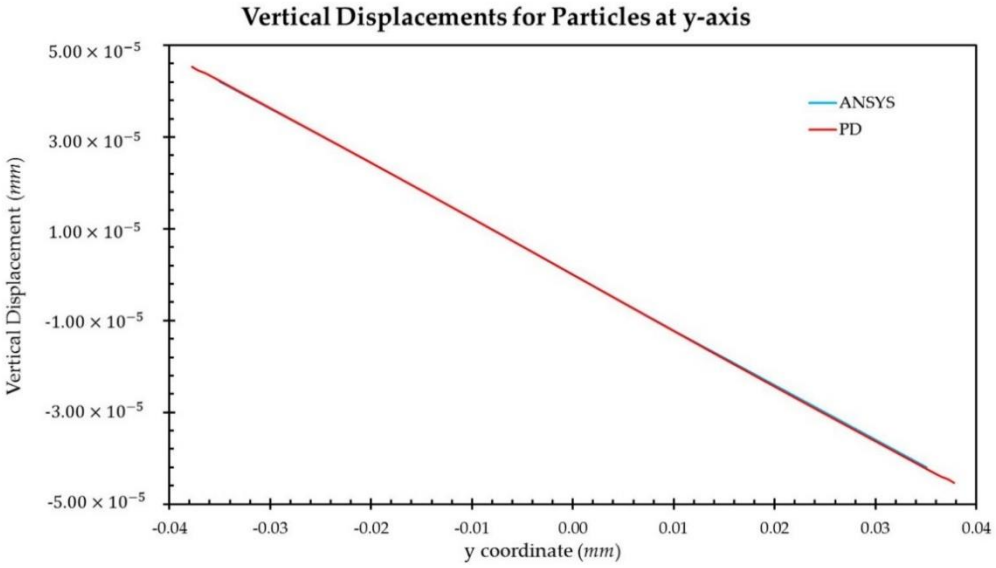

(b)

Figure 20. Comparison of displacements between FEM and PD analyses for Nb Crystal for 45° orientation: (a) horizontal displacements for particles along the central x-axis; (b) vertical displacements for particles along the central y-axis

Based on the results presented in Figure 19 and Figure 20, good agreement is obtained between PD and FEM analyses. Therefore, it can be concluded that the OSB PD crystal model presented in this study can produce accurate results for different crystal orientations for a single crystal.

3.4.2.2. Static analysis of Mo polycrystal

In the second case, a polycrystal model with 18 randomly orientated grains is generated by using Voronoi tessellation. A uniform discretization is utilized. Depending on the location of the material point, corresponding grain orientation is determined. Hence, Type 2 bonds will exist in many different directions according to the random orientation of the crystals. The average crystal size is $645.16\ \mu\text{m}^2$ and the amount of tension loading applied on the right edge is $P = 374.5$ MPa. The layout of the polycrystal model is shown in Figure 21. Similar with the single crystal

model described in previous section, PLANE 182 was used as element type, and total number of 3087 elements was modelled.

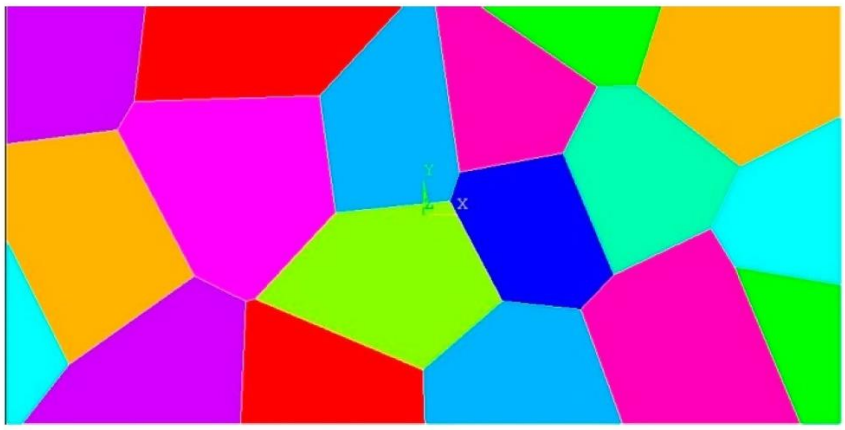

Figure 21. Model for the static analysis of Mo polycrystal, composed of 18 randomly orientated grains with respect to the x-y coordinate system located at the centre of the model

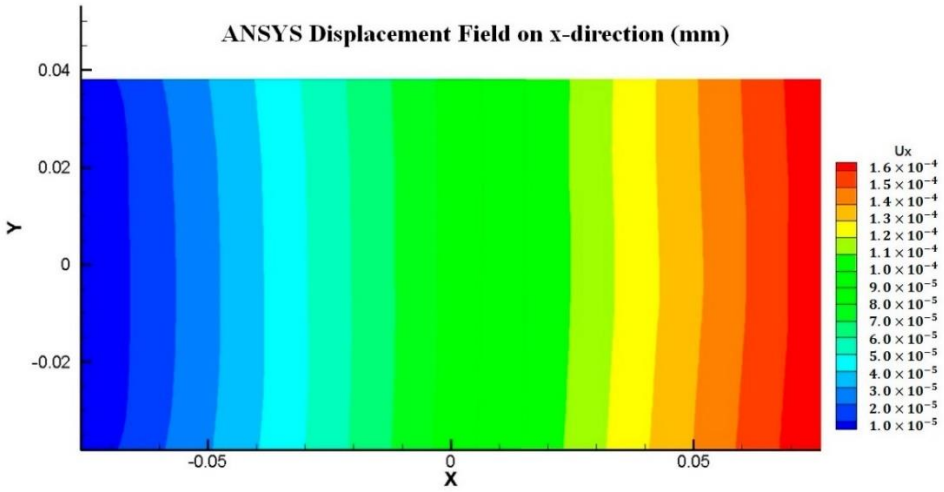

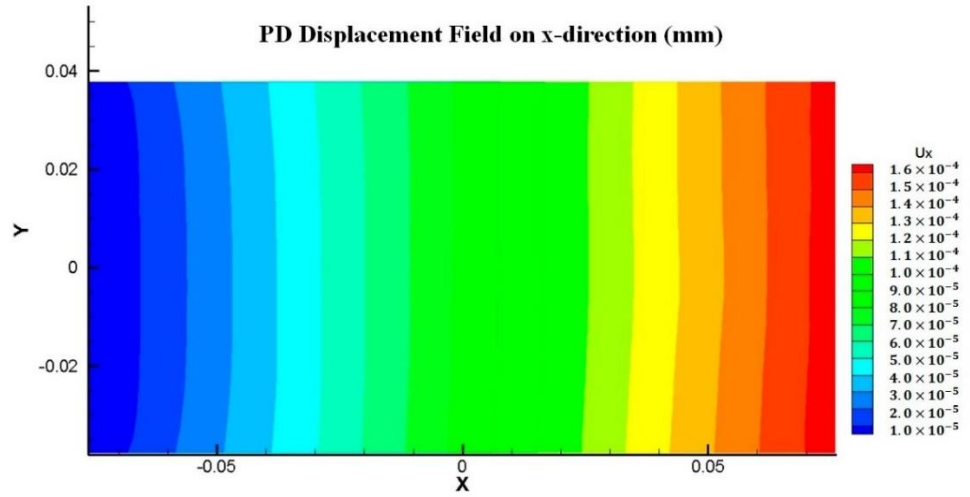

Figure 22. Displacement Field Comparison between FEM and PD Analyses for Mo Polycrystal (x-direction)

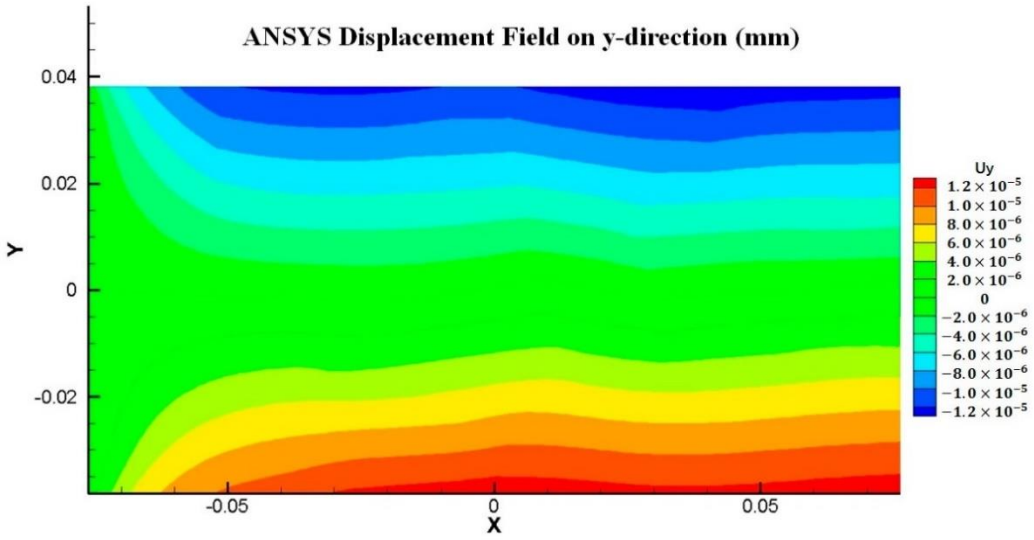

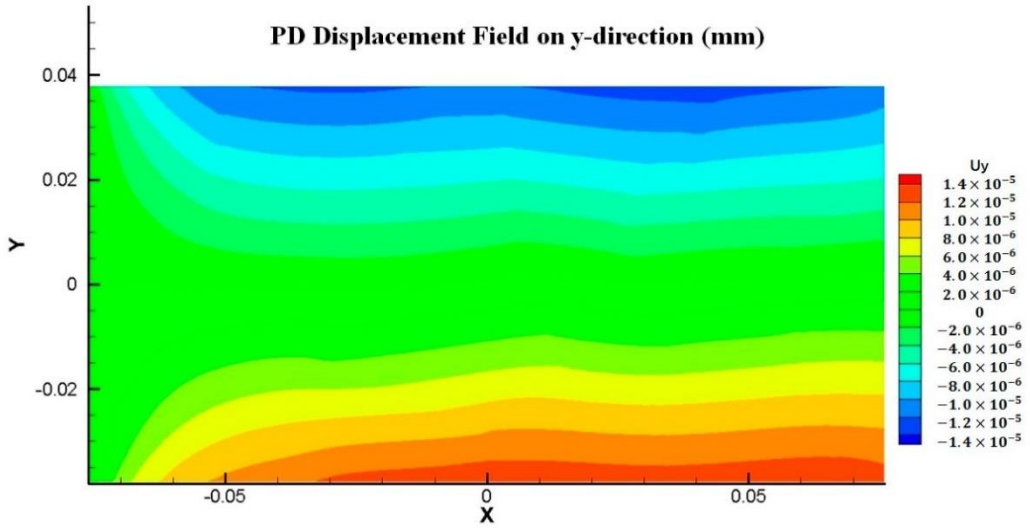

Figure 23. Displacement Field Comparison between FEM and PD Analyses for Mo Polycrystal (y-direction)

3.4.3. Dynamic Analysis of Mo Polycrystal

For the dynamic analysis, a 5 mm by 5 mm square plate with randomly oriented grains is considered as shown in Figure 24. A horizontal velocity boundary condition of $V = 5$ m/s is applied on both the left and right edges of the model. Three layers of virtual particles are placed along the left and right edges to impose this condition, as suggested in (Madenci and Oterkus, 2014). A no-fail zone is also imposed on virtual particles and their neighbouring particles in order to allow the load to be accurately transferred inside the plate. Two pre-existing cracks with a length of 0.4 mm are applied at the center of the bottom and top edges, as shown in Figure 25. The time step size is specified as $dt = 0.05$ ns and the total number of time steps is 100,000, i.e., the total simulation time of $5.0\ \mu$s. The study considers three different interface strength coefficient, β, values (0.5, 1.0, and 2.0), three different mesh sizes (74×74, 150×150, and 300×300) and three different total number of grains (25, 100, and 400; i.e., different crystal sizes).

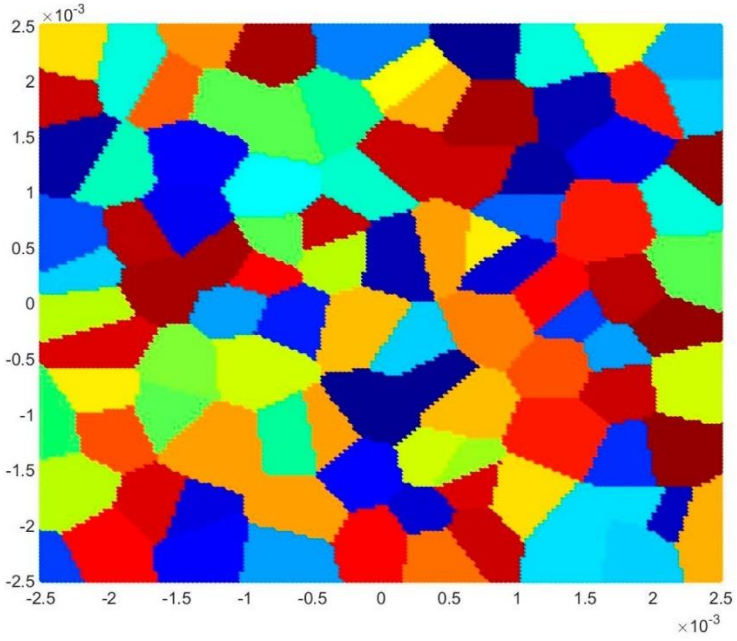

Figure 24. Polycrystal model for Dynamic Analysis (100 grains)

3.4.3.1. Effect of PD Discretization Size and Interface Strength Coefficient (β)

The aim of this analysis is to investigate the effect of the peridynamic discretization size on the crack pattern predicted by PD model and the morphology of intergranular and transgranular fracture modes when changing the value of the interface strength coefficient, β. The horizon is specified as $\delta = 3.015 \cdot \Delta x$, which means that it is controlled by changing the PD discretization (74×74 particles, 150×150 particles, and 300×300 particles). Moreover, three different interface strength coefficients, β, values are considered to investigate the intergranular and transgranular fracture modes of the polycrystal.

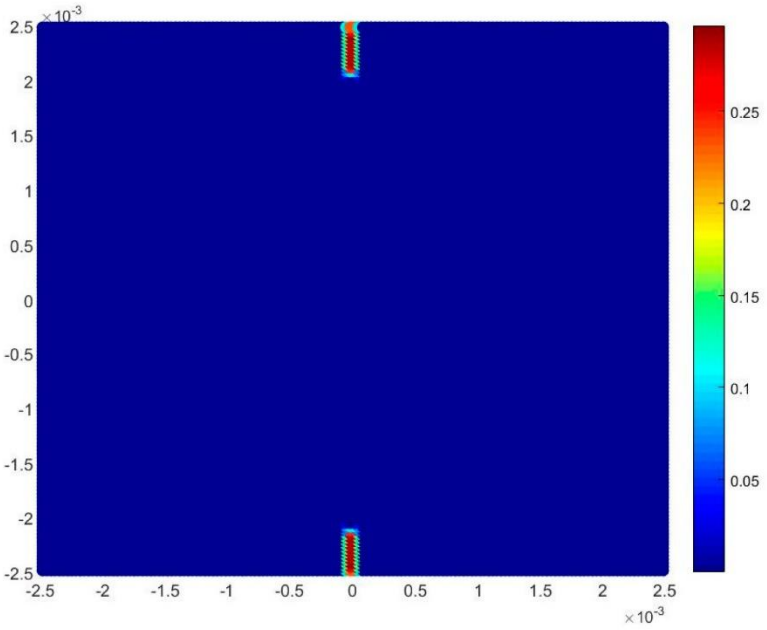

Figure 25. Location of the Cracks in the Model for Dynamic Analysis

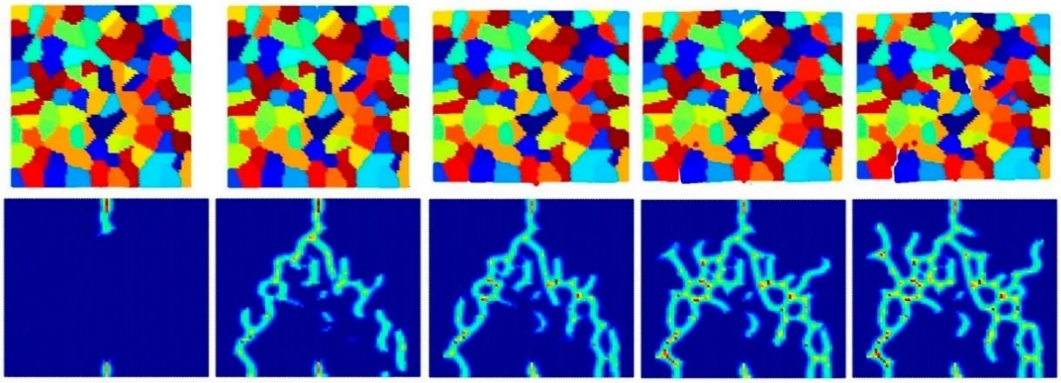

Figure 26. Fracture pattern of polycrystal when $\beta = 0.5$ *with* 74×74 *particles. From left to right:* time = 1.5 μs, 2.0 μs, 2.5 μs, 3.0 μs, and 3.5 μs *, respectively*

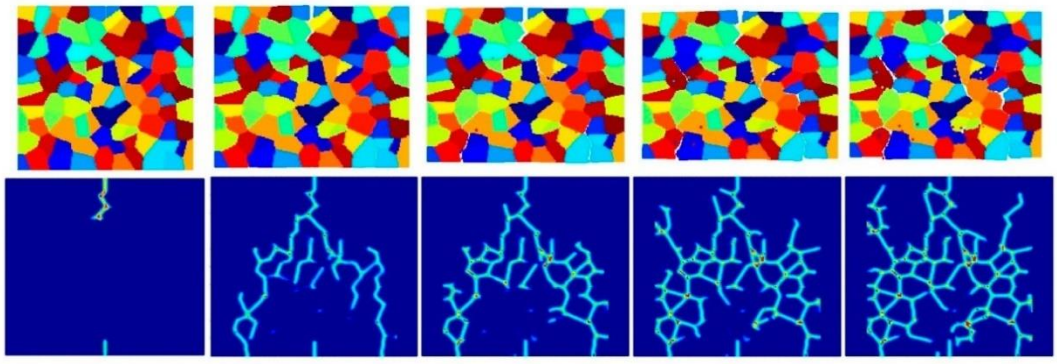

Figure 27. Fracture pattern of polycrystal when $\beta = 0.5$ *with* 150×150 *particles. From left to right:* time = 1.5 μs, 2.0 μs, 2.5 μs, 3.0 μs, and 3.5 μs *, respectively*

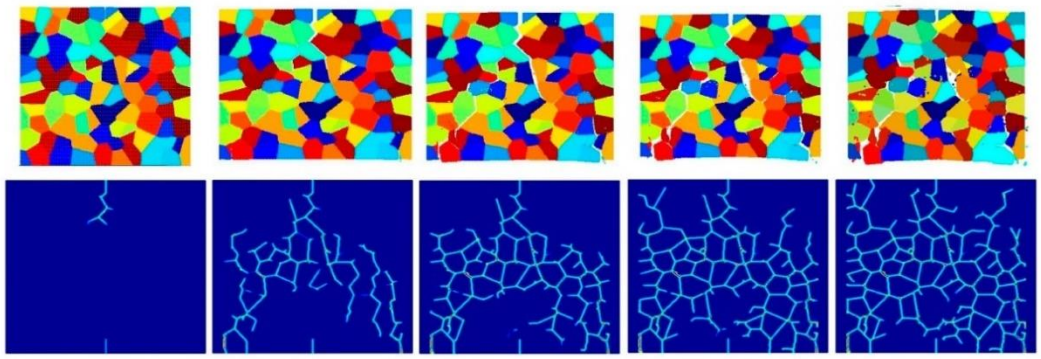

Figure 28. Fracture pattern of polycrystal when $\beta = 0.5$ *with* 300×300 *particles. From left to right:* time = 1.5 μs, 2.0 μs, 2.5 μs, 3.0 μs, and 3.5 μs *, respectively*

Figure 26 - Figure 28 show the fracture pattern of the polycrystal under plane stress configuration at five different times $(1.5\ \mu\text{s}, 2.0\ \mu\text{s}, 2.5\ \mu\text{s}, 3.0\ \mu\text{s}, \text{and } 3.5\ \mu\text{s})$ for $\beta = 0.5$ with 74×74 particles, 150×150 particles, and 300×300 particles, respectively.

The results show that with an increasing total number of particles, the intergranular crack pattern can be predicted more accurately and in more detail. However, the simulation time will increase rapidly as well. Therefore, it is important to find a good balance between accuracy and time. In this study, 150×150 particles can provide appropriate results, which is the reason why most of the simulations in this chapter are chosen by using this number of particles.

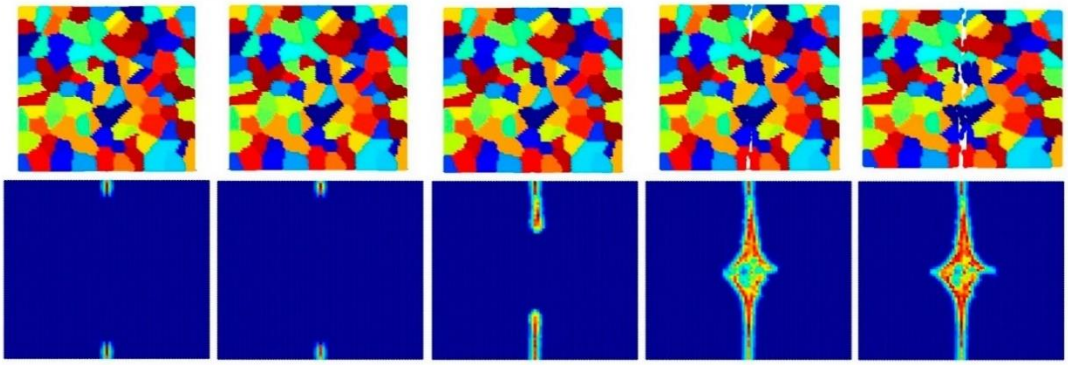

Figure 29. Fracture pattern of polycrystal when $\beta = 1.0$ *with* 74×74 *particles. From left to right:* time = 1.5 μs, 2.0 μs, 2.5 μs, 3.0 μs, and 3.5 μs *, respectively*

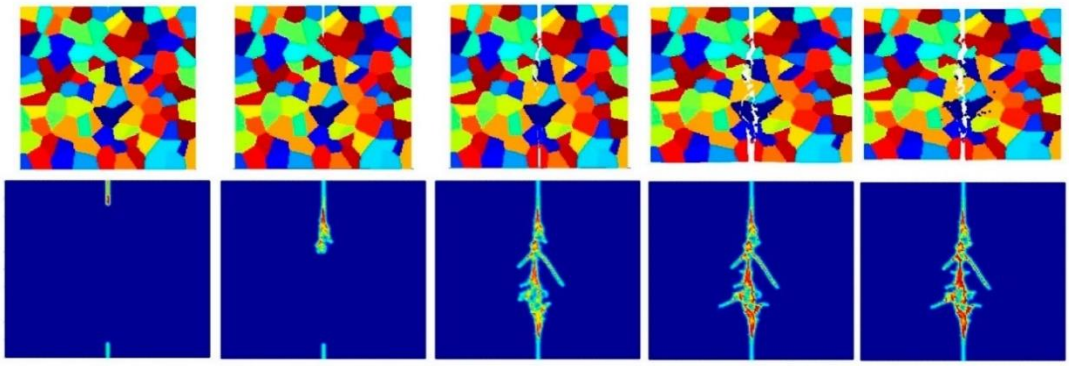

Figure 30. Fracture pattern of polycrystal when $\beta = 1.0$ *with* 150×150 *particles. From left to right:* time = 1.5 μs, 2.0 μs, 2.5 μs, 3.0 μs, and 3.5 μs *, respectively*

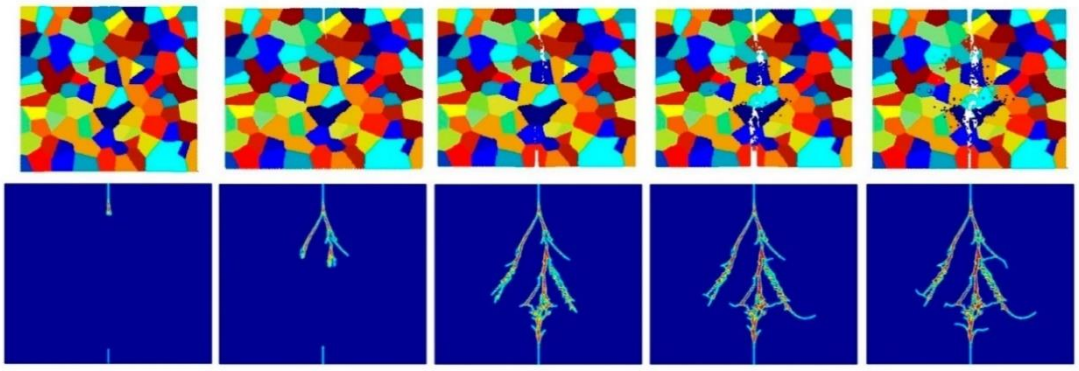

Figure 31. Fracture pattern of polycrystal when $\beta = 1.0$ *with* 300×300 *particles. From left to right:* time = 1.5 μs, 2.0 μs, 2.5 μs, 3.0 μs, and 3.5 μs *, respectively*

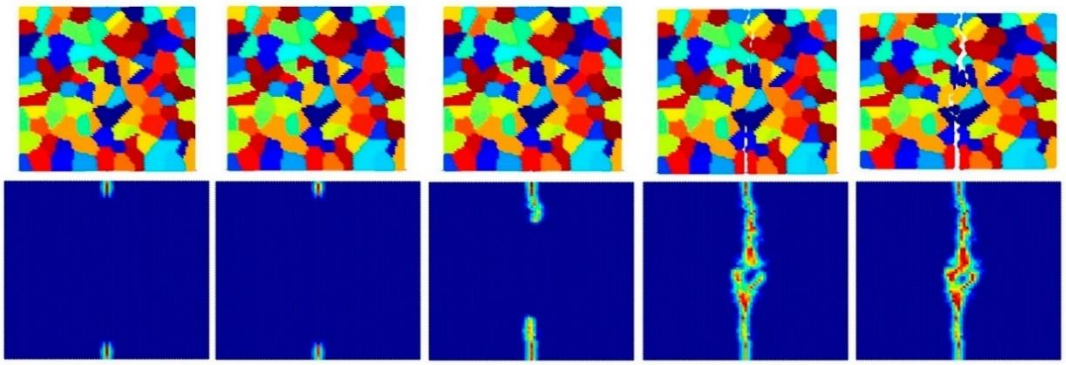

Figure 32. Fracture pattern of polycrystal when $\beta = 2.0$ *with* 74×74 *particles. From left to right:* time = 1.5 μs, 2.0 μs, 2.5 μs, 3.0 μs, and 3.5 μs *, respectively*

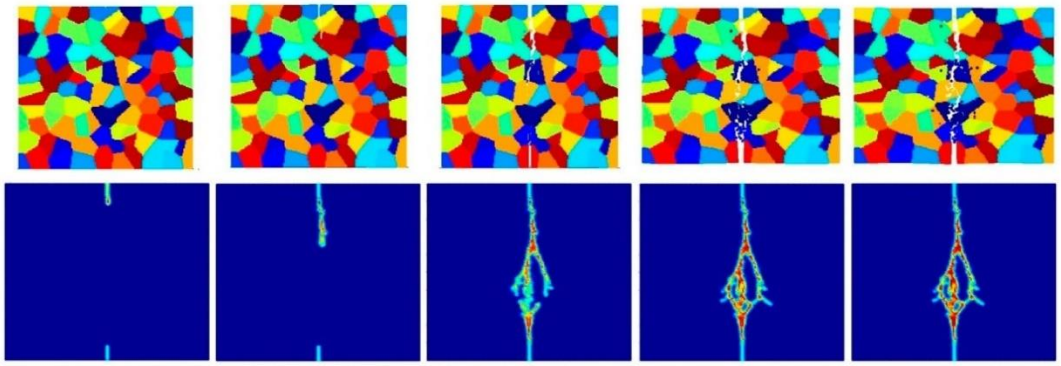

Figure 33. Fracture pattern of polycrystal when $\beta = 2.0$ *with* 150×150 *particles. From left to right:* time = 1.5 μs, 2.0 μs, 2.5 μs, 3.0 μs, and 3.5 μs *, respectively*

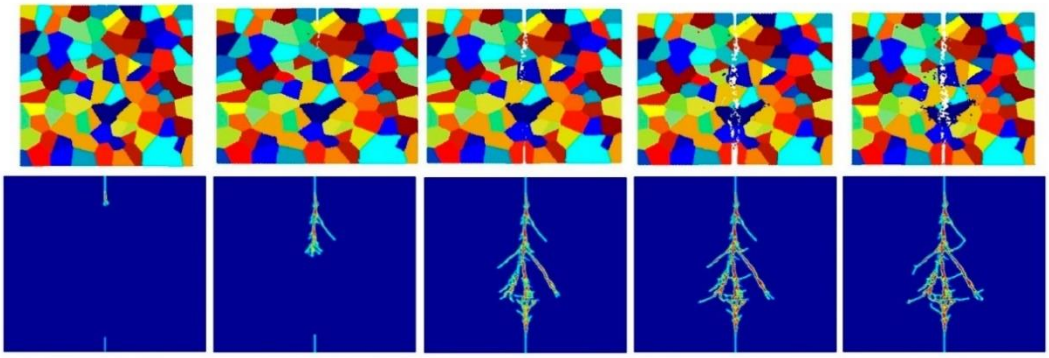

Figure 34. Fracture pattern of polycrystal when $\beta = 2.0$ *with* 300×300 *particles. From left to right:* time = 1.5 μs, 2.0 μs, 2.5 μs, 3.0 μs, and 3.5 μs *, respectively*

Figure 29 - Figure 34 show the fracture patterns of the polycrystal at five different times $(1.5\ \mu s,\ 2.0\ \mu s,\ 2.5\ \mu s,\ 3.0\ \mu s,\ \text{and}\ 3.5\ \mu s)$ for $\beta = 1.0$ and $\beta = 2.0$ with 74×74 particles, 150×150 particles, and 300×300 particles, respectively.

As described above, similar conclusions can be found in these simulations. For instance, branching of cracks can be obtained more clearly by increasing the total number of particles, but the simulations become more time-consuming. Moreover, the transgranular fracture mode becomes more dominant as the interface strength coefficient increases.

3.4.3.2. Effect of the crystal size

The aim of this section is to investigate the effect of the crystal size on fracture pattern. The plate is discretized by 150×150 particles, containing three different numbers of randomly orientated grains (25 grains, 100 grains, and 400 grains). Three different grain boundary strength coefficients, $\beta = 0.5$, $\beta = 1.0$ and $\beta = 2.0$ are considered to investigate the effect of crystal size for different fracture modes.

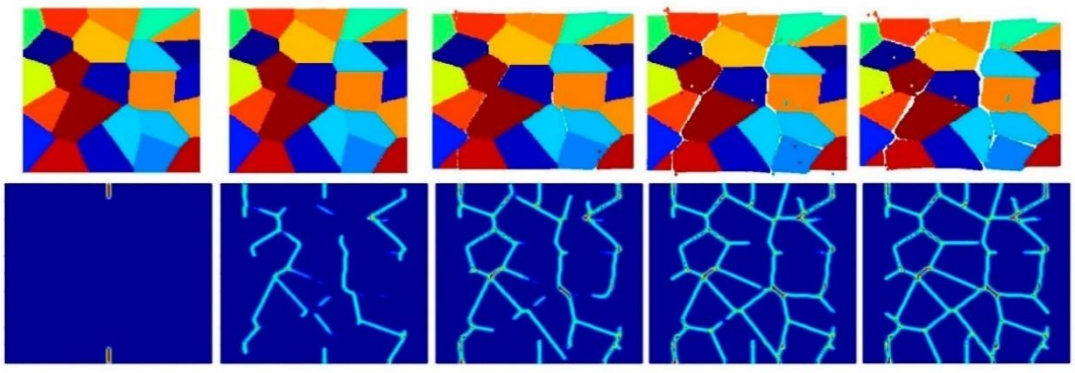

Figure 35. Fracture pattern of polycrystal when $\beta = 0.5$ with 25 grains in total. From left to right: time = 1.5 μs, 2.0 μs, 2.5 μs, 3.0 μs, and 3.5 μs *, respectively*

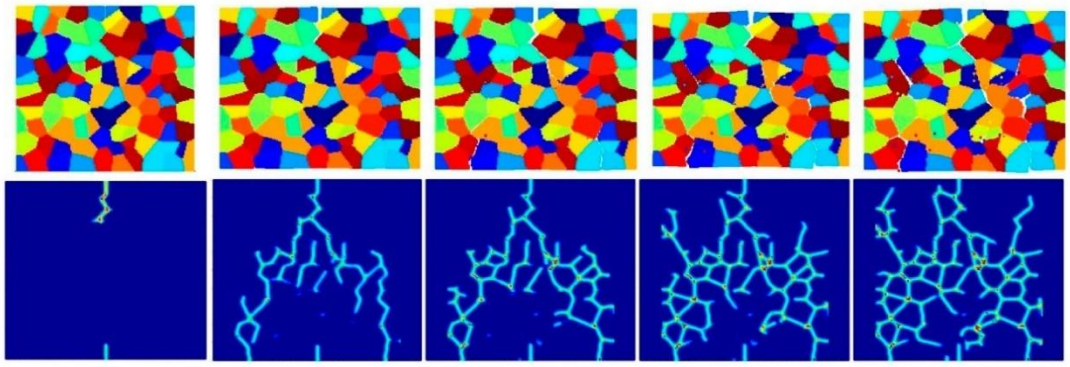

Figure 36. Fracture pattern of polycrystal when $\beta = 0.5$ *with 100 grains in total. From left to right:* time = 1.5 μs, 2.0 μs, 2.5 μs, 3.0 μs, and 3.5 μs *, respectively*

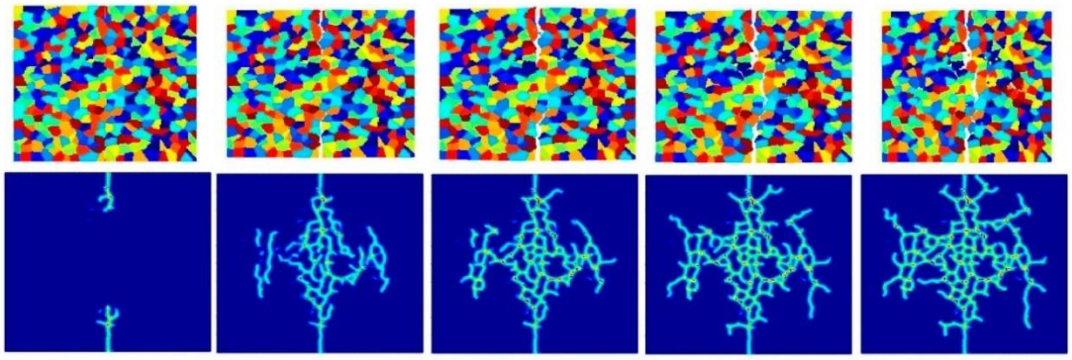

Figure 37. Fracture pattern of polycrystal when $\beta = 0.5$ *with 400 grains in total. From left to right:* time = 1.5 μs, 2.0 μs, 2.5 μs, 3.0 μs, and 3.5 μs *, respectively*

Figure 35 - Figure 37 show the fracture pattern of the polycrystal at five different times $(1.5\ \mu s, 2.0\ \mu s, 2.5\ \mu s, 3.0\ \mu s, \text{and } 3.5\ \mu s)$ for $\beta = 0.5$ with 25 grains, 100 grains, and 400 grains, respectively.

According to the damage plots shown in Figure 35 with 25 grains at $2.0\ \mu s$, the propagation does not always occur from pre-existing cracks. Only the top pre-existing crack propagates in the 100-grain model and both pre-existing cracks propagate in the 400-grain model. This is because with an increase in the total number of grains, the probability of the pre-existing cracks being located on a grain boundary increases. In other words, since the grain boundary strength $\beta = 0.5$ promotes intergranular fracture mode, the crack can more easily propagate if it is

located on the grain boundary. However, for the grain boundary strength values of $\beta = 1.0$ and $\beta = 2.0$, there is no such difference observed in fracture behaviour and both pre-existing cracks propagate as shown in Figure 38 - Figure 43.

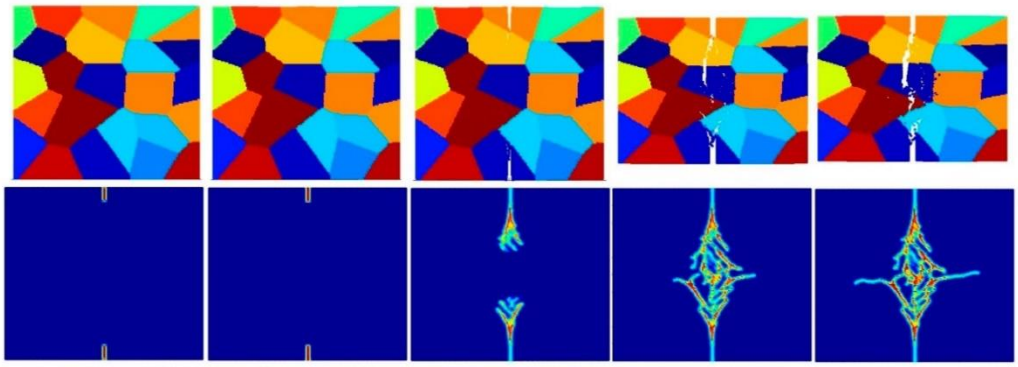

Figure 38. Fracture pattern of polycrystal when $\beta = 1.0$ with 25 grains in total. From left to right: time = 1.5 μs, 2.0 μs, 2.5 μs, 3.0 μs, and 3.5 μs *, respectively*

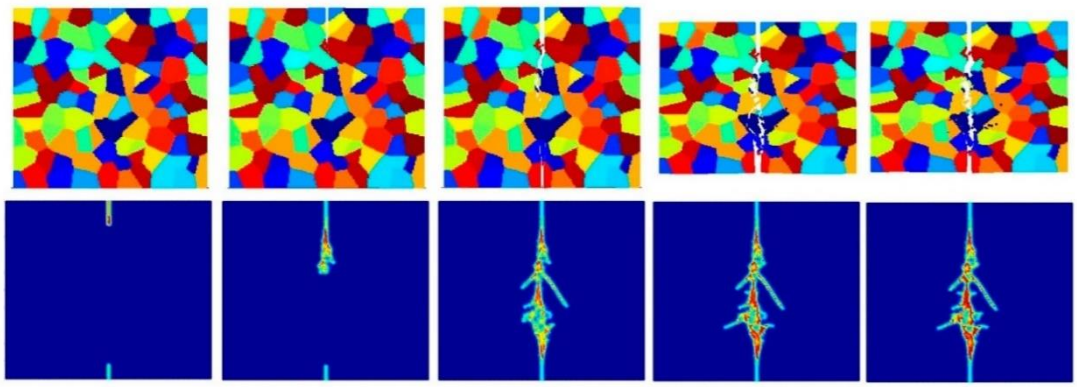

Figure 39. Fracture pattern of polycrystal when $\beta = 1.0$ with 100 grains in total. From left to right: time = 1.5 μs, 2.0 μs, 2.5 μs, 3.0 μs, and 3.5 μs *, respectively*

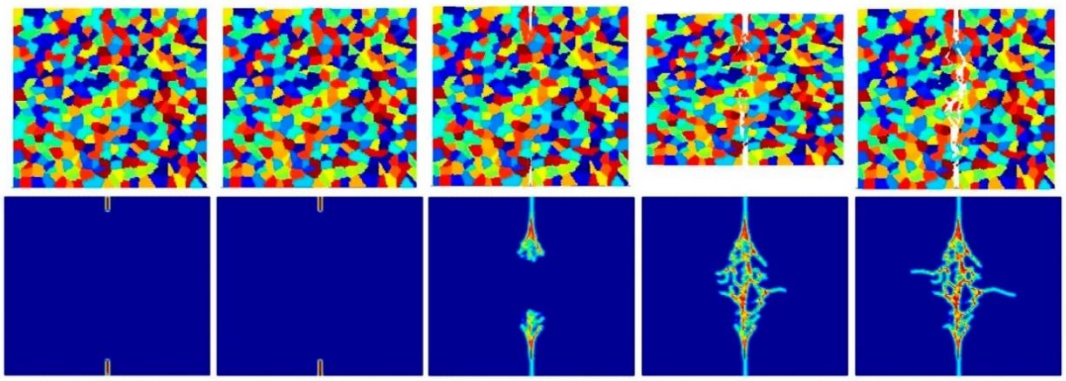

Figure 40. Fracture pattern of polycrystal when $\beta = 1.0$ *with 400 grains in total. From left to right:* time = 1.5 μs, 2.0 μs, 2.5 μs, 3.0 μs, and 3.5 μs *, respectively*

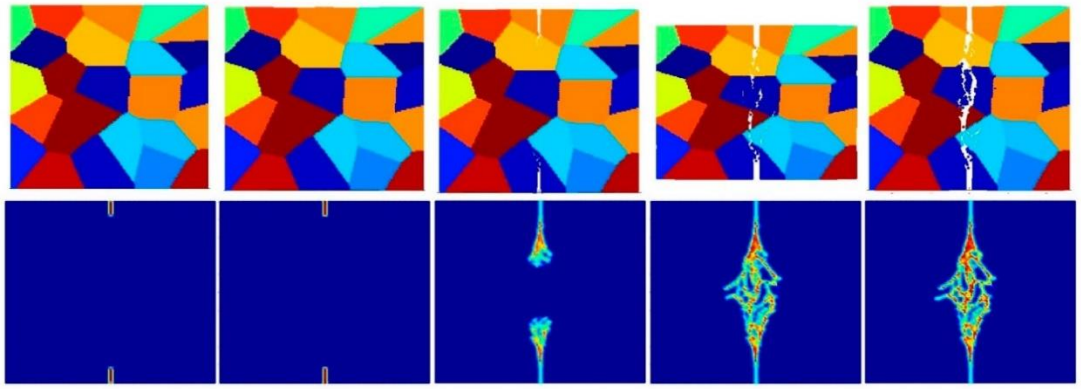

Figure 41. Fracture pattern of polycrystal when $\beta = 2.0$ *with 25 grains in total. From left to right:* time = 1.5 μs, 2.0 μs, 2.5 μs, 3.0 μs, and 3.5 μs *, respectively*

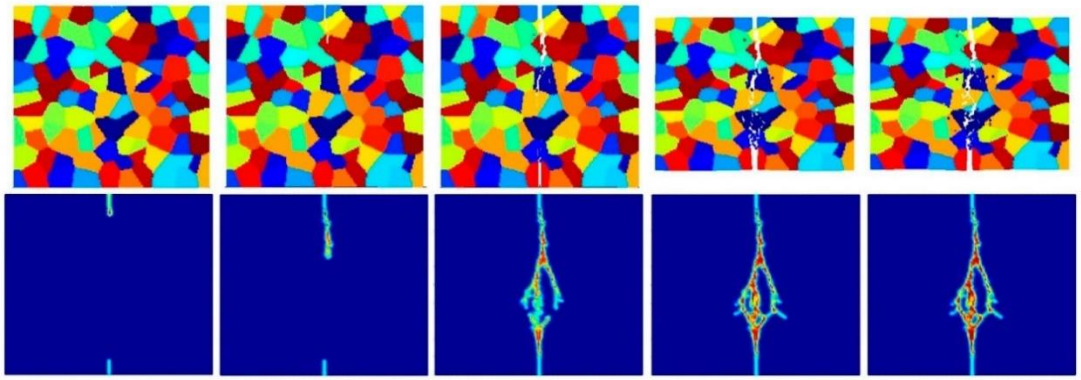

Figure 42. Fracture pattern of polycrystal when $\beta = 2.0$ *with 100 grains in total. From left to right:* time = 1.5 μs, 2.0 μs, 2.5 μs, 3.0 μs, and 3.5 μs *, respectively*

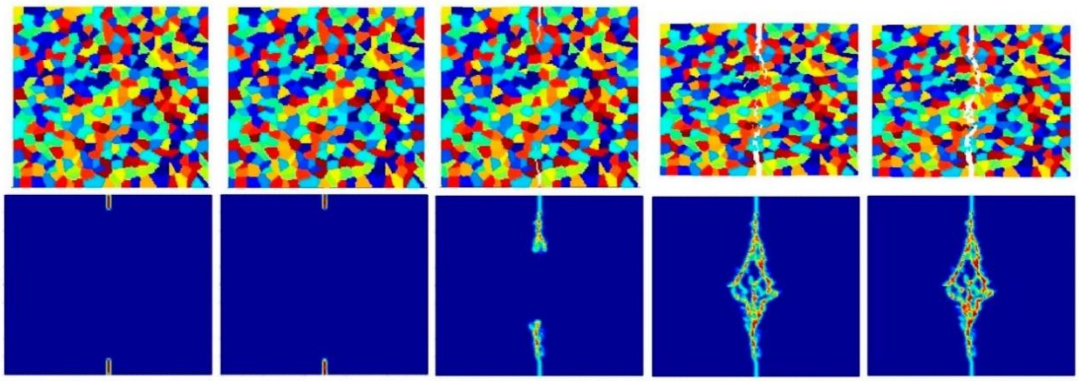

Figure 43. Fracture pattern of polycrystal when $\beta = 2.0$ *with 400 grains in total. From left to right:* time = 1.5 μs, 2.0 μs, 2.5 μs, 3.0 μs, and 3.5 μs *, respectively*

3.5. Summary

In this chapter, a new OSB PD formulation is presented, and related derivations are provided. The current model does not have any limitations on material constants as in the BB PD theory. Static analyses were carried out for validation purposes and a comparison of results between PD and FEM shows that the proposed PD model can accurately capture the deformation behaviour of cubic polycrystalline materials. Then, dynamic analyses were carried out by considering different configurations to investigate the effect of interface strength coefficient, discretization size, and crystal size. The observations based on the evaluated results can be summarized as:

1. Intergranular and transgranular fracture modes can be captured by changing the interface strength coefficient. As a future study, by comparing the experimental and PD results of crack morphology, actual interface strength coefficients can be estimated. Once the interface strength coefficient is estimated for a certain material, it could be used as a material parameter for researchers to study more complex problems and make the analysis easier.
2. The accuracy of simulation can be improved by increasing the total number of particles for intergranular fracture. However, the difference is not

significant for transgranular fracture. In order to prevent the simulation from being time-consuming, a good balance should be considered between accuracy and simulation time.

3. Pre-existing cracks can propagate more easily with decreasing crystal size for intergranular fracture mode, since there is a higher probability of a pre-existing crack interacting with a grain boundary.

As a future study, experimental studies can be used to validate and refine the damage predictions of the proposed PD model, which is also the reason why the dynamic results were not able to be verified. Moreover, as the current study is mainly focused on a 2D model, the formulation can be extended to a 3D model.

4. CALCULATION OF STRESS INTENSITY FACTOR

4.1. Introduction

This chapter will introduce a new approach to calculate stress intensity factors based on a combination of DEM and PD Theory. After obtaining the displacement field from PD Theory, by appropriately selecting nodes at the crack tip region and their displacements yield SIF at the crack tips. To demonstrate the capability of the proposed approach, three different benchmark problems are considered including plate with a central crack, plate with an edge crack and plate with a slanted crack. Results evaluated from the current approach are compared against analytical and finite element analysis results, and good agreement is obtained between three different approaches. This shows that coupled DEM and PD Theory approach can be an alternative method to calculate SIF.

4.2. Displacement Extrapolation Method

The displacement field around crack tip under Mode I loading condition (Figure 45a) for linear elastic materials can be written as:

$$u = \frac{K_I}{G}\sqrt{\frac{r}{2\pi}}\cos\frac{\theta}{2}\left[\frac{\lambda-1}{2}+\sin^2\frac{\theta}{2}\right] \tag{73}$$

$$v = \frac{K_I}{G}\sqrt{\frac{r}{2\pi}}\sin\frac{\theta}{2}\left[\frac{\lambda+1}{2}-\cos^2\frac{\theta}{2}\right] \tag{74}$$

Where

$$\lambda = \begin{cases} 3-4\upsilon & \text{plane strain} \\ \dfrac{3-\upsilon}{1+\upsilon} & \text{plane stress} \end{cases} \tag{75}$$

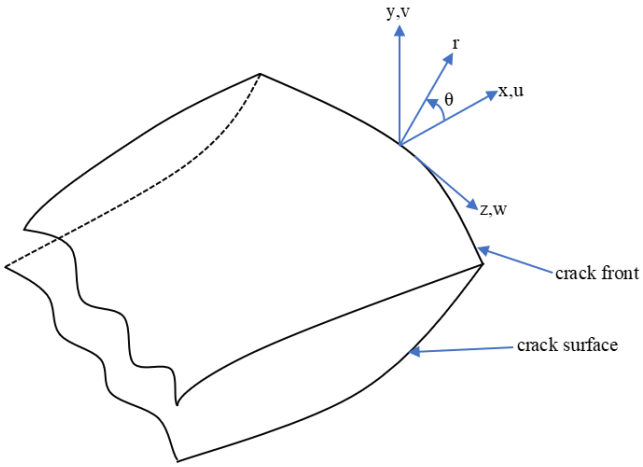

Figure 44. Local Coordinate System around Crack Tip

As shown in Figure 44, u and v are displacements in the local Cartesian coordinate system, r and θ are the coordinates in the local cylindrical coordinate system at crack tip, G and υ are shear modulus and Poisson's ratio of the material, and K_I is the SIF under Mode I loading condition.

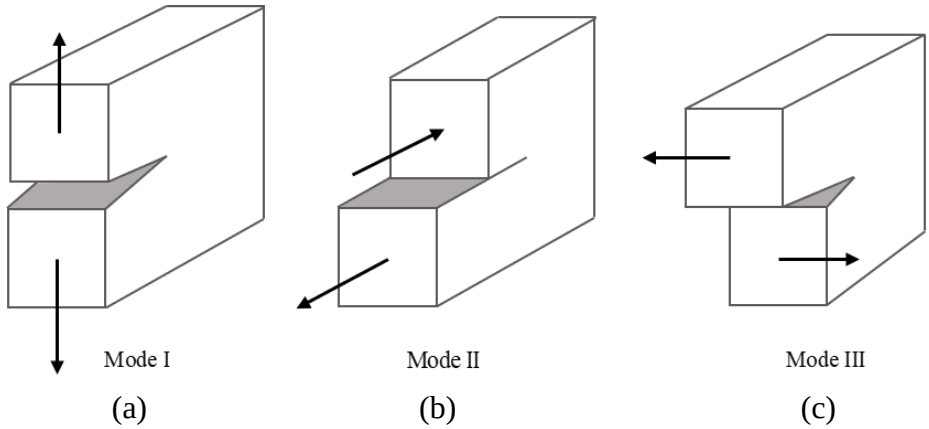

Figure 45. Fracture modes: (a) Mode I – crack opening, (b) Mode II – in-plane shear and (c) Mode III – out-of-plane shear

On the other hand, the displacement expressions for a crack tip under Mode II loading condition (Figure 45b) can be expressed as:

$$u = \frac{K_{II}}{G}\sqrt{\frac{r}{2\pi}}\sin\frac{\theta}{2}\left[\frac{\lambda+1}{2}+\cos^2\frac{\theta}{2}\right] \tag{76}$$

$$v = \frac{K_{II}}{G}\sqrt{\frac{r}{2\pi}}\cos\frac{\theta}{2}\left[\frac{\lambda-1}{2}+\sin^2\frac{\theta}{2}\right] \tag{77}$$

where K_{II} is the Mode II SIF. Moreover, the displacement expression for a crack tip under Mode III loading (Figure 45c) can be expressed as:

$$w = \frac{K_{III}}{G}\sqrt{\frac{2r}{\pi}}\sin\frac{\theta}{2} \tag{78}$$

where K_{III} is the Mode III SIF. Hence, the actual displacements around the crack tip area for linear elastic materials under mixed-mode loading can be expressed as:

$$u = \frac{1}{4G}\sqrt{\frac{r}{2\pi}}\left\{K_I\left[(2\lambda-1)\cos\frac{\theta}{2}-\cos\frac{3\theta}{2}\right]-K_{II}\left[(2\lambda+3)\sin\frac{\theta}{2}+\sin\frac{3\theta}{2}\right]\right\} \tag{79}$$

$$v = \frac{1}{4G}\sqrt{\frac{r}{2\pi}}\left\{K_I\left[(2\lambda-1)\sin\frac{\theta}{2}-\sin\frac{3\theta}{2}\right]-K_{II}\left[(2\lambda+3)\cos\frac{\theta}{2}+\cos\frac{3\theta}{2}\right]\right\} \tag{80}$$

$$w = \frac{2K_{III}}{G}\sqrt{\frac{r}{2\pi}}\sin\frac{\theta}{2} \tag{81}$$

where

$$\lambda = \begin{cases} 3-4\upsilon & \text{plane strain} \\ \dfrac{3-\upsilon}{1+\upsilon} & \text{plane stress} \end{cases} \tag{82}$$

For material points located at crack surface $\left(\theta = 180^\circ\right)$, Equations (79), (80) and (81) can be rewritten as:

$$u = \frac{K_{II}}{2G}\sqrt{\frac{r}{2\pi}}(1+\lambda) \tag{83}$$

$$v = \frac{K_{I}}{2G}\sqrt{\frac{r}{2\pi}}(1+\lambda) \tag{84}$$

$$w = \frac{2K_{III}}{G}\sqrt{\frac{r}{2\pi}} \tag{85}$$

Therefore, the Mode I, Mode II and Mode III SIF for material points which are located at crack surface can be calculated through the displacements as:

$$K_{I} = \sqrt{2\pi}\,\frac{G}{1+\lambda}\,\frac{|\Delta v|}{\sqrt{r}} \tag{86}$$

$$K_{II} = \sqrt{2\pi}\,\frac{G}{1+\lambda}\,\frac{|\Delta u|}{\sqrt{r}} \tag{87}$$

$$K_{III} = \sqrt{2\pi}\,\frac{G}{1+\lambda}\,\frac{|\Delta w|}{\sqrt{r}} \tag{88}$$

where Δv, Δu and Δw are the relative displacements of one crack face with respect to the other. For example, $|\Delta v| = |v_K - v_M|$ for points K and M shown in Figure 46(a).

As shown in Figure 46(a), in order to find the SIF at the crack tip $(r = 0)$, the only term that needs to be considered is $\frac{|\Delta v|}{r}$ for the full crack model. Note that for symmetric problems with respect to the horizontal plane, it is sufficient to consider half of the model as shown in Figure 46(b) and the relative displacement can be

calculated as $\Delta v = 2 \cdot \Delta v'$. It can be assumed that $\frac{|\Delta v|}{r}$ is a linear function for the material points at the crack surface:

$$\frac{|\Delta v|}{\sqrt{r}} = a + b \cdot r \tag{89}$$

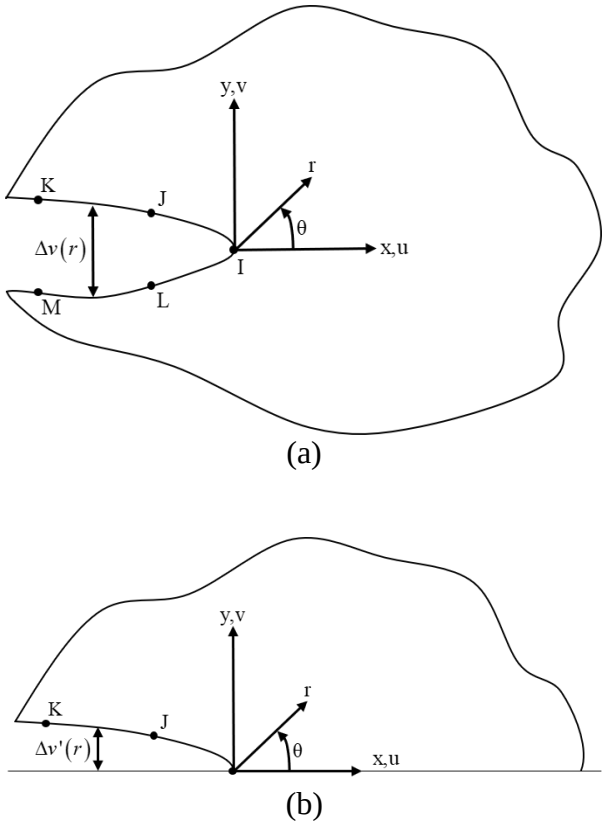

Figure 46. Crack tip displacements: (a) Full model, (b) Half model

Unknown constant a and b can be determined with the displacements of the selected material points (point K, J, M and L in Figure 46). To calculate K_I at the crack tip, $r \to 0$, Equation (89) will yield as:

$$\lim_{r \to 0} \frac{|\Delta v|}{\sqrt{r}} = a \tag{90}$$

Therefore, the SIF K_I can be computed as:

$$K_I = \sqrt{2\pi}\,\frac{Ga}{1+\lambda} \tag{91}$$

4.3. Implementation of DEM in PD

As described in previous section, it is essential to find the proper material points (including one for the crack tip location and the other two for symmetric problems or four for other problems) to compute the stress intensity factor using DEM. The numerical implementation is done by implementing the PD formulation in finite element framework as described in (Macek and Silling, 2007). The static solution is obtained by directly assigning zero to the inertia term and solving a matrix system. After the displacement field is obtained (as shown in Figure 47) and proper material points are selected (for example, point 41 and 42 in Figure 48), the Mode I stress intensity factor K_I can be calculated using Equation (91) with the displacements v of the selected material points. The flowchart of the process can be found in Figure 49. In the current study, the material points which not only closest to the crack tip, but also closest to the actual crack surface are chosen to calculated SIF.

4.4. Numerical Results

To verify the implementation of DEM in PD framework, several benchmark problems, starting from the simple central-cracked problem to the more complex slanted-cracked problem, were considered, and the results were compared with both analytical solutions and those computed by ANSYS.

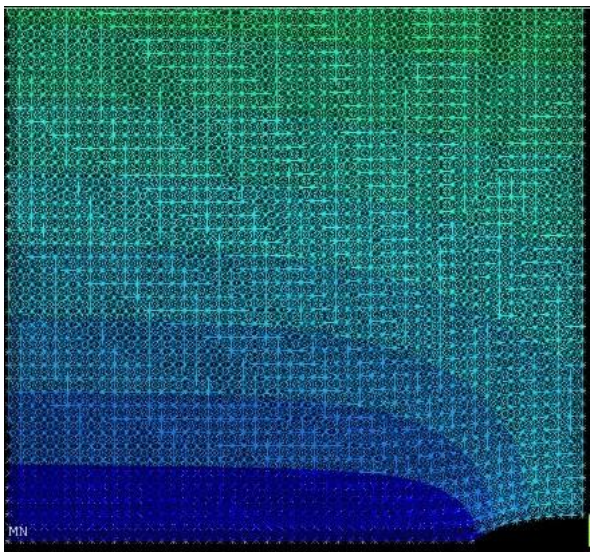

Figure 47. Displacement Field around Crack Tip Area

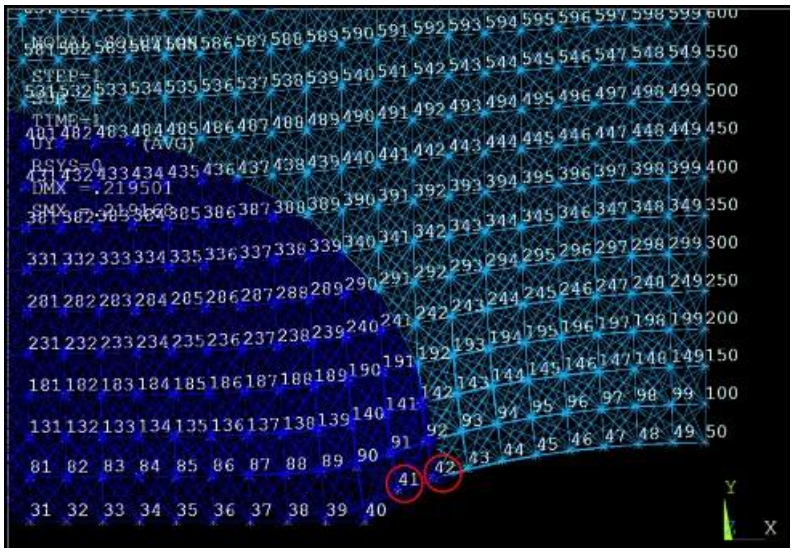

Figure 48. Example of Points Selection to Calculate SIF

4.4.1. Plate with a central crack

The first problem that was considered was a finite width plate with a crack at the centre. As shown in Figure 50, the width and height of the plate were $(2b=)$ 2m and $(2h=)$ 4m, respectively, and a $(2a=)$ 0.4m long crack was located at the centre of the plate. The elastic modulus was specified as 164.3 GPa and Poisson's ratio is 0.32. A tension load of 183 MPa was applied on both top and bottom edges of the plate.

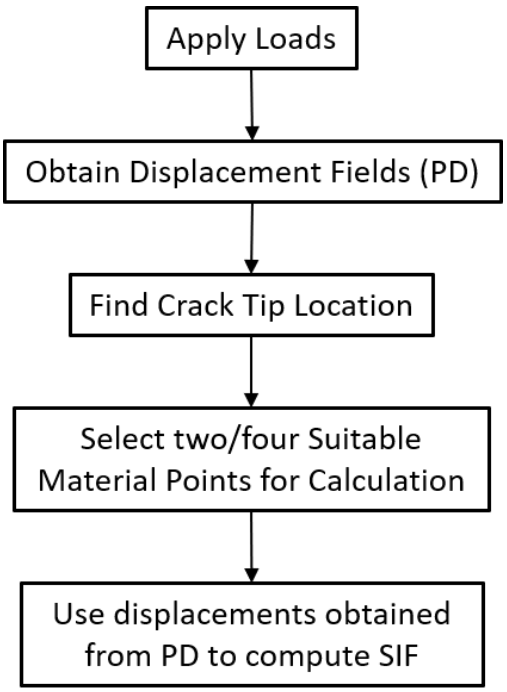

Figure 49. Flowchart for Calculation of SIF

For this particular configuration, (Rooke and Cartwright, 1976) provided a theoretical equation on how to compute the Mode-I SIF for the plate with a central crack, which can be written as:

$$K_I = \sigma\sqrt{\pi a}\left[\frac{1-\frac{a}{2b}+0.326\left(\frac{a}{b}\right)^2}{\sqrt{1-\frac{a}{b}}}\right] \tag{92}$$

For the PD simulation, the plate was discretised by 100×200 material points, and the thickness of the plate was specified as 0.02m. The normalised SIF calculated from PD was compared with the result computed from Equation (92) and the result calculated from ANSYS, a commercial finite element software, by using the KCALC command. Table 2 shows results and the comparison between PD, analytical and ANSYS results. According to these results, SIF calculated from PD theory agree very well with the analytical and ANSYS results. The difference between PD and

analytical results is less than 5% whereas the difference between PD and ANSYS results is less than 3%.

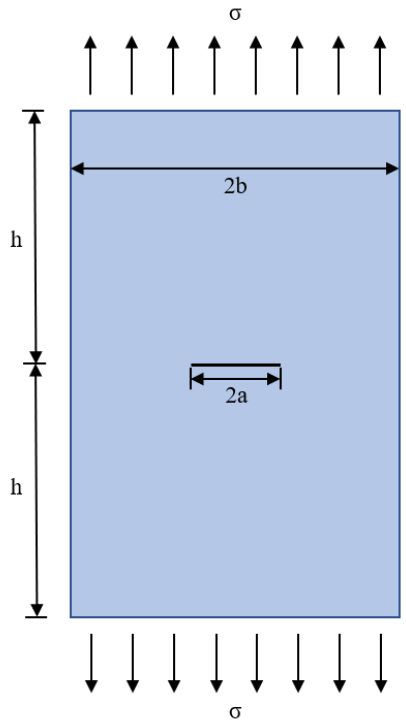

Figure 50. Finite Plate with a Central Crack

Table 2. Summary of SIF results (plate with a central crack)

	Mode I normalised SIF ($K_I / \sigma\sqrt{\pi a}$)	Difference
PD	1.0541	
Equation (92)	1.0050	4.87%
ANSYS	1.0265	2.69%

4.4.2. Plate with an edge crack

The second problem which was considered was a plate with an edge crack, as shown in Figure 51, the width and height of the plate were $(b=)$ 1m and $(2h=)$ 4m, respectively, and a $(a=)$ 0.2m long crack was located at the left edge of the plate. The material properties and the tension load are the same as in the first problem.

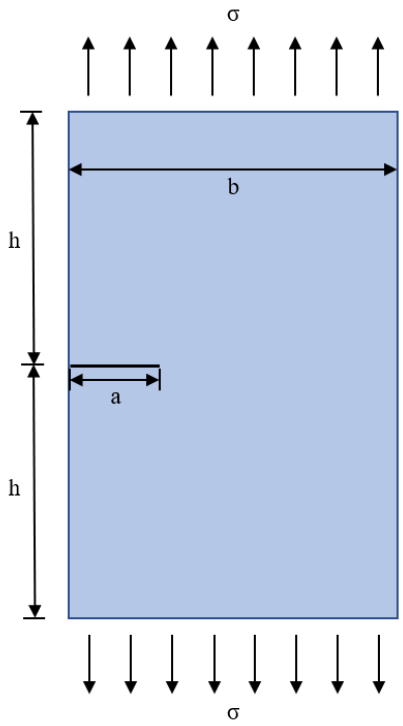

Figure 51. Plate with an edge crack

For this particular configuration, the SIF can be calculated as:

$$K_I = 1.12\sigma\sqrt{\pi a} \tag{93}$$

The plate was also discretized by 100×200 material points and the PD SIF result was compared with that computed by Equation (93) given by (Paul C. Paris and Sih, 1965) and ANSYS, which can be shown in Table 3. Again, a good agreement is obtained between PD, analytical and ANSYS results. The difference between PD and analytical results is less than 4% whereas the difference between PD and ANSYS results is less than 5%.

Table 3. Summary of SIF results (plate with an edge crack)

	Mode I normalized SIF ($K_I / \sigma\sqrt{\pi a}$)	Difference
PD	1.1637	
Equation (93)	1.1200	3.88%
ANSYS	1.1133	4.52%

4.4.3. Plate with a slanted crack

The third problem which was considered was a plate with a slanted crack at the centre. As shown in Figure 52, β is the orientation of the crack surface with respect to x-axis. The width and height of the plate were $(b=)$ 1m and $(h=)$ 2m, respectively, and the central crack has a length of $(a=)$ 0.2m.

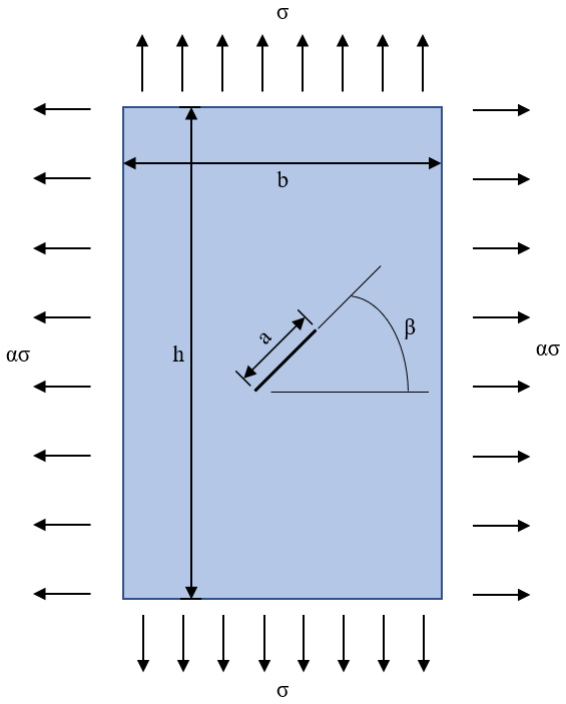

Figure 52. Plate with a slanted crack

The analytical form of SIF for slanted cracks can be expressed as (George C. Sih, Paris and Erdogan, 1962):

$$K_I = \sigma\sqrt{\frac{\pi a}{2}}\left(\cos^2\beta + \alpha\sin^2\beta\right) \tag{94}$$

and

$$K_{II} = \sigma\sqrt{\frac{\pi a}{2}}(1-\alpha)\sin\beta\cos\beta \tag{95}$$

where α is the ratio between the tensile load applied horizontally and the load applied vertically. In this section, α was set to 0, which means only tension loading is applied at the top and bottom edges of the plate, and β was set to be 60 and 15 degree. The material properties and the tension load are the same as in the previous problem.

Unlike the PD simulation described in the previous two sections, in order to make the analysis more accurate due to the crack is not aligned with horizontal axis, the plate was discretized into 160×320 material, and the results of both Mode I and Mode II SIFs were computed from PD and compared with SIF calculated by using Equations (94) and (95). The results are given in Table 3, Table 4 and Table 5.

As shown in the tables, a very good agreement is obtained for both Mode I and Mode II SIFs between analytical and PD results. The difference between PD and analytical results is less than 8% for both Mode-I and Mode-II SIFs.

Table 4. Summary of SIF results (plate with 60 degree slanted crack)

β=60°	Mode I normalized SIF ($K_I / \sigma\sqrt{\pi a}$)	Difference
PD	0.2702	
Equation (26)	0.2506	7.82%
	Mode II normalized SIF ($K_{II} / \sigma\sqrt{\pi a}$)	Difference
PD	0.4600	
Equation (27)	0.4329	6.26%

Table 5. Summary of SIF results (plate with a 15 degree slanted crack)

β=15°	Mode I normalized SIF ($K_I / \sigma\sqrt{\pi a}$)	Difference
PD	1.0022	
Equation (26)	0.9332	7.40%
	Mode II normalized SIF ($K_{II} / \sigma\sqrt{\pi a}$)	Difference
PD	0.2632	
Equation (27)	0.2501	5.26%

4.5. Summary

In this chapter, a coupled DEM and PD Theory approach is utilized to calculate SIF. To demonstrate the capability of the proposed approach, three different benchmark problems were considered including plate with a central crack, plate with an edge crack and plate with a slanted crack. SIF obtained from PD Theory were compared against analytical and ANSYS results. For all three cases, it was observed that the results obtained with the current approach agree well with analytical and ANSYS results. The maximum difference between PD and analytical results is less than 8% for all cases including Mode-I and Mode-II SIFs. Finally, it can be concluded that the proposed approach can be used as an alternative approach to calculate SIF. Although DEM has been widely used in FEM to calculate SIF already, there are few researchers who use DEM under PD framework. Unlike the J-integral which need a specific path to calculate SIF, DEM can directly link the displacement field solved by PD theory with DEM without any modification. As discussed in Abstract, PD has many advantages compare with other numerical methods when dealing with discontinuity problems. For example, the remeshing is the main problem when using FEM to simulate crack growth, but PD can handle it automatically. Since PD has been chosen as the tool to solve polycrystal fatigue crack growth problem, it is

necessary to discover a method to calculate SIF under PD framework, rather than under FEM framework.

5. FATIGUE MODEL IN PERIDYNAMIC FRAMEWORK

5.1. Introduction

This chapter provides simulations to predict crack propagation of polycrystal structure under cyclic loads using PD theory. The PD fatigue model utilizes the ε-N data and introduces the "bond remaining life" of each bond calculated from its cyclic strain which changes over time. The model also captured the traditional Paris' law which is widely used for computing fatigue crack growth. Moreover, a crack tip detecting algorithm is introduced in this chapter to face the requirements of the fatigue model. Finally, several simulations are carried out to compare the effect of how the strength of crystal boundary influences the crack pattern.

5.2. Fatigue Model in Peridynamic Framework

The PD fatigue model was recently introduced by (Stewart A. Silling and Askari, 2014) for linear isotropic materials, which includes all three phases in fatigue failure: nucleation, crack growth and static propagation.

Unlike the failure algorithm described in Chapter 2.3, which was used for analysis of linear elastic brittle material, a new algorithm called "remaining life" was introduced. The new damage variable $\lambda(\mathbf{x},\boldsymbol{\xi},N)$ means the remaining life of a bond $\boldsymbol{\xi}$ which is associated with the material point $\mathbf{x}$, and can be expressed as follows (Stewart A. Silling and Askari, 2014):

$$\frac{d\lambda}{dN}(N) = -A\varepsilon^{m} \tag{96}$$

where A and m are material constants which can be determined by complying against experimental results. ε denotes the cyclic bond strain of the bond ξ, which can be computed using the equation below:

$$\varepsilon = \left| s^{\max} - s^{\min} \right| \tag{97}$$

where $s^{\max}$ and $s^{\min}$ are the stretch of the bond ξ under the two extreme loads in this cycle. It is assumed that the initial life of the bond ξ at $N = 0$ is 1, i.e. $\lambda(0) = 1$, and the bond breaks irreversibly when $\lambda(N) \le 0$. Since the material is assumed to be linear elastic material, the cyclic bond strain can also be expressed by using only $s^{\max}$ and the load ratio $R = s^{\min} / s^{\max}$. Hence Equation (97) can be rewritten as:

$$\varepsilon = \left| (1 - R) s^{\max} \right| \tag{98}$$

which means that only the maximum loading condition needs to be considered in simulations.

The first phase of the PD fatigue model is Phase I: Nucleation. In this phase, the material constant A and m are calibrated with the experimental results (i.e. the S-N curve in strains) of the material, which is shown in Figure 53.

It was assumed that the first bond in the horizon $H_{\mathbf{x}}$ is broken at N_1 cycle, and the corresponding cyclic strain range is ε_1. Since the initial bond life of this bond is $\lambda_1(0) = 1$, by integrating Equation (96), it can lead to:

$$A_1 \varepsilon_1^{m_1} N_1 = 1 \tag{99}$$

where A_1 and m_1 denotes the material constants for Phase I analysis. To obtain A_1 and m_1, a straight line is fitted to the experimental data in the form of an S-N curve in terms of strains, and the constants can be obtained from the function of the fitted straight line. Hence the first bond is broken when:

$$N \geq \frac{1}{A_1 \varepsilon_1^{m_1}} \tag{100}$$

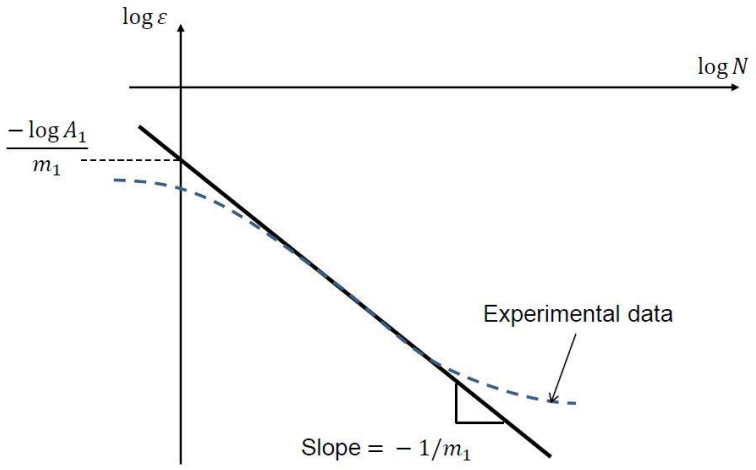

Figure 53. Calibration of Material Constant for Phase I: Nucleation

If there is a bond broken at ε_1 in Phase I, new static analysis needs to be carried out at the same cycle. Since the strains of nearby bonds will increase, if the strain of a nearby bond is larger than ε_1, the bond is broken and another static solution is calculated until there are no more bonds broken.

The second phase of the PD fatigue model is Phase II: crack growth. Unlike Phase I, in which Equation (96) is used to evaluate the fatigue life of a bond, the discretized remaining life λ_{ij}^n which is associated with the material points $\mathbf{x}_i$ and $\mathbf{x}_j$ for a range

of discretized range of cycles $N(n)$ can be evaluated using backward finite differences of Equation (96) as follows (Guanfeng Zhang *et al.*, 2016):

$$\frac{\lambda_{ij}^{n}-\lambda_{ij}^{n-1}}{N(n)-N(n-1)}=-A_2\left(\varepsilon_{ij}^{n}\right)^{m_2} \tag{101}$$

with

$$\lambda_{ij}^{0}=1 \tag{102}$$

where ε_{ij}^{n} represents the cyclic bond strain of bond ξ_{ij} at cycle range n, and A_2 and m_2 are material constants for Phase II analysis. In order to determine these two material constants, the PD remaining life evolution law needs to be calibrated with the well-known Paris' Law (Stewart A. Silling and Askari, 2014), whose data can be obtained from experiments. It is assumed that the evolution law for the remaining life is only suitable to use for the bonds which are located in the horizon of points that are in Phase II or at the crack-tip. The explanation of how to obtain A_2 and m_2 can be found in (Stewart A. Silling and Askari, 2014) and (Guanfeng Zhang *et al.*, 2016).

The transformation of PD fatigue analysis from Phase I: Nucleation to Phase II: Crack Growth happens when there's a point that within its horizon (including itself), there is a point with a damage value of $d \geq 0.5$. If there is a pre-existing crack presented in the model, the points located within the horizon of the crack tip will directly switch to Phase II, as there are points whose damage values have already reached to 0.5.

5.3. Crack Tip Detecting Algorithm

As described in the previous section, the points which are located within the horizon of the crack tip will directly switch from Phase I to Phase II if a pre-existing crack is presented in the model, hence it is essential to automatically update the location of the crack tip during the simulation. “bwmorph” function with “endpoints” option has been used by (Guanfeng Zhang *et al.*, 2016) after converting the PD damage map to black and white images in Matlab. There are different crack tip detecting (or tracking) algorithms been developed in CZM and FEM (M. Cervera and Chiumenti, 2006, Saloustros, Pelà and Cervera, 2015, Sancho *et al.*, 2007, Wang and Xu, 2015), however, quite less in PD theory. The crack tip detecting algorithm used in this thesis is generally following the similar technique introduced in (Miguel Cervera *et al.*, 2010). There are three steps when using crack tip detecting algorithm in PD framework: Firstly, a mesh is generated using PD bonds to connect a material point with its neighbouring material points only. In other words, there are no bonds exceeding length of Δx in this mesh. Therefore, the model is discretised in to unit blocks which contain four material points and four bonds with a length of Δx in each block. Secondly, the four bonds in a block are checked every PD integration to see if any of which are broken. If at least one bond breaks, the status of this block will be marked as “damaged” (shown as “T” in Figure 54). A “damaged” block means the crack tip has already either reached or passed this block. Thirdly, for each “damaged” block, its neighbouring blocks need to be checked to see how many of these blocks are “damaged”. Hence, the crack tip will be located at the damaged block which has only one damaged neighbouring block.

5.4. Numerical Results and Discussion

5.4.1. Analysis of plate with a central crack problem using crack tip detecting algorithm

Before starting to use PD fatigue model to analyse a polycrystalline material, crack tip detecting algorithm needs to be tested by simulating the same problem presented in (Madenci and Oterkus, 2014).

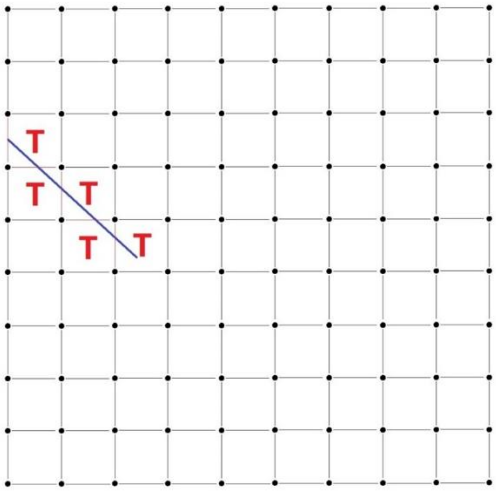

Figure 54. PD mesh used in the crack tip detecting algorithm, blue line represents the pre-existing crack

The first problem is a 0.05 m width and 0.0001 m thick square plate with a 0.01 m length pre-existing central crack. The plate is discretised with 500×500 material points. Moreover, 3 more layers of material points are added on both top and bottom edges (as shown in Figure 55) in order to apply 20.0 m/s velocity boundary condition to these edges. The horizon δ is set as 3.015 times the spacing between material points and the critical stretch is $s_0 = 0.04472$. There are 1250 time steps in the simulation, and the time step size is $\Delta t = 1.3367 \times 10^{-8}$s.

In (Madenci and Oterkus, 2014), local damage value was used to determine the location of the crack tip, which was based on any material point's damage exceeding

$d = 0.38$ along the x-axis. The growth of the crack with respect of time is shown in Figure 56 (blue line), and the crack growth speed can be obtained as 1650 m/s.

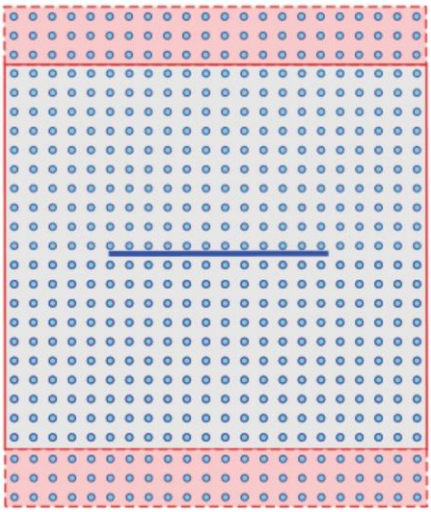

Figure 55. Plate with a pre-existing central crack

The crack growth data can also be obtained using the crack tip detecting algorithm when running the same problem, which is shown in Figure 56 (red line), and the crack growth speed can be obtained from the slope of the straight line as 1641 m/s. By comparing the results with those in (Madenci and Oterkus, 2014), it can be concluded that the results are in good fit.

5.4.2. Fatigue analysis of polycrystalline material

The PD fatigue analysis is generally following the flowchart given in Figure 57 where $D_{\min}$ and $D_{\max}$ represents the critical damage factors, which were introduced by (Guanfeng Zhang *et al.*, 2016). The purposes of introducing these two parameters are not only to determine the correct crack path with minimal number of static solutions, but also to prevent from breaking too many bonds within one static solution so that the solution doesn't become unstable. In each static solution, the maximum damage difference (Δd) of material points which are located within a

certain area from the crack tip between the previous static solution and the current one is compared with the two critical damage factors to determine the next action by following the flowchart. The location of the crack tip is updated for each static solution as well in order to determine the material points that are in crack growth stage.

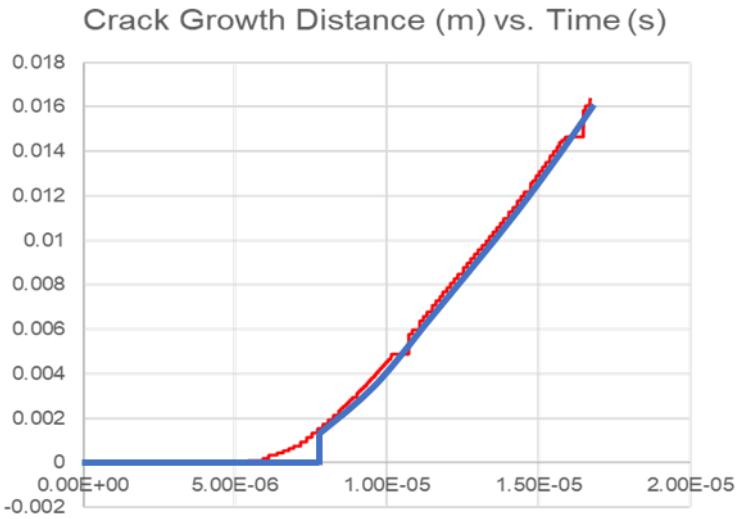

Figure 56. Crack growth vs. Time (Red – Crack tip detecting algorithm, Blue - (Madenci and Oterkus, 2014))

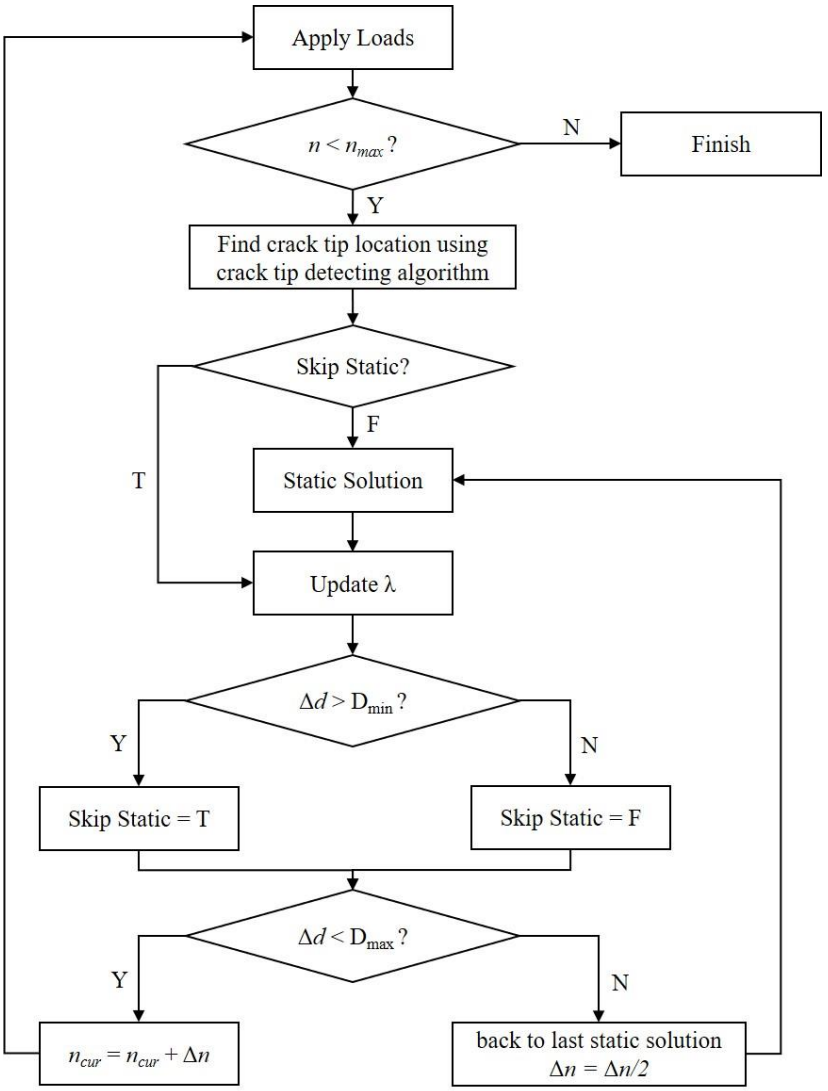

Figure 57. Flowchart for PD fatigue analysis with critical damage factors

5.4.3. Setup of the model

The geometry of the model can be found in Figure 58. The material used in the analysis was the cold rolled SAE 1020 steel, with Young's modulus of E = 205 GPa and Poisson's ratio of 0.29. According to (Guanfeng Zhang *et al.*, 2016), since there is a pre-existing crack in the model, the whole simulation will automatically switch to the crack growth phase, hence the key parameters that were used in the analysis

are A_2=9.53×10^6 and $m_2 = 2.1$. The horizon size is $\delta = 1.2$ mm, and $\delta / \Delta x = 4$. The force which is exerted on the model is P=6000N.

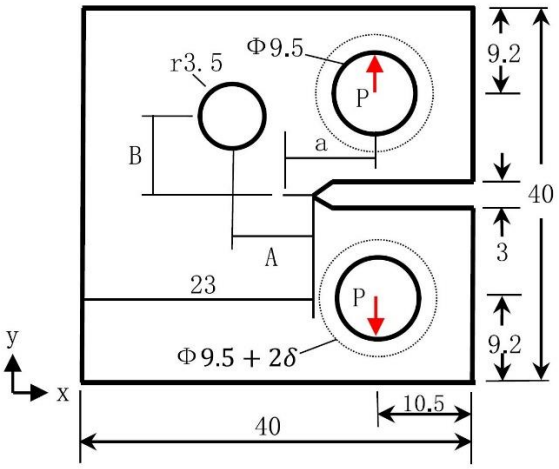

Figure 58. Geometry of the model used in PD fatigue analysis

There were three different polycrystalline models considered, with 25, 100 and 400 grains randomly distributed within the model, respectively. The polycrystal models were generated using Voronoi diagram, which are shown in Figure 59, and to make the simulation simple, the material in each grain is assumed to be isotropic. To investigate various fracture modes of polycrystalline materials, the "interface strength coefficient (β)" was first introduced by (Askari *et al.*, 2008) and then discussed by (De Meo, Zhu and Oterkus, 2016) and (Ning Zhu, De Meo and Oterkus, 2016). Similarly, the interface strength coefficient was also considered in this paper to study the effect of interface strength with respect to the crack pattern. Unlike β described in (Askari *et al.*, 2008), β used in this chapter can be defined as:

$$\beta = \frac{A_2^{GI}}{A_2^{GB}} \tag{103}$$

where A_2^{GB} and A_2^{GI} denote the material constants used in the Phase II PD fatigue analysis for the bonds that cross the grain boundary and the bonds that are located within the grain, respectively. Here, GB means the grain boundary, and GI means the grain interior. Therefore, when $\beta < 1.0$, A_2^{GB} is larger than A_2^{GI}, which means that the remaining life of the cross-grain bonds will decrease faster than the in-grain bonds, assuming the bonds are applied the same cyclic strain value. In other words, $\beta < 1.0$ means the grain boundary is weaker, on the other hand, $\beta > 1.0$ represents that the grain boundary is stronger. In this paper, the study considers 5 different interface strength coefficient, β, values (0.1, 0.5, 1.0, 2.0, 10.0) and three different total numbers of grains (25, 100 and 400).

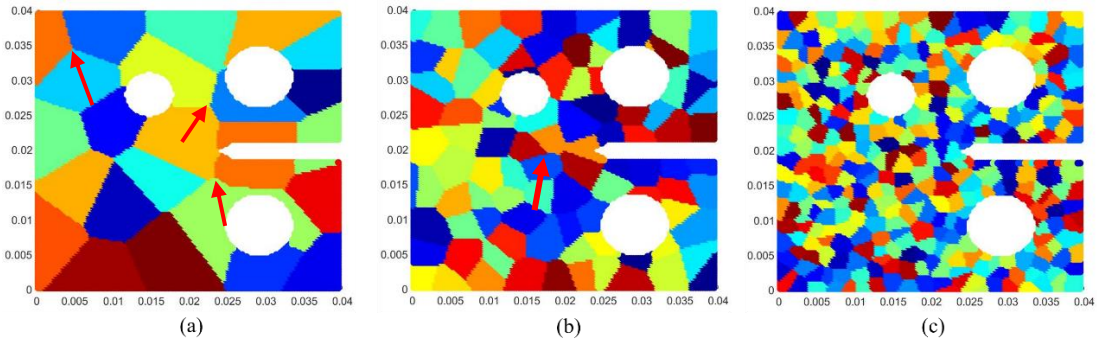

Figure 59. Polycrystal model for PD fatigue analysis. (a): 25 grains, (b): 100 grains and (c): 400 grains

5.4.4. Effect of interface strength coefficient on crack patterns

The first analysis aims to study the crack pattern of intergranular and transgranular fracture modes by changing the interface strength coefficient value.

By comparing the results in Figure 60(a) and (b) with (c), it can be found that there is a sharp turn of the crack pattern (red arrow) in both Figure 60(a) and (b), which is because that the crack was first propagating within the grain until it reached close to the grain boundary, and since the grain boundary in Figure 60(a) and Figure 60(b) is

weaker, the crack pattern is much easier to follow the boundary (intergranular fracture mode) than Figure 60(c).

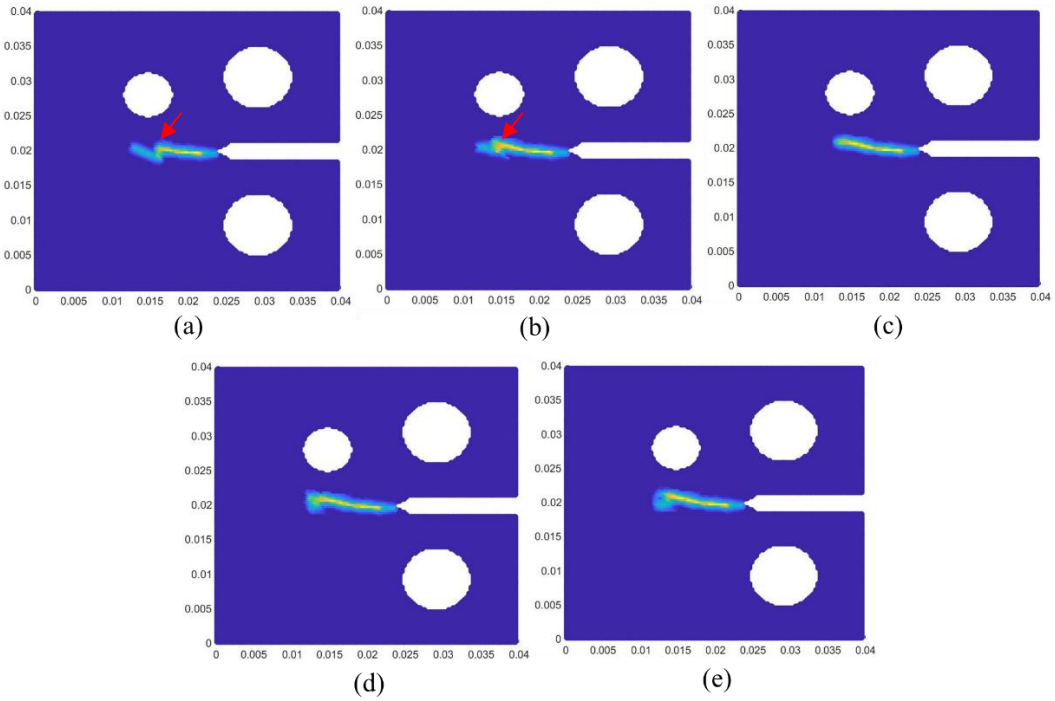

Figure 60. Crack pattern of polycrystal with 25 grains. (a) $\beta = 0.1, n = 246k$ cycles *, (b)* $\beta = 0.5, n = 331k$ cycles *, (c)* $\beta = 1.0, n = 345k$ cycles *, (d)* $\beta = 2.0, n = 431k$ cycles *, and (e)* $\beta = 10.0, n = 429k$ cycles

Figure 61 and Figure 62 both show more clearly of the influence of interface strength coefficient to the crack pattern than Figure 60. When $\beta < 1.0$ (Figure 61(a), Figure 61(b), Figure 62(a) and Figure 62(b)), which means the bonds across the grain boundary are much weaker than those located within the grain, the crack will be more likely to propagate along grain boundaries, comparing with crack patterns when $\beta > 1.0$ (Figure 61(d), Figure 61(e), Figure 62(d) and Figure 62(e)).

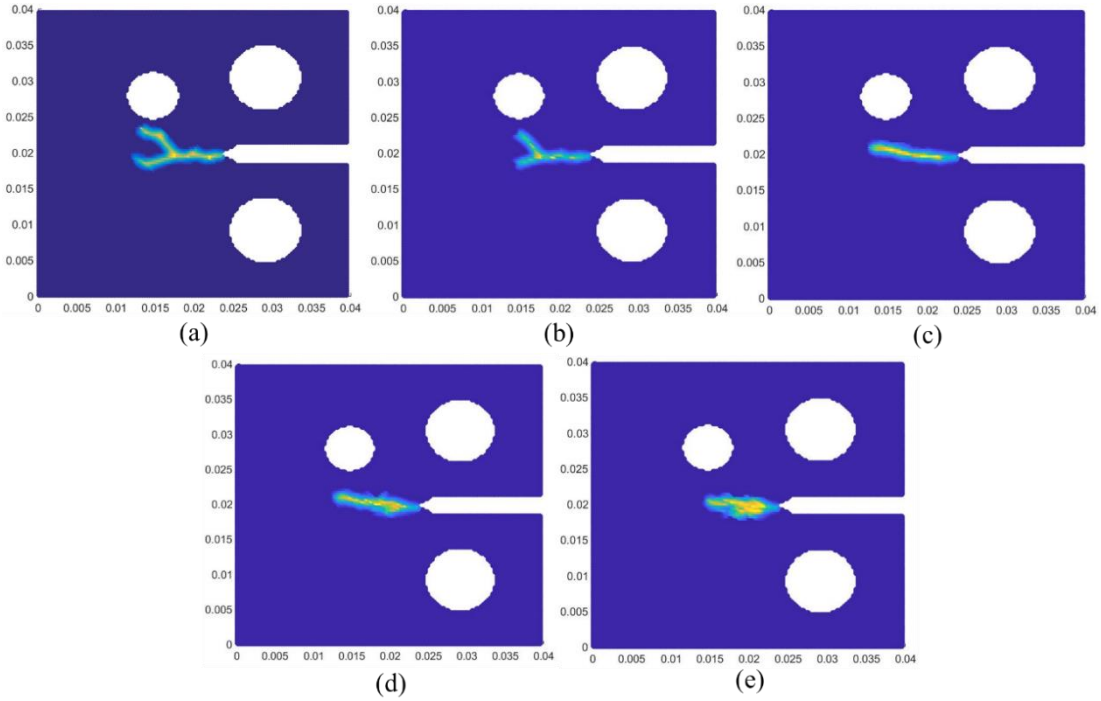

Figure 61. Crack pattern of polycrystal with 100 grains. (a) $\beta = 0.1,\ n = 48k$ cycles *, (b)* $\beta = 0.5,\ n = 174k$ cycles *, (c)* $\beta = 1.0,\ n = 345k$ cycles *, (d)* $\beta = 2.0,\ n = 453k$ cycles *, and (e)* $\beta = 10.0,\ n = 784k$ cycles

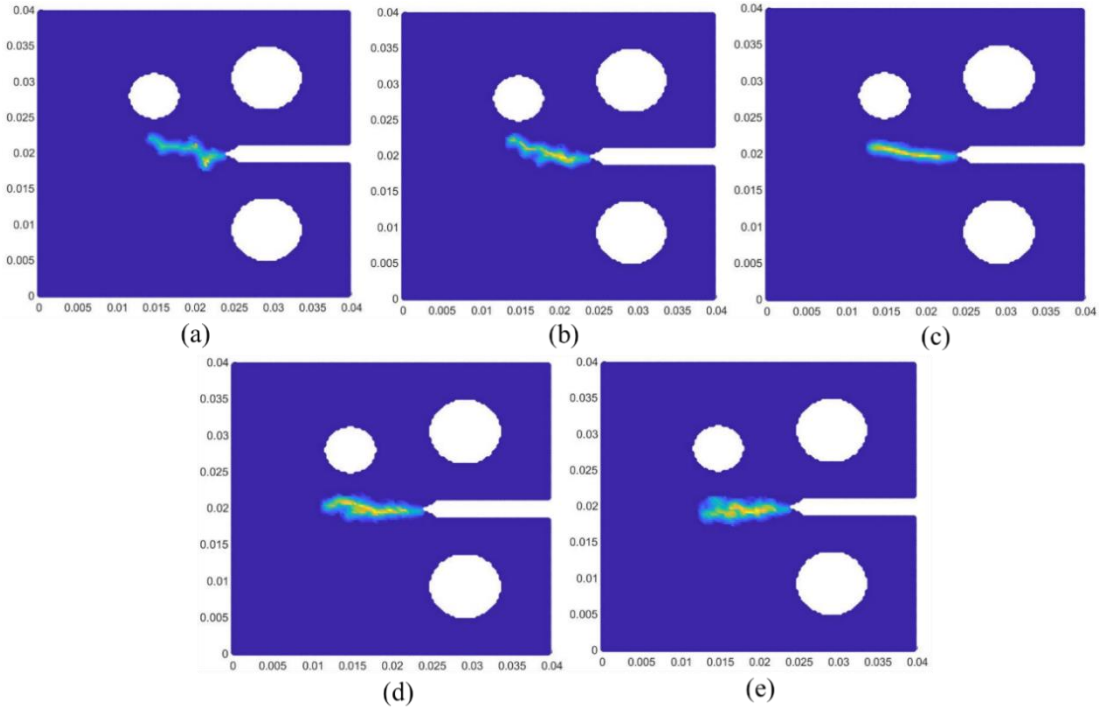

Figure 62. Crack pattern of polycrystal with 400 grains. (a) $\beta = 0.1,\ n = 51k$ cycles *, (b)* $\beta = 0.5,\ n = 214k$ cycles *, (c)* $\beta = 1.0,\ n = 345k$ cycles *, (d)* $\beta = 2.0,\ n = 512k$ cycles *, and (e)* $\beta = 10.0,\ n = 846k$ cycles

5.4.5. *Effect of crystal size on propagation speed*

The aim of the comparisons discussed in this section is to find out how the crystal size can affect the crack propagation speed. Since it was difficult to track and store the crack tip locations cycle by cycle, only total number of cycles when crack propagates to similar location ($x \cong 12.5$ mm) are compared between each case.

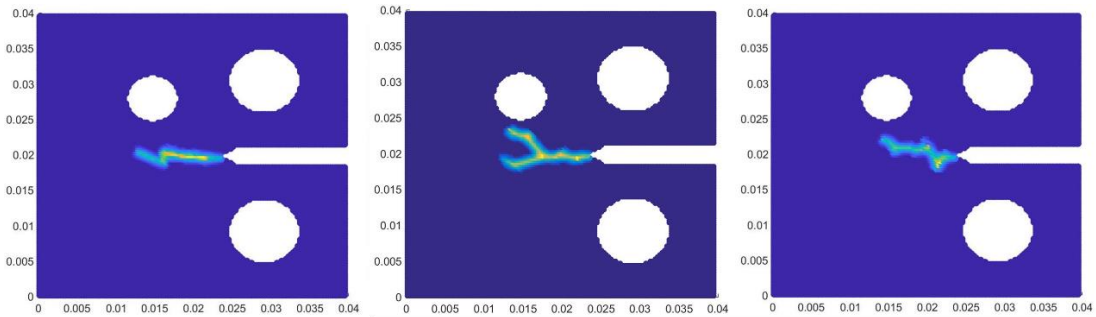

Figure 63. Crack pattern of polycrystal when $\beta = 0.1$. *(a) 25 grains,* $n = 246k$ cycles , *(b) 100 grains,* $n = 48k$ cycles , *and (c) 400 grains,* $n = 51k$ cycles

Figure 63 compares the crack patterns and total number of cycles for 25, 100 and 400 cycles, respectively, when $\beta = 0.1$. It can be found that the 25 grains model required much more cycles for the crack to propagate till the certain location (where $x \cong 12.5$ mm). As shown in Figure 59(a), the pre-existing crack tip is located right within a grain, and since the size of the crystal is much larger, the crack needs to propagate much longer to reach the boundary. Hence, the crack tip in Figure 63(a) required significantly more cycles ($246k$ cycles) to reach the target location than Figure 63(b) ($48k$ cycles). By increasing the total number of crystals, the number of bonds which cross the grain boundaries become larger. When $\beta < 1.0$, which means when the grain boundaries are weaker, the model with more crystals have more weaker bonds than the model with less crystals, i.e. the crack is much easier to propagate. Hence, it is expected that the number of cycles required for the crack tip

to reach the target location in the model with more crystals will be less than the model with less crystals. However, according to Figure 63(b) and Figure 63(c), the 400-crystal model required more cycles than the 100-crystal model, which is the opposite to what it was expected. This is because with the increasing of the total number of crystals within the model, there will be more points that are located at the boundary of multiple grains (as shown in red arrows in Figure 59(a)). When the crack tip reaches these key points, it required a certain number of cycles to "decide" which direction to propagate. The more number of key points are in the model, the more cycles are required for the crack tip to "decide" the propagation direction. Therefore, the number of cycles required for the crack in 400 crystal model to reach the target location is larger than that in 100 crystal model. When the interface strength coefficient β is changed from 0.1 to 0.5, the results remain similar.

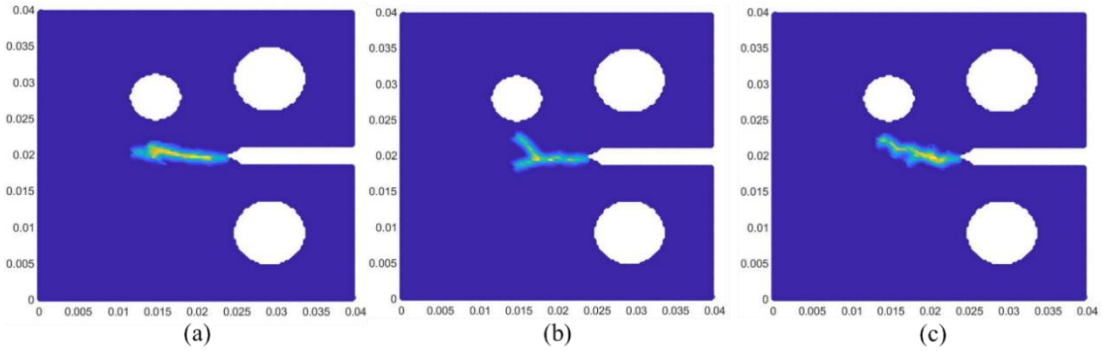

Figure 64. Crack pattern of polycrystal when $\beta = 0.5$. *(a) 25 grains,* $n = 331k$ cycles, *(b) 100 grains,* $n = 174k$ cycles, *and (c) 400 grains,* $n = 214k$ cycles

When $\beta > 1.0$, since the bond that crosses the grain boundary becomes stronger than those are located within the grains, the crack will more likely to propagate through grains (trans-granular fracture). Hence, more total number of crystals are in the model, the more bonds cross grain boundaries and the more cycles are required to reach the target location (as shown in Figure 65 and Figure 66).

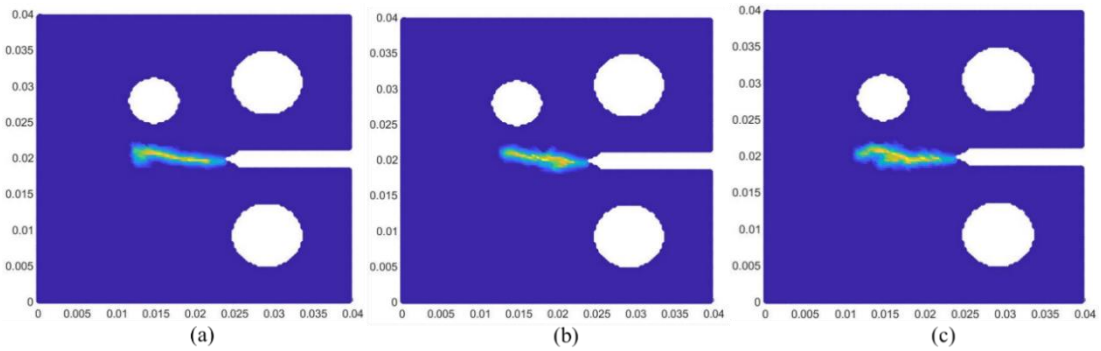

Figure 65. Crack pattern of polycrystal when $\beta = 2.0$ *. (a) 25 grains,* $n = 431k$ cycles *, (b) 100 grains,* $n = 453k$ cycles *, and (c) 400 grains,* $n = 512k$ cycles

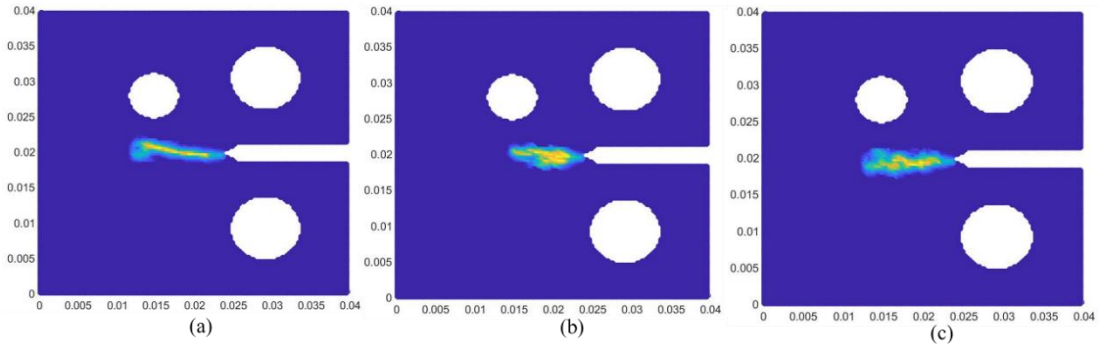

Figure 66. Crack pattern of polycrystal when $\beta = 10.0$ *. (a) 25 grains,* $n = 429k$ cycles *, (b) 100 grains,* $n = 784k$ cycles *, and (c) 400 grains,* $n = 846k$ cycles

5.4.6. Crack branching in fatigue analysis

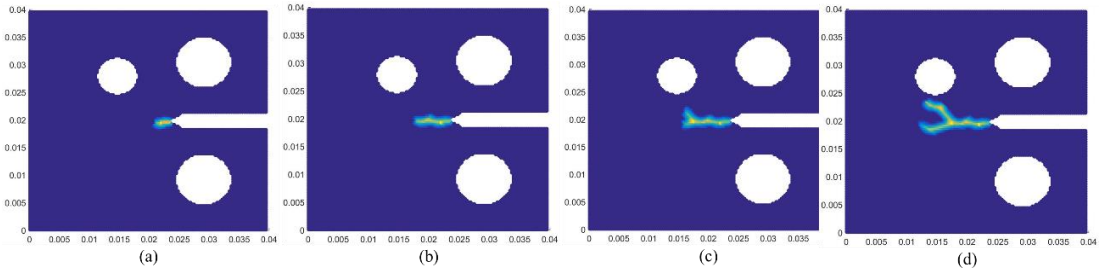

Figure 67. Crack pattern of polycrystal when $\beta = 0.1$ *, 100 grains, (a)* $n = 7.6k$ cycles *, (b)* $n = 22.5k$ cycles *, (c)* $n = 31.2k$ cycles *, and (d)* $n = 47.8k$ cycles

As shown in Figure 67, since $\beta = 0.1$, which means the fracture in the polycrystal model is mainly inter-granular fracture, the crack propagates following the grain boundary. However, when the crack tip reaches a certain key point (as shown by red arrow in Figure 59(b)), the crack branches, which also captured the similar concept

shown in the experiments described in (Vasudevan *et al.*, 1984, Gilbert, Schroeder and Ritchie, 1999, Rios, Tang and Miller, 1984).

5.5. Summary

In this chapter, a new crack tip detecting algorithm is introduced. By comparing the results from the new algorithm with that given in (Madenci and Oterkus, 2014), it can be concluded that the algorithm can correctly detect the crack tip location. And then fatigue analysis of polycrystal material is carried out. The approach described in (Stewart A. Silling and Askari, 2014) along with the new crack tip detecting algorithm are both used in fatigue analysis. The effect of interface strength coefficient on crack pattern, crystal size on crack propagation speed and the effect of crack branching are considered in the simulations. The observations based on the results can be summarised as:

1. The changing of the interface strength coefficient can capture different fracture modes (inter-granular fracture and trans-granular fracture). By comparing the experimental results and PD crack patterns, actual interface strength coefficients of a material can be estimated in the future.
2. The size of crystals can affect the crack propagation speed more on inter-granular fractures, rather than trans-granular fractures.
3. The crack branching in fatigue analysis can be captured by PD fatigue model automatically.

Due to the lack of experimental results on fatigue analysis of polycrystalline materials, the validation of the numerical results was not be able to carry out. However, the PD fatigue model has already be validated in (Guanfeng Zhang *et al.*,

2016). As for the future study, experiments can be used to validate the PD fatigue model. Moreover, a crack detecting algorithm can be extended for 3D model, along with the PD fatigue model, since the studies in this paper are mainly focused on 2D simulations.

6. DISCUSSIONS AND CONCLUSIONS

6.1. Discussions

6.1.1. Novelty and contribution to the field

Polycrystalline materials are widely used in many different industrial applications. Among which various polycrystalline materials, metals and ceramics are common examples. Since the fracture behaviour of polycrystalline materials can be affected by large number of variables, it is quite challenging to design safe structures without overdesign. Although experiments can provide valuable information regarding the polycrystalline material, the experimental approaches are not always viable. Hence, it is necessary to find a proper approach to study polycrystalline materials. The computational approaches discovered nowadays have several limitations to capture the transition from microscopic defects to macroscopic fractures. As discussed in the previous section, (De Meo, Zhu and Oterkus, 2016) provided a formulation to overcome these limitations. However, there was still limitation for BB PD formulation. The study described in Chapter 3 demonstrates that the limitation can be overcome by using OSB PD formulation.

SIF was introduced by (Irwin, 1957) to describe the stress distribution around the crack tip region and was widely used to predict fatigue crack growth (Schijve, 2009). Several theoretical formulations had been developed and coupled with different numerical methods to help researchers to study crack growth. Among which, J-integral is widely used in PD theory to compute the SIF around the crack tip region. In Chapter 4, DEM has been used to compute the SIF after obtaining the displacement field around the crack tip region using PD theory. The usage of DEM provides an alternative approach to compute SIF in PD framework.

Fatigue is one of the main reasons which causes failures in engineering structures, and predictions of these failures due to cyclic loadings are usually challenging. Several different approaches have been developed to overcome the challenges, including experimental methods (S-N curve, Paris' law etc.) and numerical methods (FEM, CZM and X-FEM etc.). The PD fatigue model has been introduced by (Stewart A. Silling and Askari, 2014), and developed by (Guanfeng Zhang *et al.*, 2016). (Y. L. Hu and Madenci, 2017) provided an alternative way to do the fatigue analysis in PD theory. This thesis extended the PD fatigue formulation given by (Stewart A. Silling and Askari, 2014) and coupled an crack tip tracking algorithm to study the fracture behaviour of 2D polycrystalline materials.

6.1.2. Gaps and recommended future work

In Chapter 3, a PD model was introduced to simulate cubic polycrystalline materials. In order to overcome the limitation which has been pointed in (De Meo, Zhu and Oterkus, 2016), OSB PD has been chosen in this thesis for simulation of cubic polycrystals. However, the prediction of the crack pattern was based on the assumption of the strength of grain boundary, Experimental studies can be used in the future to validate and refine the damage predictions of the proposed PD model. Moreover, the polycrystal study in Chapter 3 was mainly focused on 2D model. 2D formulation can be extended to 3D formulation to simulate more realistic problems. Parallel programming and multiscale modelling can be used to significantly reduce the computation time of simulations.

Concerning the calculation of SIF using DEM under PD framework, it was found that the accuracy of the calculation of SIF using DEM depends on the choice of reference nodes. Closer the nodes to the crack surface, smaller the discretization

sizes and more accurate solution. Since standard squared discretization was used in this thesis for PD simulation, the study of triangular discretization can be considered in the future to study if the accuracy can be improved. Moreover, Mode III crack problems along with 3D problems can also be studied in the future.

Concerning the PD fatigue model, BB PD theory has been extended for the simulation of polycrystalline materials. However, the Poisson's ratio is limited to 1/3 for 2D BB PD formulation and 1/4 for 3D BB PD problems. For future studies, OSB PD can be considered, and formulations can be extended for fatigue model.

6.2. Conclusions

As described in Chapter 1.2, the main objective of this thesis is to use PD theory to build up models for analysis of polycrystalline materials. The fracture behaviour under dynamic loading conditions and cyclic loading conditions are both considered. The main achievements in line with the research objectives of this thesis are shown below:

- OSB PD formulation was developed to support for studying the fracture behaviour of polycrystalline materials. The formulation overcomes the limitations on material constants as in the BB PD theory. The model captures quite accurately for the static deformation behaviour of cubic polycrystalline materials between PD and FEM. The dynamic analyses are then carried out, and successfully investigate the effect of interface strength coefficient, discretization size and crystal size to the fracture behaviour.
- A coupled DEM and PD theory was developed to calculate stress intensity factors. After analysing three benchmark problems and comparing the results between DEM+PD, ANSYS and analytical solutions, it could be concluded

that the model can provide an alternative approach to accurately compute SIFs.

- A crack tip tracking algorithm was developed to support the fatigue analysis. Since it was critical to track the location of the crack tip and update the location every cycle, it was necessary to create an algorithm so that the location can be updated automatically. The algorithm can meet the requirements and provide accurate results after comparing with benchmark problem given in (Madenci and Oterkus, 2014).
- A BB PD model of fatigue analysis of polycrystalline materials was created by extending an existing approach. The effect of interface strength coefficient on crack patterns, crystal size on crack propagation speed and crack branching have been studied.

6.3. Research outputs

- Zhu, N., & Oterkus, E. (2020). Calculation of stress intensity factor using displacement extrapolation method in peridynamic framework. *Journal of Mechanics*, *36*(2), 235-243. doi: https://doi.org/10.1017/jmech.2019.62
- Zhu, N., De Meo, D., & Oterkus, E. (2016). Modelling of granular fracture in polycrystalline materials using ordinary state-based peridynamics. *Materials*, *9*(12), [977]. https://doi.org/10.3390/ma9120977
- De Meo, D., Zhu, N., & Oterkus, E. (2016). Peridynamic modeling of granular fracture in polycrystalline materials. *Journal of Engineering Materials and Technology*, *138*(4), [041008]. https://doi.org/10.1115/1.4033634

- De Meo, D., Diyaroglu, C., Zhu, N., Oterkus, E., & Siddiq, M. A. (2016). Modelling of stress-corrosion cracking by using peridynamics. *International Journal of Hydrogen Energy*, *41*(15), 6593-6609. https://doi.org/10.1016/j.ijhydene.2016.02.154
- De Meo, D., Diyaroglu, C., Zhu, N., Oterkus, E., & Siddiq, M. A. (2015). Multiphysics modelling of stress corrosion cracking by using peridynamics. In *Analysis and Design of Marine Structures - Proceedings of the 5th International Conference on Marine Structures, MARSTRUCT 2015* (pp. 499-504)
- Oterkus, E., Diyaroglu, C., Zhu, N., Oterkus, S., & Madenci, E. (2015). Utilization of peridynamic theory for modeling at the nano-scale. In X. Baillin, C. Joachim, & G. Poupon (Eds.), *Nanopackaging: From Nanomaterials to the Atomic Scale: Proceedings of the 1st International Workshop on Nanopackaging, Grenoble 27-28 June 2013* (pp. 1-16). (Advances in atom and single molecule machines). Springer. https://doi.org/10.1007/978-3-319-21194-7

REFERENCE

Aliabadi, M.H. and Rooke, D.P. (1991) *Numerical fracture mechanics.* Springer Science & Business Media.

Anderson, T.L. (2005) *Fracture mechanics: fundamentals and applications.* CRC press.

Askari, E. *et al.* (2008) Published. 'Peridynamics for multiscale materials modeling'. *Journal of Physics: Conference Series*, 2008. IOP Publishing, pp.012078.

ATSB (2013) 'In-flight uncontained engine failure Airbus A380-842, VH-OQA'.

Azvision (2015) *Criminal case launched on Azerbaijani offshore oil platform collapse.* Available at: https://en.azvision.az/news.php?id=24881 (Accessed: 05/08).

Bagirova, N. (2015) *One worker killed, 30 missing after Azeri oil rig fire: government.* Available at: https://www.reuters.com/article/us-azerbaijan-accident-fire-idUSKBN0TO09H20151205 (Accessed: 05/08).

Barenblatt, G.I. (1962) 'The mathematical theory of equilibrium cracks in brittle fracture'. *Advances in applied mechanics.* Elsevier, pp. 55-129.

Barsoum, R.S. (1976) 'On the use of isoparametric finite elements in linear fracture mechanics'. *International journal for numerical methods in engineering*, 10 (1), pp. 25-37.

Barut, A., Guven, I. and Madenci, E. (2006) 'A meshless grain element for micromechanical analysis with crystal plasticity'. *International journal for numerical methods in engineering*, 67 (1), pp. 17-65.

Belytschko, T. and Black, T. (1999) 'Elastic crack growth in finite elements with minimal remeshing'. *International journal for numerical methods in engineering,* 45 (5), pp. 601-620.

Ben-Daya, M., Kumar, U. and Murthy, D.N.P. (2016) *Introduction to Maintenance Engineering: Modelling, Optimization and Management.* Wiley.

Benedetti, I. and Aliabadi, M. (2013) 'A three-dimensional cohesive-frictional grain-boundary micromechanical model for intergranular degradation and failure in polycrystalline materials'. *Computer Methods in Applied Mechanics and Engineering,* 265 36-62.

Blandford, G.E., Ingraffea, A.R. and Liggett, J.A. (1981) 'Two-dimensional stress intensity factor computations using the boundary element method'. *International Journal for Numerical Methods in Engineering,* 17 (3), pp. 387-404.

Bouvard, J.-L. *et al.* (2009) 'A cohesive zone model for fatigue and creep–fatigue crack growth in single crystal superalloys'. *International Journal of Fatigue,* 31 (5), pp. 868-879.

Bronkhorst, C., Kalidindi, S. and Anand, L. (1992) 'Polycrystalline plasticity and the evolution of crystallographic texture in FCC metals'. *Phil. Trans. R. Soc. Lond. A,* 341 (1662), pp. 443-477.

Cervera, M. and Chiumenti, M. (2006) 'Mesh objective tensile cracking via a local continuum damage model and a crack tracking technique'. *Computer methods in applied mechanics engineering,* 196 (1-3), pp. 304-320.

Cervera, M. *et al.* (2010) 'A crack-tracking technique for localized damage in quasi-brittle materials'. *Engineering Fracture Mechanics,* 77 (13), pp. 2431-2450.

Chen, C. and Li, S. (1998) 'Distribution of stresses and elastic strain energy in an ideal multicrystal model'. *Materials Science and Engineering: A,* 257 (2), pp. 312-321.

Chen, Y.M. (1975) 'Numerical computation of dynamic stress intensity factors by a Lagrangian finite-difference method (the HEMP code)'. *Engineering Fracture Mechanics,* 7 (4), pp. 653-660.

Chevalier, J., Olagnon, C. and Fantozzi, G. (1999) 'Subcritical crack propagation in 3Y-TZP ceramics: static and cyclic fatigue'. *Journal of the American Ceramic Society,* 82 (11), pp. 3129-3138.

Courant, R. (1994) 'Variational methods for the solution of problems of equilibrium and vibrations'. *Bulletin of the American Mathematical Society,* 49 1-23.

Cox, J.V. (2009) 'An extended finite element method with analytical enrichment for cohesive crack modeling'. *nternational Journal for Numerical Methods in Engineering,* 78 (1), pp. 48-83.

Crocker, A., Flewitt, P. and Smith, G. (2005) 'Computational modelling of fracture in polycrystalline materials'. *International materials reviews,* 50 (2), pp. 99-125.

Cruse, T. (1969) 'Numerical solutions in three dimensional elastostatics'. *International journal of solids structures,* 5 (12), pp. 1259-1274.

Dauskarat, R.H., Marshall, D.B. and Ritchie, R.O. (1990) 'Cyclic fatigue-crack propagation in magnesia-partially-stabilized zirconia ceramics'. *Journal of the American Ceramic Society,* 73 (4), pp. 893-903.

Dauskardt, R.H., Yu, W. and Ritchie, R.O. (1987) 'Fatigue crack propagation in transformation-toughened zirconia ceramic'. *Journal of the American Ceramic Society,* 70 (10), pp. C-248-C-252.

De Meo, D., Zhu, N. and Oterkus, E. (2016) 'Peridynamic modeling of granular fracture in polycrystalline materials'. *Journal of Engineering Materials and Technology,* 138 (4), pp.

Dhondt, G. (1998) 'Automatic 3-D mode I crack propagation calculations with finite elements'. *International Journal for Numerical Methods in Engineering,* 41 (4), pp. 739-757.

Diyaroglu, C. *et al.* (2015) 'Peridynamics for bending of beams and plates with transverse shear deformation'. *International Journal of Solids and Structures,* 69 152-168.

Dominguez, J. and Gallego, R. (1992) 'Time domain boundary element method for dynamic stress intensity factor computations'. *International journal for numerical methods in engineering,* 33 (3), pp. 635-647.

Donahue, R.J. *et al.* (1972) 'Crack opening displacement and the rate of fatigue crack growth'. *International Journal of Fracture Mechanics,* 8 (2), pp. 209-219.

Dong, P. (2001) 'A structural stress definition and numerical implementation for fatigue analysis of welded joints'. *International Journal of Fatigue,* 23 (10), pp. 865-876.

Dowling, N. and Begley, J. (1976) 'Fatigue crack growth during gross plasticity and the J-integral'. *Mechanics of crack growth.* ASTM International, pp.

Dugdale, D.S. (1960) 'Yielding of steel sheets containing slits'. *Journal of the Mechanics and Physics of Solids,* 8 (2), pp. 100-104.

Executive, M. (2016) *Third Fatal Accident on SOCAR's Offshore Platforms.* Available at: https://www.maritime-executive.com/article/third-fatal-accident-on-socars-offshore-platforms (Accessed: 05/08).

Gay, P., Hirsch, P. and Kelly, A. (1954) 'X-ray studies of polycrystalline metals deformed by rolling. III. The physical interpretation of the experimental results'. *Acta Crystallographica,* 7 (1), pp. 41-49.

Gerstle, W.H., Martha, L.F. and Ingraffea, A.R. (1987) 'Finite and boundary element modeling of crack propagation in two and three dimensions'. *Engineering with Computers,* 2 (3), pp. 167-183.

Gilbert, C.J., Schroeder, V. and Ritchie, R.O. (1999) 'Mechanisms for fracture and fatigue-crack propagation in a bulk metallic glass'. *Metallurgical and Materials Transactions A,* 30 (7), pp. 1739-1753.

Groeber, M.A. *et al.* (2006) '3D reconstruction and characterization of polycrystalline microstructures using a FIB–SEM system'. *Materials Characterization,* 57 (4-5), pp. 259-273.

Gross, B. and Mendelson, A. (1972) 'Plane elastostatic analysis of V-notched plates'. *International Journal of Fracture Mechanics,* 8 (3), pp. 267-276.

Guinea, G.V. *et al.* (1998) 'Stress intensity factor, compliance and CMOD for a general three-point-bend beam'. *International Journal of Fracture,* 89 (2), pp. 103-116.

Herbig, M. *et al.* (2011) '3-D growth of a short fatigue crack within a polycrystalline microstructure studied using combined diffraction and phase-contrast X-ray tomography'. *Acta Materialia,* 59 (2), pp. 590-601.

Hillerborg, A., Modéer, M. and Petersson, P.E. (1976) 'Analysis of crack formation and crack growth in concrete by means of fracture mechanics and finite elements'. *Cement and concrete research,* 6 (6), pp. 773-781.

Hinton, E. and Irons, B. (1968) 'Least squares smoothing of experimental data using finite elements'. *Strain,* 4 (3), pp. 24-27.

Hopper, C.D. and Miller, K.J. (1977) 'Fatigue crack propagation in biaxial stress fields'. *The Journal of Strain Analysis for Engineering Design,* 12 (1), pp. 23-28.

Hosford, W.F. (1993) *The Mechanics of Crystals and Textured Polycrystals.* NY, USA: Oxford University Press: New York.

Hrennikoff, A. (1941) 'Solution of problems of elasticity by the framework method'. *Journal of applied mechanics,* 8 (4), pp. 169-175.

Hu, W. *et al.* (2012) 'The formulation and computation of the nonlocal J-integral in bond-based peridynamics'. *International journal of fracture,* 176 (2), pp. 195-206.

Hu, Y.L. and Madenci, E. (2017) 'Peridynamics for fatigue life and residual strength prediction of composite laminates'. *Composite Structures,* 160 169-184.

Huffman, P.J. *et al.* (2017) 'Fatigue crack propagation prediction of a pressure vessel mild steel based on a strain energy density model'. *Frattura ed Integrita Strutturale,* 42 74-84.

Imachi, M., Tanaka, S. and Bui, T.Q. (2018) 'Mixed-mode dynamic stress intensity factors evaluation using ordinary state-based peridynamics'. *Theoretical and Applied Fracture Mechanics,* 93 97-104.

Ingraffea, A. (1978) Published. 'On discrete fracture propagation in rock loaded in compression'. *Proceedings, First International Conference on Numerical Methods in Fracture Mechanics,* 1978. pp.235-248.

Irwin, G.R. (1957) 'Analysis of stresses and strains near the end of a crack traversing a plate'. *J. appl. Mech.,* 24 351-369.

Kaw, A.K. (2005) *Mechanics of composite materials*. CRC press.

Kilic, B. and Madenci, E. (2010) 'An adaptive dynamic relaxation method for quasi-static simulations using the peridynamic theory'. *Theoretical and Applied Fracture Mechanics,* 53 (3), pp. 194-204.

Kirane, K. and Ghosh, S. (2008) 'A cold dwell fatigue crack nucleation criterion for polycrystalline Ti-6242 using grain-level crystal plasticity FE model'. *International Journal of Fatigue,* 30 (12), pp. 2127-2139.

Kishimoto, K., Aoki, S. and Sakata, M. (1980) 'Simple formula for dynamic stress intensity factor of pre-cracked Charpy specimen'. *Engineering Fracture Mechanics,* 13 (3), pp. 501-508.

Kraft, R. *et al.* (2008) 'Computational micromechanics of dynamic compressive loading of a brittle polycrystalline material using a distribution of grain boundary properties'. *Journal of the Mechanics and Physics of Solids,* 56 (8), pp. 2618-2641.

Lazzarin, P. and Tovo, R. (1998) 'A notch intensity factor approach to the stress analysis of welds'. *Fatigue & fracture of engineering materials & structures,* 21 (9), pp. 1089-1103.

Lim, I.L., Johnston, I.W. and Choi, S.K. (1992) 'Comparison between various displacement-based stress intensity factor computation techniques'. *International Journal of Fracture,* 58 (3), pp. 193-210.

Lin, L., Wang, X. and Zeng, X. (2017) 'The role of cohesive zone properties on intergranular to transgranular fracture transition in polycrystalline solids'. *International Journal of Damage Mechanics,* 26 (3), pp. 379-394.

Lindley, T.C. and Richards, C.E. (1974) 'The relevance of crack closure to fatigue crack propagation'. *Materials Science Engineering,* 14 (3), pp. 281-293.

Liu, L. *et al.* (2011) 'In situ synchrotron X-ray imaging of high-cycle fatigue crack propagation in single-crystal nickel-base alloys'. *Acta Materialia,* 59 (13), pp. 5103-5115.

Liu, M. *et al.* (2015) 'An improved semi-analytical solution for stress at round-tip notches'. *Engineering fracture mechanics,* 149 134-143.

Ludwig, W. *et al.* (2009) 'New opportunities for 3D materials science of polycrystalline materials at the micrometre lengthscale by combined use of X-ray diffraction and X-ray imaging'. *Materials Science and Engineering: A,* 524 (1-2), pp. 69-76.

Macek, R.W. and Silling, S.A. (2007) 'Peridynamics via finite element analysis'. *Finite Elements in Analysis Design,* 43 (15), pp. 1169-1178.

Madenci, E. and Oterkus, E. (2014) *Peridynamic Theory and Its Applications.* New York: Springer.

Madenci, E. and Oterkus, S. (2016) 'Ordinary state-based peridynamics for plastic deformation according to von Mises yield criteria with isotropic hardening'. *Journal of the Mechanics and Physics of Solids,* 86 192-219.

Mariani, S. and Perego, U. (2003) 'Extended finite element method for quasi-brittle fracture'. *International Journal for numerical methods in engineering,* 58 (1), pp. 103-126.

Marines, I. *et al.* (2003) 'Ultrasonic fatigue tests on bearing steel AISI-SAE 52100 at frequency of 20 and 30 kHz'. *International Journal of Fatigue,* 25 (9-11), pp. 1037-1046.

Martínez, J. and Domínguez, J. (1984) 'On the use of quarter-point boundary elements for stress intensity factor computations'. *International Journal for Numerical Methods in Engineering,* 20 (10), pp. 1941-1950.

Miyazaki, N. *et al.* (1993) 'Stress intensity factor analysis of interface crack using boundary element method—application of contour-integral method'. *Engineering Fracture Mechanics,* 45 (5), pp. 599-610.

Moës, N., Dolbow, J. and Belytschko, T. (1999) 'A finite element method for crack growth without remeshing'. *International journal for numerical methods in engineering,* 46 (1), pp. 131-150.

Nagashima, T., Omoto, Y. and Tani, S. (2003) 'Stress intensity factor analysis of interface cracks using X-FEM'. *International Journal for Numerical Methods in Engineering,* 56 (8), pp. 1151-1173.

Newman, J.C. (1976) 'A finite-element analysis of fatigue crack closure'. *Mechanics of crack growth.* ASTM International, pp.

Newman, J.C. (1981) 'A crack-closure model for predicting fatigue crack growth under aircraft spectrum loading'. *Methods and models for predicting fatigue crack growth under random loading.* ASTM International, pp.

Nguyen, O. *et al.* (2001) 'A cohesive model of fatigue crack growth'. *International Journal of Fracture,* 110 (4), pp. 351-369.

Norway (1981) ' The "Alexander L. Kielland"-accident: from a Commission appointed by Royal Decree of 28th March, 1980 : report presented to Ministry of Justice and Police, March 1981'.

NTSB (1984) 'Highway Accident Report - Collapse of a Suspended Span of Interstate Route 95 Highway Bridge over the Mianus River Greenwich, Connecticut, June 28, 1983'.

NTSB (2016) *Investigative Update Provides Initial Findings in Investigation of Uncontained Engine Failure.* Available at: https://www.ntsb.gov/news/press-releases/Pages/PR20160912.aspx (Accessed: 12 August).

NTSB (2018) *Southwest Airlines engine accident.* Available at: https://www.ntsb.gov/investigations/Pages/DCA18MA142.aspx (Accessed: 17 August).

Oestern, H.J. *et al.* (2000) 'Facts About the Disaster at Eschede'. 14 (4), pp. 287-290.

Oterkus, E., Guven, I. and Madenci, E. (2010) Published. 'Fatigue failure model with peridynamic theory'. *2010 12th IEEE Intersociety Conference on Thermal and Thermomechanical Phenomena in Electronic Systems*, 2010. IEEE, pp.1-6.

Oterkus, E., Guven, I. and Madenci, E. (2012) 'Impact damage assessment by using peridynamic theory'. *Open Engineering*, 2 (4), pp. 523-531.

Oterkus, S. and Madenci, E. (2015) 'Peridynamics for antiplane shear and torsional deformations'. *Journal of Mechanics of Materials and Structures*, 10 (2), pp. 167-193.

Oterkus, S., Madenci, E. and Oterkus, E. (2017) 'Fully coupled poroelastic peridynamic formulation for fluid-filled fractures'. *Engineering geology*, 225 19-28.

Panchadhara, R. and Gordon, P.A. (2016) 'Application of peridynamic stress intensity factors to dynamic fracture initiation and propagation'. *International Journal of Fracture*, 201 (1), pp. 81-96.

Papoulia, K.D., Vavasis, S.A. and Ganguly, P. (2006) 'Spatial convergence of crack nucleation using a cohesive finite-element model on a pinwheel-based mesh'. *International Journal for Numerical Methods in Engineering*, 67 (1), pp. 1-16.

Paris, P.C. (1957) 'The Mechanics of Fracture Propagation and Solutions to Fracture Arrester Problem'.

Paris, P.C. (1961) 'A rational analytic theory of fatigue'. *The trend in engineering,* 13 9.

Paris, P.C. and Sih, G.C. (1965) 'Stress analysis of cracks'. *Fracture toughness testing and its applications.* ASTM International, pp. 30-81.

Parks, D.M. (1974) 'A stiffness derivative finite element technique for determination of crack tip stress intensity factors'. *International Journal of fracture,* 10 (4), pp. 487-502.

Pearson, S. (1975) 'Initiation of fatigue cracks in commercial aluminium alloys and the subsequent propagation of very short cracks'. *Engineering Fracture Mechanics,* 7 (2), pp. 235-247.

Petroski, H.J. and Achenbach, J.D. (1978) 'Computation of the weight function from a stress intensity factor'. *Engineering Fracture Mechanics,* 10 (2), pp. 257-266.

Potirniche, G.P. *et al.* (2005) 'Fatigue damage in nickel and copper single crystals at nanoscale'. *International Journal of Fatigue,* 27 (10-12), pp. 1179-1185.

Proudhon, H. *et al.* (2016) '3D simulation of short fatigue crack propagation by finite element crystal plasticity and remeshing'. *International Journal of Fatigue,* 82 238-246.

Rabczuk, T., Bordas, S. and Zi, G. (2010) 'On three-dimensional modelling of crack growth using partition of unity methods'. *Computers and structures,* 88 (23-24), pp. 1391-1411.

Reddy, J.N. (2013) *An introduction to continuum mechanics.* Cambridge university press.

Reece, M.J., Guiu, F. and Sammur, M.F.R. (1989) 'Cyclic fatigue crack propagation in alumina under direct tension—compression loading'. *Journal of the American Ceramic Society,* 72 (2), pp. 348-352.

Ren, H. *et al.* (2016) 'Dual-horizon peridynamics'. *International Journal for Numerical Methods in Engineering,* 108 (12), pp. 1451-1476.

Ren, H., Zhuang, X. and Rabczuk, T. (2016) 'A new peridynamic formulation with shear deformation for elastic solid'. *Journal of Micromechanics and Molecular Physics,* 1 (02), pp. 1650009.

Rice, J. (1967) 'Mechanics of crack tip deformation and extension by fatigue'. *Fatigue crack propagation.* ASTM International, pp.

Rios, E.R.D.L., Tang, Z. and Miller, K.J. (1984) 'Short crack fatigue behaviour in a medium carbon steel'. *Fatigue & Fracture of Engineering Materials & Structures,* 7 (2), pp. 97-108.

Rizzo, F.J. (1967) 'An integral equation approach to boundary value problems of classical elastostatics'. *Quarterly of applied mathematics,* 25 (1), pp. 83-95.

Roe, K.L. and Siegmund, T. (2003) 'An irreversible cohesive zone model for interface fatigue crack growth simulation'. *Engineering fracture mechanics,* 70 (2), pp. 209-232.

Rooke, D.P. and Cartwright, D.J. (1976) 'Compendium of stress intensity factors'. *Procurement Executive, Ministry of Defence. H. M. S. O.,* 330.

Rybicki, E.F. and Kanninen, M.F. (1977) 'A finite element calculation of stress intensity factors by a modified crack closure integral'. *Engineering fracture mechanics,* 9 (4), pp. 931-938.

Sadd, M.H. (2009) *Elasticity: theory, applications, and numerics.* Academic Press.

Saloustros, S., Pelà, L. and Cervera, M. (2015) 'A crack-tracking technique for localized cohesive–frictional damage'. *Engineering Fracture Mechanics*, 150 96-114.

Sancho, J.M. *et al.* (2007) 'An embedded crack model for finite element analysis of concrete fracture'. *Engineering Fracture Mechanics,* 74 (1-2), pp. 75-86.

Schijve, J. (2009) 'Stress Intensity Factors of Cracks'. *Fatigue of Structures and Materials.* Dordrecht: Springer Netherlands, pp. 105-140.

Sfantos, G. and Aliabadi, M. (2007a) 'A boundary cohesive grain element formulation for modelling intergranular microfracture in polycrystalline brittle materials'. *International journal for numerical methods in engineering,* 69 (8), pp. 1590-1626.

Sfantos, G. and Aliabadi, M. (2007b) 'Multi-scale boundary element modelling of material degradation and fracture'. *Computer Methods in Applied Mechanics and Engineering,* 196 (7), pp. 1310-1329.

Shih, C.F., de Lorenzi, H.G. and German, M.D. (1976) 'Crack extension modeling with singular quadratic isoparametric elements'. *International Journal of Fracture,* 12 (4), pp. 647-651.

Shiozawa, K., Lu, L. and Ishihara, S. (2001) 'S–N curve characteristics and subsurface crack initiation behaviour in ultra-long life fatigue of a high carbon-chromium bearing steel'. *Fatigue Fracture of Engineering Materials Structures,* 24 (12), pp. 781-790.

Sih, G.C. and Barthelemy, B.M. (1980) 'Mixed mode fatigue crack growth predictions'. *Engineering Fracture Mechanics,* 13 (3), pp. 439-451.

Sih, G.C., Paris, P.C. and Erdogan, F. (1962) 'Crack-tip, stress-intensity factors for plane extension and plate bending problems'. *Journal of Applied Mechanics,* 29 (2), pp. 306-312.

Silling, S.A. (2000) 'Reformulation of elasticity theory for discontinuities and long-range forces'. *Journal of the Mechanics and Physics of Solids,* 48 (1), pp. 175-209.

Silling, S.A. and Askari, A. (2014) 'Peridynamic Model for Fatigue Cracking'.

Silling, S.A. and Askari, E. (2005) 'A meshfree method based on the peridynamic model of solid mechanics'. *Computers & structures,* 83 (17-18), pp. 1526-1535.

Silling, S.A. and Bobaru, F. (2005) 'Peridynamic modeling of membranes and fibers'. *International Journal of Non-Linear Mechanics,* 40 (2-3), pp. 395-409.

Silling, S.A. *et al.* (2007) 'Peridynamic states and constitutive modeling'. *Journal of Elasticity,* 88 (2), pp. 151-184.

Smith, R.A. (2013) 'Hatfield Memorial Lecture 2007 Railways and materials: synergetic progress'. *Ironmaking & Steelmaking,* 35 (7), pp. 505-513.

Stenström, C. and Eriksson, K. (2019) 'The J-contour integral in peridynamics via displacements'. *International Journal of Fracture,* 216 (2), pp. 173-183.

Sturm, D. *et al.* (2007) 'The influence of silicon on the strength and fracture toughness of molybdenum'. *Materials Science and Engineering: A,* 463 (1-2), pp. 107-114.

Sukumar, N., Chopp, D.L. and Moran, B. (2003) 'Extended finite element method and fast marching method for three-dimensional fatigue crack propagation'. *Engineering Fracture Mechanics,* 70 (1), pp. 29-48.

Sukumar, N. and Srolovitz, D. (2004) 'Finite element-based model for crack propagation in polycrystalline materials'. *Computational and Applied Mathematics,* 23 (2-3), pp. 363-380.

Sukumar, N. *et al.* (2003) 'Brittle fracture in polycrystalline microstructures with the extended finite element method'. *International Journal for Numerical Methods in Engineering,* 56 (14), pp. 2015-2037.

Tang, T., Kim, S. and Horstemeyer, M.F. (2010) 'Fatigue crack growth in magnesium single crystals under cyclic loading: molecular dynamics simulation'. *Computational Materials Science,* 48 (2), pp. 426-439.

Thompson, P. (2001) 'How Much Did the Liberty Shipbuilders Learn? New Evidence for an Old Case Study'. 109 (1), pp. 103-137.

Tracey, D.M. (1971) 'Finite elements for determination of crack tip elastic stress intensity factors'. *Engineering Fracture Mechanics,* 3 (3), pp. 255-265.

Underwood, P. (1983) *Dynamic relaxation. Computational Methods for Transient Dynamic Analysis.*

Vasudevan, A.K. *et al.* (1984) 'Fatigue crack growth behavior of aluminum alloy 2020 (Al-Cu-Li-Mn-Cd)'. *Materials Science and Engineering,* 64 (1), pp. 113-122.

Von Euw, E.F.J., Hertzberg, R.W. and Roberts, R. (1972) Published. 'Delay effects in fatigue crack propagation'. *Stress Analysis and Growth of Cracks: Proceedings of the 1971 National Symposium on Fracture Mechanics: Part 1,* 1972. ASTM International.

Wang, C. and Xu, X. (2015) 'Cohesive element analysis of fatigue delamination propagation in composite materials with improved crack tip tracking algorism'. *Composite Structures,* 134 176-184.

Warner, D. and Molinari, J. (2006) 'Micromechanical finite element modeling of compressive fracture in confined alumina ceramic'. *Acta Materialia,* 54 (19), pp. 5135-5145.

Warren, T.L. *et al.* (2009) 'A non-ordinary state-based peridynamic method to model solid material deformation and fracture'. *International Journal of Solids Structures,* 46 (5), pp. 1186-1195.

Wolf, E. (1970) 'Fatigue crack closure under cyclic tension'. *Engineering Fracture Mechanics,* 2 (1), pp. 37-45.

Xiao, Z.M. and Chen, B.J. (2001) 'Stress intensity factor for a Griffith crack interacting with a coated inclusion'. *International Journal of Fracture,* 108 (3), pp. 193-205.

Xu, X.-P. and Needleman, A. (1994) 'Numerical simulations of fast crack growth in brittle solids'. *Journal of the Mechanics and Physics of Solids,* 42 (9), pp. 1397-1434.

Yang, B., Mall, S. and Ravi-Chandar, K. (2001) 'A cohesive zone model for fatigue crack growth in quasibrittle materials'. *International Journal of solids Structures,* 38 (22-23), pp. 3927-3944.

Zhai, T.-g., Wilkinson, A.J. and Martin, J.W. (2000) 'A crystallographic mechanism for fatigue crack propagation through grain boundaries'. *Acta materialia,* 48 (20), pp. 4917-4927.

Zhang, G. *et al.* (2016) 'Validation of a peridynamic model for fatigue cracking'. *Engineering Fracture Mechanics,* 162 76-94.

Zhang, W. (2016) 'Technical Problem Identification for the Failures of the Liberty Ships'. *Challenges,* 7 (2), pp.

Zheng, X. and Hirt, M.A. (1983) 'Fatigue crack propagation in steels'. *Engineering Fracture Mechanics,* 18 (5), pp. 965-973.

Zhou, T. *et al.* (2012) 'Crack propagation simulation in microstructure of ceramic tool materials'. *Computational Materials Science,* 54 150-156.

Zhu, N., De Meo, D. and Oterkus, E. (2016) 'Modelling of granular fracture in polycrystalline materials using ordinary state-based peridynamics'. *Materials,* 9 (12), pp. 977.

Zhu, Z. *et al.* (2006) 'Stress intensity factor for a cracked specimen under compression'. *Engineering Fracture Mechanics,* 73 (4), pp. 482-489.

Zi, G., Rabczuk, T. and Wall, W. (2007) 'Extended meshfree methods without branch enrichment for cohesive cracks'. *Computational Mechanics,* 40 (2), pp. 367-382.